

Measurement of
 $\sigma(\text{p}\bar{\text{p}} \rightarrow \text{Z}) \times \text{BR}(\text{Z} \rightarrow \text{b}\bar{\text{b}})$ at
 $\sqrt{s} = 1.96 \text{ TeV}$

N. Axel Naumann
Radboud Universiteit Nijmegen

Measurement of $\sigma(\text{p}\bar{\text{p}} \rightarrow \text{Z}) \times \text{BR}(\text{Z} \rightarrow \text{b}\bar{\text{b}})$ at $\sqrt{s} = 1.96 \text{ TeV}$

Proefschrift

ter verkrijging van de graad van doctor
aan de Radboud Universiteit Nijmegen
op gezag van de rector magnificus prof. dr. J.H.J.M. van Krieken,
volgens besluit van het college van decanen
in het openbaar te verdedigen op

maandag 24 oktober 2016
om 14.30 uur precies

door
Nikolaus Axel Naumann
geboren op 9 mei 1974
te Kassel, Duitsland

Promotor: Prof. dr. S.J. de Jong

Copromotor: Dr. F. Filthaut

Manuscriptcommissie: Prof. dr. N. de Groot

Prof. dr. P.J. de Jong (Universiteit van Amsterdam)

Prof. dr. D.O. Whiteson (University of California, VS)

Contents

1	Introduction	1
2	Theory	5
2.1	The Standard Model	5
2.1.1	The Higgs Mechanism	7
2.2	The $Z \rightarrow b\bar{b}$ Process	7
2.2.1	Event Topology, Notation	8
2.2.2	Z Production	8
2.2.3	The Z Decay	9
2.2.4	The Z Resonance in $b\bar{b}$ Production	10
2.2.5	Electroweak Contributions through Virtual Photons to the $b\bar{b}$ Production	10
2.2.6	Cross Section of $p\bar{p} \rightarrow b\bar{b}$	11
2.2.7	Prediction of the $p\bar{p} \rightarrow Z$ Production Cross Section	13
2.3	Higgs Production	13
2.4	Final State of the $Z \rightarrow b\bar{b}$ Process	15
2.4.1	Jet Production	15
2.4.2	b-Hadrons	17
2.4.3	Azimuthal Jet Separation	19
2.5	b-Jet Production through the Strong Interaction	21
2.5.1	Strong Production	21
2.5.2	Light Flavor Contribution	22
2.5.3	Heavy Flavor Contribution	22
2.5.4	Mixed Flavor Contribution	26
3	The DØ Detector	29
3.1	The Tevatron	29
3.1.1	Proton Production and Acceleration	29
3.1.2	Anti-Proton Production and Acceleration	30

3.1.3	Beam Characteristics	32
3.2	The DØ Detector	32
3.3	Tracking	33
3.3.1	Solenoid Magnet	33
3.3.2	Silicon Microstrip Tracker	34
3.3.3	Radiation Protection System	36
3.3.4	Central Fiber Tracker	39
3.4	Calorimetry	40
3.4.1	Preshower Detectors	40
3.4.2	Calorimeter	41
3.5	Muon System	44
3.5.1	Toroid Magnet	46
3.5.2	Proportional Drift Tubes	46
3.5.3	Scintillator Counters	49
3.6	Luminosity System	49
3.7	Data Acquisition and Trigger	50
3.7.1	First Level Trigger System	52
3.7.2	Second Level Trigger System	53
3.7.3	Third Level Trigger System	53
3.7.4	Online Event Selection	54
3.8	Monte Carlo Event Modeling	54
3.8.1	Pythia	55
3.8.2	Simulation of the Detector Response	55
3.9	Event Reconstruction	55
4	Data Selection	57
4.1	Efficiency Correction	57
4.2	Trigger	59
4.2.1	Level 1 Trigger	60
4.2.2	Level 2 Trigger	65
4.2.3	Level 3 Trigger	65
4.3	Offline Object Identification	66
4.3.1	Muons	67
4.3.2	Jets	74
4.3.3	b-Jets	77

4.4	Event Selection	85
4.4.1	b-Jet Selection	85
4.4.2	Measurement of b-Jet Purity Using p_T^{rel}	86
4.4.3	Suppression of Inclusive b Production	89
4.5	Invariant Mass Spectra	89
4.5.1	QCD Prediction	90
4.5.2	Impact of the Z Resonance	90
5	Z \rightarrow $b\bar{b}$ Cross Section Measurement	93
5.1	Outline	93
5.2	Efficiency and Statistical Uncertainties	94
5.2.1	Efficiency Correlations	95
5.2.2	Validity of b-Jet Efficiencies for Z \rightarrow $b\bar{b}$ Events	95
5.2.3	Sources of Inefficiencies	96
5.2.4	Correlations across Invariant Mass Bins, Bin Uncertainty	97
5.3	Signal Extraction	100
5.3.1	Z-Enriched Invariant Mass Spectrum	101
5.3.2	Z-Suppressed Invariant Mass Spectrum	101
5.3.3	Comparison of Z-Enriched and -Suppressed Samples	103
5.3.4	Phase Space Corrections Deduced from Light Jets	103
5.3.5	Signal Expectation	106
5.3.6	Signal Optimization	106
5.3.7	Luminosity Measurement	108
5.3.8	Systematic Uncertainty	108
5.3.9	Signal Fit	109
5.4	Exclusion Limit	111
6	Comparison to other Measurements and Theory	113
6.1	Other Measurements	113
6.2	Prediction from Theory	114
6.3	Conclusion	114
	Bibliography	117

Chapter 1

Introduction

High energy physics probes nature at the smallest scale, to detect the fundamental rules that also govern nature at the largest scale: the universe. Physicists have made tremendous progress over the last century; today, most probes into nature’s behavior give “boring” results: our models predict what will happen to an extremely high degree.¹ This holds both for the smallest scale, where the Standard Model provides us with excellent predictions, and the largest scale, where General Relativity has yet to find its limits — were it not for the intersection of both:

While each model is powerful by itself, theoreticians have struggled to combine them since decades. Several theories have been suggested; none of them has been providing a prediction that falls outside the Standard Model predictions and that has been confirmed by measurement. Even more interesting, there are properties of the universe and of the particle world that remain to be explained. An example is the fact that only 4.6% of the universe’s mass stems from “ordinary matter” that we understand [64].

The last remaining corner stone of the Standard Model that required verification is the Higgs boson. It was found with a mass that is marginally consistent in the Standard Model; a lower mass could have been an interesting hint for physics beyond the Standard Model. The next best guess is to look for deviations in the Higgs particle’s properties from the Standard Model’s prediction. In particular the branching fraction of the Higgs to two b-quarks is a sensitive indicator for physics beyond the Standard Model. The precise measurement of $b\bar{b}$ resonances is thus crucial. The $Z \rightarrow b\bar{b}$ decay is an irreducible background to this process and therefore has to be understood quantitatively

¹The biggest issue is often not a failure in the model, but the complexity of applying it to measurement predictions.

as a background. In addition, it also provides a measurement, or at least a check on the detection efficiency for $H \rightarrow b\bar{b}$.

The study presented here is about measuring the $Z \rightarrow b\bar{b}$ process at the Tevatron.

Overview

The Z boson is one of the four electroweak interaction's gauge bosons. Its properties and its decay processes are theoretically well understood, and experimentally precisely studied, especially at LEP [23, 10, 11, 6]. Studying them at a hadron collider is a valuable cross-check for the universality of the theoretical predictions.

At hadron colliders the production of Z bosons followed by their decay in charged lepton pairs is well studied [49, 44, 45]. The charged leptons are relatively easy to identify and their properties can be precisely measured. For hadronic decays, i.e. $Z \rightarrow q\bar{q}$ with $q = u, d, s, c, b$, this is much more difficult due to the large hadronic background in hadron colliders. In this case the signal to background can be improved by studying the decay $Z \rightarrow b\bar{b}$, because the heavy quark background is much smaller than the light flavor quark background. Because the branching ratio $Z \rightarrow b\bar{b}$ is known to high precision from LEP, one can test the prediction of the process $p\bar{p} \rightarrow Z \rightarrow b\bar{b}$, a weak interaction that depends critically on the “composition” of the proton and antiproton.

QCD predicts the flavor and momentum distribution for the quarks and gluons of the colliding protons. It allows to extend measurements for instance from HERA, an electron-proton collider, to proton-proton collisions at the Tevatron. Thus, the measurement of the cross section for $p\bar{p} \rightarrow Z \rightarrow b\bar{b}$ tests the combined predictions of the electroweak theory and QCD.

The process $p\bar{p} \rightarrow Z \rightarrow b\bar{b}$ also plays a key role in two other areas. The $H \rightarrow b\bar{b}$ decay is the dominant decay mode for the Higgs, making it suitable for Higgs analyses at the Tevatron and LHC, despite the fact that this decay has not been observed yet. Due to its similarity, the process $p\bar{p} \rightarrow Z \rightarrow b\bar{b}$ allows to test the sensitivity of analyses in that Higgs channel.

As a second side effect, the process $p\bar{p} \rightarrow Z \rightarrow b\bar{b}$ allows to determine the quality of the energy measurement for b-jets, by gauging the $b\bar{b}$ invariant mass to the well known Z mass. The precision of the b-jet energy is a relevant ingredient e.g. for the top mass measurement and to optimize the detection of the $H \rightarrow b\bar{b}$ decay.

The measurement of this process at CDF [51] was the first detection at a hadron collider. A recent example of an analysis using $b\bar{b}$ pairs produced in conjunction with leptons from weak boson decay can be found in [36]. This thesis will present an attempt to measure the process $p\bar{p} \rightarrow Z \rightarrow b\bar{b}$ at DØ, on a smaller data set. In chapter 2 the theory pertaining to the measurement will be treated, zooming in on the theoretical understanding of the signal and its backgrounds. Chapter 3 will introduce the accelerator, the Tevatron, and the DØ detector, which provided the data that was used for the analysis. Chapter 4 will deal with the data selection in trigger and off-line and the description of the Monte Carlo samples that are used in this analysis. Notably, efficiency calculations and corrections will be introduced in this chapter. Chapter 5 presents the method to extract the $p\bar{p} \rightarrow Z \rightarrow b\bar{b}$ cross section from the data. In chapter 6 the measurement is confronted with the theory and with measurements in the charged lepton decay channels.

Chapter 2

Theory

2.1 The Standard Model

The Standard Model is the currently accepted best theoretical framework for elementary particle physics [61]. It describes in detail the known properties of the presently known particles, including the electroweak and strong interaction. The Standard Model predicts the cross sections of interacting particles, for instance of $p\bar{p}$ -collisions, and the production rate of particles and decay rates.

Quarks	u (up)	c (charm)	t (top)
	d (down)	s (strange)	b (bottom)
Leptons	e^- (electron)	μ^- (muon)	τ^- (tau)
	ν_e (electron neutrino)	ν_μ (muon neutrino)	ν_τ (tau neutrino)
Gauge Bosons	g (gluon)		
	γ (photon)		
	W (W boson)		
	Z (Z boson)		
	H (Higgs boson)		

Table 2.1: Elementary particles described by the Standard Model. Not shown are the corresponding anti-particles.

			Q	I^3	Y
Leptons	left-handed	e, μ, τ	-1	$-1/2$	-1
		ν_e, ν_μ, ν_τ	0	$+1/2$	-1
	right-handed	e, μ, τ	-1	0	-2
Quarks	left-handed	u, c, t	$+2/3$	$+1/2$	$+1/3$
		d, s, b	$-1/3$	$-1/2$	$+1/3$
	right-handed	u, c, t	$+2/3$	0	$+4/3$
		d, s, b	$-1/3$	0	$-2/3$

Table 2.2: Electroweak quantum numbers of elementary particles: Q denotes the electric charge in units of e , I^3 the third component of the isospin and Y the hypercharge. Right-handed neutrinos are not known to exist.

All experimentally accessible properties of all known particles are well described. The known elementary particles (but not their corresponding anti-particles) are shown in Table 2.1.

The Standard Model postulates the quantum numbers weak isospin and hypercharge (for the electroweak interaction), shown in Table 2.2 and color (for the strong interaction). They correspond to associated conserved currents. Local gauge symmetries make them conserved locally by the introduction of gauge particles. These gauge particles carry energy and momentum, thereby introducing forces.

The electroweak part of the Standard Model describes the interaction of charged particles and fermions (particles with spin $1/2$) through the combined exchange of photons (for electrically charged particles) and W^\pm or Z particles (for particles with weak isospin charge) [84]. The contributions of these interactions interfere; depending on the interaction they can yield larger or smaller cross sections than the sum of the contributing cross sections involving any single gauge boson. As a crucial ingredient for massive W^\pm and Z particles, also the H boson interferes in processes with W^\pm and Z bosons.

As an example, quarks are charged fermions that are thus susceptible to the electroweak force; they are also carriers of the strong charge (color) and can thus interact through the strong force (even among themselves through self-interaction). Protons and antiprotons are examples of bound states of quarks; they thus interact through their constituents electroweakly and strongly.

Gravity is the only known “force” not covered by the Standard Model; additionally, the Standard Model cannot predict the particles’ masses.

2.1.1 The Higgs Mechanism

The Standard Model’s *Brout-Englert-Higgs mechanism* serves to explain rest masses of elementary particles [61]. This additional interaction yields a beautiful way to introduce particle masses, relating them to their respective coupling with the Higgs complex doublet scalar field. The Standard Model Brout-Englert-Higgs mechanism predicts one additional neutral particle, the Higgs boson H . Other theories and many extensions of the Standard Model require multiple Higgs bosons, e.g. the Minimal Supersymmetric Standard Model predicts two complex doublet fields resulting in three neutral and two oppositely charged Higgs bosons. The recent measurements of the neutral Higgs particle at the LHC confirm the Standard Model Higgs mechanism, and complete the particle spectrum of the Standard Model.

2.2 The $Z \rightarrow b\bar{b}$ Process

At lowest order in perturbation theory, the process $p\bar{p} \rightarrow Z \rightarrow b\bar{b}$ can be factorized into the production of Z via $p\bar{p} \rightarrow Z$, and its decay to a b -pair. However, this factorization holds only approximately: as shown in Fig. 2.1, this combination of initial and final state can also be obtained by the mediation of a (virtual) photon; the Z and γ processes interfere.

Subsequently, the b -quarks will hadronize and fragment into jets of stable and unstable particles. Depending on their lifetime, unstable particles can decay near the interaction point or somewhere in the detector, or they can escape or be absorbed by the detector before they decay. In reality, one generally only observes traces of the final state, and has to deduce how often the alluded process contributes to the observed final state.

There are several production mechanisms for b -jets, which will be discussed in the following section. An important feature of b -jet pairs is their invariant mass distribution in the final state, which will be used in this analysis to signal the Z boson as an intermediate state.

Final states with two b-jets, as relevant for this analysis, are not only produced by $Z/\gamma \rightarrow b\bar{b}$. There are several other processes that can yield two b-jets. They will be discussed as background in Section 2.5.

2.2.1 Event Topology, Notation

In the context of collider experiments, physics descriptions of events are invariant under rotations around the beam; this angle is denoted as ϕ . The only relevant measure for topologies in the ϕ axis is thus the distance of two objects in ϕ , provided that the detector response is uniform in ϕ .

The second dimension used to describe event topologies is orthogonal to ϕ .¹ The two axes meet at the nominal interaction point near the center of the detector. At hadron colliders, the hadrons' constituents (quarks or gluons) interact. The probability distribution of their relative momentum (with respect to the hadron's momentum) is described by *parton density functions (pdfs)*. As the interacting partons usually have different momenta, collisions exhibit a net boost along the beam axis.

There are two different measures for the direction orthogonal to ϕ : the geometrical angle θ describes the angle with the beam axis. An alternative measure is rapidity, introduced as $y = \frac{1}{2} \ln \left(\frac{E+p_z}{E-p_z} \right)$ with p_z being the momentum projected onto the beam axis. Describing event topologies in terms of rapidity is practical: the difference of rapidity of two particles is invariant under Lorentz boosts along the beam axis. Instead of rapidity, the simpler pseudo-rapidity $\eta = \frac{1}{2} \ln \left(\frac{|p|+p_z}{|p|-p_z} \right) = -\ln \left(\tan \left(\frac{\theta}{2} \right) \right)$ is often used. Rapidity and pseudo-rapidity are numerically close for light particles with high momentum. Both yield 0 for the direction perpendicular to the beam and $\pm\infty$ for particles parallel to the beam. For DØ the + sign is chosen in the direction of the proton beam.

As objects' distances in η and ϕ are relevant measures, the combined distance in η , ϕ space, ΔR can be useful. It is defined as $(\Delta R)^2 = (\Delta\eta)^2 + (\Delta\phi)^2$.

2.2.2 Z Production

By far the dominant fraction of interactions for $p\bar{p}$ collisions is due to the strong interaction. These interactions could in principle be described by QCD, but calculations

¹The radius from the detector is rarely used; as the charged particles are bent by the magnetic fields employed by most detectors, only their initial *direction* is relevant.

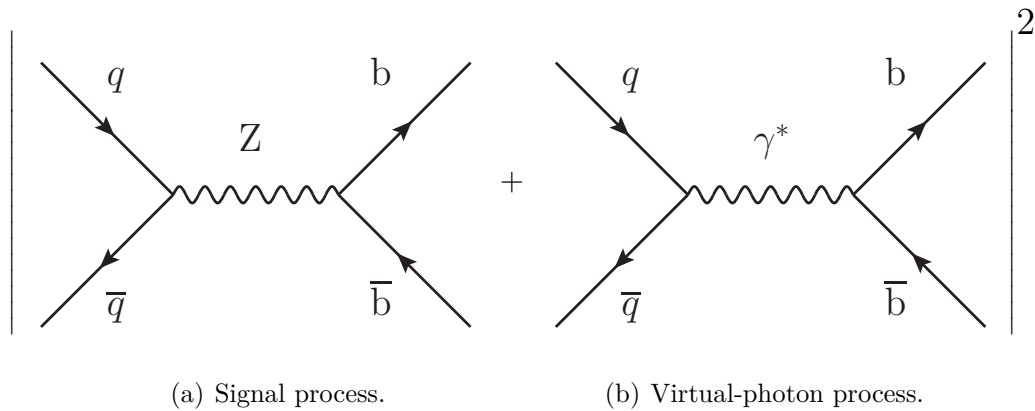


Figure 2.1: The tree level electroweak Feynman diagrams contributing to the signal cross section $p\bar{p} \rightarrow b\bar{b}$.

generally need to be done in perturbative QCD where the results are not always accurate. On the other hand, the production of a Z requires a “hard” (high Q^2) interaction, reducing the uncertainties on parton density functions considerably.

The process $p\bar{p} \rightarrow Z$ is modeled theoretically by the electroweak theory for which results can be calculated more reliably. Due to the high mass of the Z , the momentum scale involved is high enough to allow the use of perturbative QCD, for strong interaction effects in this reaction and for the prediction of the initial state parton momenta.

Within the electroweak framework, two different contributions for the $b\bar{b}$ -quark pair production exist: continuum production due to photon exchange, and resonant Z production, see Fig. 2.1(a), 2.1(b). These two electroweak contributions interfere, yielding a total cross section that differs from their sum.

2.2.3 The Z Decay

The Z boson decays into all possible pairs of elementary fermion-antifermion that are kinematically allowed, with branching ratios as shown in Table 2.3. The quarks’ color charge increases the relative phase space for decays into quarks, causing a higher decay width.

Z Decay Mode	Fraction [Γ_i/Γ , %]
e^+e^-	3.363 ± 0.004
$\mu^+\mu^-$	3.366 ± 0.007
$\tau^+\tau^-$	3.370 ± 0.008
$(u\bar{u} + c\bar{c})/2$	11.6 ± 0.6
$(d\bar{d} + s\bar{s} + b\bar{b})/3$	15.6 ± 0.4
$(b\bar{b})$	15.12 ± 0.05

Table 2.3: Visible Z branching ratios contributing above 1%, as given by [26].

2.2.4 The Z Resonance in $b\bar{b}$ Production

The tree level Feynman diagrams involving Z production and decay at the Tevatron are all similar to Fig. 2.1(a), except that the Z can decay to any fermion-antifermion pair, of which $b\bar{b}$ is only one example.

The invariant mass of the incoming interacting particles is $\sqrt{\hat{s}}$. The final state's invariant mass is expected to follow the initial state's invariant mass. As the Z is the intermediary particle for the final state, a Breit-Wigner peak is expected in the $b\bar{b}$ invariant mass at the Z-boson's mass $m_Z = 91.19 \text{ GeV}$ and with a width $\Gamma_Z = 2.50 \text{ GeV}$ [26].

2.2.5 Electroweak Contributions through Virtual Photons to the $b\bar{b}$ Production

In the non-resonant electromagnetic or QED contribution to the electroweak description of the $p\bar{p} \rightarrow Z$ process, two incoming quarks q and \bar{q} annihilate into a virtual, massive photon γ^* , see Fig. 2.1(b). This process is sometimes referred to as *Drell-Yan*, even though originally the Drell-Yan process meant lepton-pair production through virtual photons at hadron colliders. The virtual photon behaves just like a Z, it can for instance decay into a $b\bar{b}$ -jet pair. As the contributions from a virtual photon and Z production are indistinguishable, their contributions interfere. For low values of \hat{s} , the differential cross section $d\sigma/d\sqrt{\hat{s}} \propto \hat{s}^{-2}$ falls rapidly with the invariant mass of the virtual photon $\sqrt{\hat{s}}$, and thus the invariant mass of the final state jet pair. The contributions are clearly distinguishable on the parton level (Fig. 2.2).

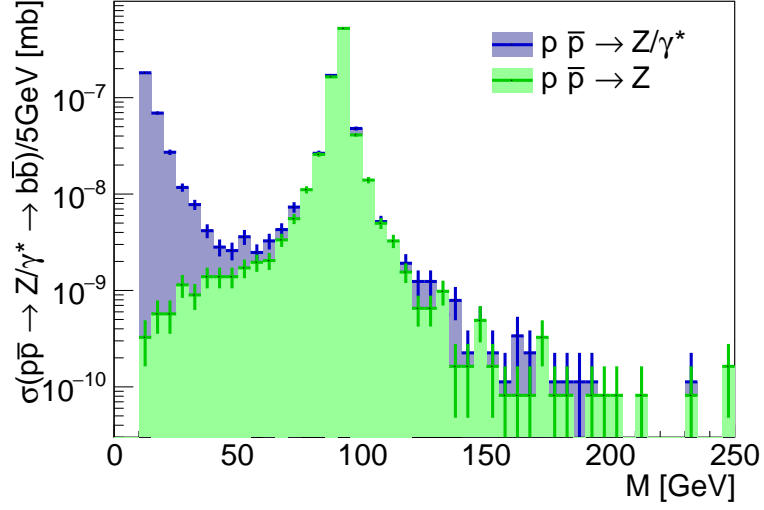


Figure 2.2: Monte Carlo prediction of the virtual photon contribution to the signal cross section; invariant mass at parton level. Pythia8 [78] samples with $\hat{p}_T > 10.$, `ffbar2gmZ = 0` and `WeakZ0:gmZmode = 0` (with Z/γ interference) versus 2 (pure Z contribution).

Fermion	Q	a	v
$e\mu\tau$	-1	$-\frac{1}{2}$	$-\frac{1}{2} + 2\sin^2\theta_W$
$\nu_e\nu_\mu\nu_\tau$	0	$\frac{1}{2}$	$\frac{1}{2}$
uct	$\frac{2}{3}$	$\frac{1}{2}$	$\frac{1}{2} - \frac{4}{3}\sin^2\theta_W$
dsb	$-\frac{1}{3}$	$-\frac{1}{2}$	$-\frac{1}{2} + \frac{2}{3}\sin^2\theta_W$

Table 2.4: The Z vertex factors for the electroweak interaction, adapted from [61]. θ_W denotes the weak mixing angle; $\sin^2\theta_W \approx 0.22$ [26].

2.2.6 Cross Section of $p\bar{p} \rightarrow b\bar{b}$

Within this process, production and decay cannot be decoupled; the interaction is characterized by the combination of them. The cross section of the electroweak process $q\bar{q} \rightarrow b\bar{b}$ can be calculated [15] as

$$\frac{d\sigma}{d\Omega} = \frac{\alpha^2}{4\hat{s}} \left(G_1(\hat{s}) \left(1 + \cos^2\theta \right) \dots \right) \quad (2.1)$$

with the ellipsis \dots denoting terms that are asymmetric in $\cos\theta$ and thus vanish upon integration over θ , and additional terms that depend on the parton masses. The contribution of the latter is negligible around the Z peak ($\hat{s} \approx m_Z^2$); any such term will be ignored in the following discussion.

The ratio of the Z over the photon propagator needed for G_1 is in its lowest order Breit-Wigner approximation

$$\chi_0(\hat{s}) = \frac{\hat{s}}{\hat{s} - M_Z^2 + iM_Z\Gamma_Z^0} \quad (2.2)$$

with

$$\Gamma_Z^0 = \sum_f N_C^f \frac{\alpha}{3} M_Z (v_f^2 + a_f^2) \quad (2.3)$$

(again ignoring terms that depend on the parton masses). N_C^f is the number of colors for the fermion f ; $N_C^f = 3$ for quarks and 1 for leptons. See Table 2.4 for the vector and axial coupling constants v_f and a_f .

This finally gives

$$G_1(\hat{s}) = Q_q^2 Q_b^2 + 2v_q v_b Q_q Q_b \text{Re}(\chi_0(\hat{s})) + (v_q^2 + a_q^2)(v_b^2 + a_b^2) |\chi_0(\hat{s})|^2 \quad (2.4)$$

See Table 2.4 for $Q_{b,q}$. Integrating over θ and convoluting with the parton density functions $f_{\bar{p} \rightarrow q_i}(x_i, \mu^2)$, $f_{p \rightarrow q_j}(x_j, \mu^2)$ (and similar for anti-quarks) for a $q_{i,j}$ -(anti)-quark to have momentum fraction $x_{i,j}$ when probing an (anti-)proton at the factorization scale μ , yields

$$d\sigma = \int_0^1 dx_1 dx_2 \sum_i \left(f_{p \rightarrow q_i}(x_1, \mu^2) f_{\bar{p} \rightarrow \bar{q}_i}(x_2, \mu^2) + f_{p \rightarrow \bar{q}_i}(x_1, \mu^2) f_{\bar{p} \rightarrow q_i}(x_2, \mu^2) \right) \frac{4\pi\alpha^2}{3\hat{s}} G_1(\hat{s}) \quad (2.5)$$

with the sum over the (anti-)proton's quark flavors, where the partonic center of mass energy squared \hat{s} is related to the $q\bar{q}$ center of mass energy squared s by $\hat{s} = x_1 x_2 s$.

In Equation 2.4, the term $2v_q v_b Q_q Q_b \text{Re}\chi_0(\hat{s})$ is the source of the interference. Note that the product $\text{Re}\chi_0(\hat{s})$ is positive for $\hat{s} > M_Z^2$ and negative for $\hat{s} < M_Z^2$. $v_q Q_q$ is positive for all flavors. The interference is thus constructive for $\hat{s} > M_Z^2$ and destructive for $\hat{s} < M_Z^2$.

The cross section plotted in Fig. 2.2 corresponds to the (QCD-) leading order contribution from Equation 2.5, while still modeling the Z/ γ^* interference. Despite the convolution with the parton density functions, the underlying scaling of $1/\hat{s}$ outside the Z resonance is still discernible.

2.2.7 Prediction of the $p\bar{p} \rightarrow Z$ Production Cross Section

Given a Z decay product, the total cross section to produce a Z boson from a $p\bar{p}$ collision can be determined by taking the branching fraction shown in Table 2.3 into account. This cross section times branching fraction has been measured at the Tevatron, using taus in the final state, as $\sigma(p\bar{p} \rightarrow Z/\gamma^*) \times Br(Z/\gamma^* \rightarrow \tau^+\tau^-) = 245 \pm 8(\text{stat}) \pm 12(\text{sys}) \pm 15(\text{lumi}) \text{ pb}$ [56] in the invariant mass window $60 < m_{\tau\tau} < 130 \text{ GeV}$ at $D\bar{O}$. A measurement at Tevatron's CDF combining the decays $Z/\gamma^* \rightarrow e^+e^-$ and $Z/\gamma^* \rightarrow \mu^+\mu^-$ yields $\sigma(p\bar{p} \rightarrow Z/\gamma^*) \times Br(Z/\gamma^* \rightarrow \ell^+\ell^-) = 254.9 \pm 3.3(\text{stat}) \pm 4.6(\text{sys}) \pm 15.2(\text{lumi}) \text{ pb}$ in the invariant mass range $66 \text{ GeV} < m_{\ell+\ell-} < 116$ [35].

A prediction of the production cross section for $\sigma(p\bar{p} \rightarrow Z)$ at $\sqrt{s} = 1.96 \text{ TeV}$ (i.e. without the contributions of virtual photons) has been calculated [72] using e.g. CTEQ6.1M and NNLO code by Hamberg et al. [62]: $\sigma^{\text{theory}}(p\bar{p} \rightarrow Z) = (7.178^{+0.028}_{-0.025}) \text{ nb}$. This predicts a cross section times branching ratio $\sigma^{\text{theory}}(p\bar{p} \rightarrow Z \rightarrow b\bar{b}) = (1.549^{+0.006}_{-0.005}) \text{ nb}$.

The analysis cannot distinguish the Z and virtual photon contributions from the Z/γ^* interference. Instead, it corrects the measured combined Z/γ^* contributions within the Z mass range in the Z mass window using a Monte Carlo prediction as described in Section 5.3.8.

2.3 Higgs Production

A standard Model Higgs-like particle with a mass of about $m_H = 125 \text{ GeV}$ has recently been observed by the ATLAS [17] and CMS [39] collaborations at the LHC. Such a Higgs boson has a large branching ratio for the $H \rightarrow b\bar{b}$ decay. Decays to heavier pairs, such as W^+W^- and $t\bar{t}$ force the H or its decay products to be off-shell, suppressing the branching ratio.

The sensitivity of the Tevatron Higgs analysis is highest for associated vector boson production, because the leptonic decays of the W or Z can relatively easily be detected. However, the direct production $p\bar{p} \rightarrow H \rightarrow b\bar{b}$ through gluon fusion has a much higher cross section, albeit negligible compared to $p\bar{p} \rightarrow Z \rightarrow b\bar{b}$.

Detecting the $Z \rightarrow b\bar{b}$ decay should also demonstrate the ability to detect the $H \rightarrow b\bar{b}$ process, see for instance Section 4.3.3.

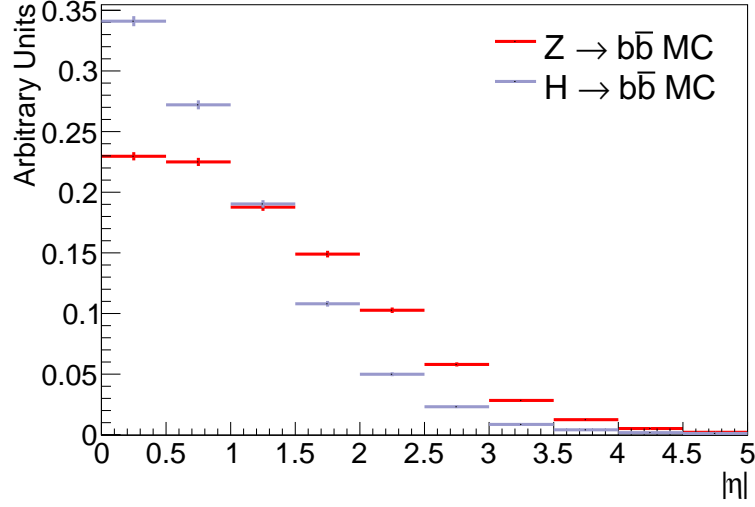


Figure 2.3: Pythia Monte Carlo prediction of the $|\eta|$ distribution of b-partons from a $Z \rightarrow b\bar{b}$ decay and from a $H \rightarrow b\bar{b}$ decay at $m_H = 126$ GeV.

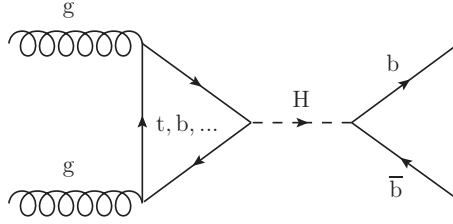


Figure 2.4: Tree level Feynman diagram for the process $gg \rightarrow H \rightarrow b\bar{b}$.

As both H and Z are bosons without electric or strong charge, their final state pairs of b-jets have similar properties. As shown in Fig. 2.3, for partons even the jets' rapidity distributions are expected to be similar compared to inclusive $b\bar{b}$ production, because both are color-neutral, and because both have similar invariant masses. There should thus be two resonances in the $b\bar{b}$ invariant mass spectrum. Note that some kinematic details of the two processes are different, due to the different spins of the H and Z.

The most significant evidence for a Higgs decaying to $b\bar{b}$ comes from measurements at the Tevatron [37]. A possible signal in this analysis would help in improving this Tevatron analysis, for instance by providing an “energy gauge”.

The major differences between $p\bar{p} \rightarrow H \rightarrow b\bar{b}$ and $p\bar{p} \rightarrow Z \rightarrow b\bar{b}$ are the production mechanism for the H and the Z bosons. While most of the Z bosons are produced by electroweakly fusing quarks at tree level, most of the H bosons are created by gluon fusion $gg \rightarrow H$ via a top quark loop, see Fig. 2.4. For a Standard Model Higgs of $m_H = 125$ GeV,

the production cross section at the Tevatron is expected to be $\sigma(\text{gg} \rightarrow \text{H}) \approx 0.6 \text{ pb}$, as calculated by [18] — only $\sim 10^{-4}$ of the expected production cross section of the Z boson. The large difference between these two cross sections stems from the loop-suppression of the Higgs production: it requires the creation of a massive intermediary particle, as shown in Fig. 2.4.

It should thus be easier to measure the Z resonance, and finding it is often seen as a prerequisite for finding the gluon-fusion Higgs process $\text{H} \rightarrow \text{b}\bar{\text{b}}$. The relevant issues are quality and knowledge of the detector response, the tools to extract the signal from the large amount of QCD inclusively produced b-jets. Even then, the process's small cross section makes large integrated luminosity a prerequisite for studying the Higgs (or indeed $\text{Z} \rightarrow \text{b}\bar{\text{b}}$). This will be provided by the LHC, while the Tevatron has been shut down in 2012, because it could no longer compete with the LHC.

2.4 Final State of the $\text{Z} \rightarrow \text{b}\bar{\text{b}}$ Process

This analysis uses measurements from the DØ detector. Detectors do not measure partons directly, for instance those produced by a $\text{p}\bar{\text{p}} \rightarrow \text{Z}/\gamma^* \rightarrow \text{b}\bar{\text{b}}$, but a final state consisting of particles produced from those partons. This section covers hadronization of b-partons and jet production.

2.4.1 Jet Production

Due to color confinement, one cannot detect separate (i.e. unbound) quarks but only color-neutral mesons and baryons. The conversion of a b- or $\bar{\text{b}}$ -quark to hadrons is modeled as hadronization and fragmentation: the number, the type, and the momentum of particles generated depends on the quark's momentum, flavor and the production environment of the quark. For a given quark momentum and flavor, probability distributions for fragmentation products can be measured e.g. in a clean two jet environment. The experimental reconstruction of jets will be discussed in Section 4.3.2.

The particles generated by fragmentation of one quark are relatively close together; for jets with energies relevant to this analysis, i.e. not too low, only a few percent of their energy is deposited outside a cone of $\Delta R < 1$. In perturbative QCD it is not easy to predict the probability distribution of gluons close to the outgoing quark [81]; instead, a

cut-off ΔR_{QCD} needs to be introduced. It allows us to integrate the probabilities for all generated particles within the cut-off; this region is taken as one physical object — the *jet*.

The exact cut-off cannot be defined purely by physical reasoning: it is impossible to decide whether a particle was generated as part of the fragmentation, before fragmentation began (*initial state radiation*, here: a gluon radiating off the incoming quark), or as a parton shower product of a particle that is part of the final state under study (*final state radiation*, here: a b-quark radiating off a gluon). These contributions interfere as they are indistinguishable. In practice, only hadrons are observed and hadronization confuses the issue further.

Algorithms have been developed to simulate these effects including fragmentation; some of them, like the Lund string fragmentation model [16], have become of common use. In the Lund string fragmentation model, the outgoing $q\bar{q}$ -pair is connected by the color charge. With their momentum pulling them apart, kinetic energy is converted into energy of the color field. This can be modeled as a massless “rubber” band or string that connects the two quarks. The string is assumed to have a constant tension; its end points can be interpreted as the quark antiquark pair.

The energy of the color field can generate a pair of quarks. They can cut the color connection of the quarks, “splitting” the string in two, and generating fragmentation mesons. This process can continue until the string energy is too low to generate new quarks and antiquarks. At these energies, the string starts acting as a glue between the quarks and a bound state develops.

Gluons are modeled as string excitations, which complicates the otherwise simple model. The model assumes that the quarks are massless. Heavy quark masses need to be taken into account by introducing corrections, such as the Bowler string model for Pythia [77].

Several parameters are needed for the string fragmentation models. Examples are the cut-off energy where fragmentation stops, the fraction of the available energy that a newly created hadron takes, the probability for producing a quark depending on its flavor, the time-scale of the fragmentation (the fragmentation procedure assumes particles with a lifetime larger than this time-scale to be stable), the ratio of di-quark anti-di-quark production versus quark antiquark production and of course the quark masses. The parameters’ values used in this analysis depend on the Monte Carlo model that is used and will be introduced in Section 3.8.1.

b-Hadron	Fraction [%]	Lifetime [ps]
B^+	40.3 ± 0.9	1.641 ± 0.008
B^0		1.519 ± 0.007
B_s^0	10.3 ± 0.9	1.466 ± 0.031
Λ_b	9.0 ± 1.5	1.425 ± 0.032

Table 2.5: Relative occurrence of weakly decaying b-hadrons (including their charge conjugates) in $Z \rightarrow b\bar{b}$ decays and lifetimes, as given by [26].

2.4.2 b-Hadrons

For b-quarks, all of these final states, however they were produced, have b-hadrons that are produced as part of a jet. Most often, these b-hadrons are produced in an excited state like B^* , Ξ_b , etc. They decay by radiating off photons or hadrons (mostly pions) to a b-flavored hadron with lowest mass, i.e. B^\pm , B^0 , B_s^0 , or Λ_b . Both the electromagnetic decay and the decay via the strong interaction are almost instantaneous: they have a decay time of less than 10^{-20} s.

The jet is generated partly by the hadronization of the initial b-quark and partly by the b-hadron's de-excitation and decay. The average jet has slightly more particles stemming from hadronization than from the hadron's decay. Most often the de-excited hadrons are a B- or \bar{B} -meson, which are the lightest and thus most probable form of a quasi-stable b-flavored hadron. Table 2.5 shows the relative occurrence of the different weakly decaying b-hadrons in the $Z \rightarrow b\bar{b}$ decay. The production mechanism is expected not to influence the relative abundance. For this analysis, the different b-hadrons will be indistinguishable.

We make use of two ways to tell a b-hadron apart from lighter hadrons: its lifetime and its decay modes.

Lifetime

The b-hadrons listed in Table 2.5 are the end of the fast strong and electromagnetic decay chains of b-flavored hadrons. They owe their relatively long lifetime to the lack of decay modes: they have to decay weakly via the W^\pm boson. Additionally, this process is CKM suppressed as it involves a change of quark generation, or a non-tree-level process in the

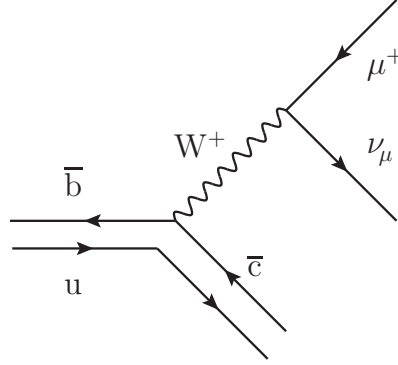


Figure 2.5: Example of a tree level Feynman diagram for the semi-leptonic decay of a B^+ .

case of the flavor changing neutral current process $b \rightarrow s$. The different (non-charm) B-mesons lifetimes range from 1.42 ps to 1.64 ps, as shown in Table 2.5.

In the particle's own rest frame, the average B-lifetime translates to an expected proper decay length of $c\tau = (461 \pm 5) \mu\text{m}$, compared to $(468^{+95}_{-75}(\text{stat.}) \pm 39(\text{syst.})) \mu\text{m}$ as measured at DØ [20]. The length in the detector rest frame that a particle with a given lifetime can travel before decaying depends on the particle's Lorentz-boost. For a jet selection and event topology similar to the one used in this analysis, the proper decay length is dilated to physical decay lengths of the order of millimeters.

Most other unstable particles decay either almost instantaneously (e.g. the Z-boson, the t-quark, the J/ψ -meson, and excited hadrons) or after centimeters and longer (e.g. the K_L^0 -meson and even the K_S^0 -meson, the μ -lepton, and the π -meson).

The τ -lepton and the D^\pm are the most relevant examples of particles with a comparable lifetime to the B-mesons: 0.2906 ± 0.0010 ps for the τ and 1.040 ± 0.007 ps for the D^\pm [26]. The probability to reconstruct them, though, is far smaller than for a b-hadron, because their major decay modes involve only few charged decay products. The b-hadrons, on the other hand, have on average about 5.5 charged long-lived decay products (cascade products included) [74].

This secondary vertex with many particles allows specific experimental techniques for b-hadron identification, see Section 4.3.3.

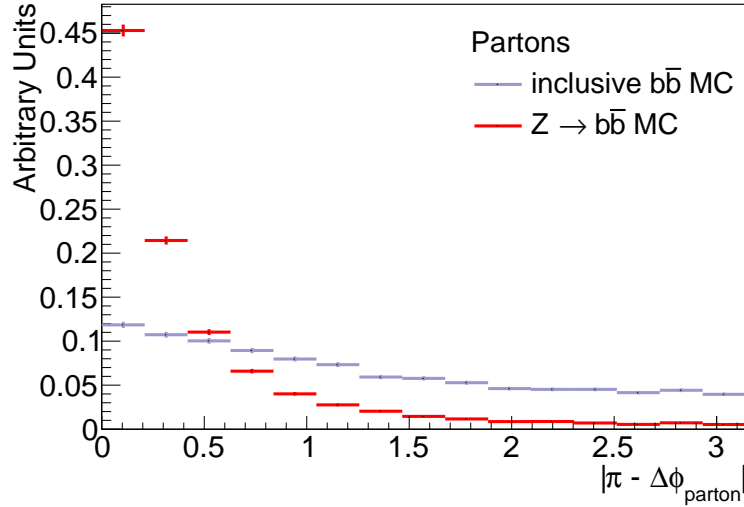


Figure 2.6: Pythia Monte Carlo prediction of the $|\pi - \Delta\phi|$ distribution between b-parton pairs, from a $Z \rightarrow b\bar{b}$ decay and from inclusive b production (i.e. having any b-quark in the final state).

Semi-Leptonic Decay

A considerable fraction of b-hadrons decays into a lepton, a neutrino, and light (non-b-flavored) hadrons. One such decay is $B^+ \rightarrow \bar{D}^0 \mu^+ \nu_\mu$, see the Feynman diagram Fig. 2.5. Of all B^+ -meson decays, $2 * (10.99 \pm 0.28) \%$ are semi-leptonic decays [26] into electrons or muons. The semi-leptonic decay rates of B^0 , B_s^0 and Λ_b are similar to that of the B^+ -meson.

Most leptons that are part of b-jets are produced as decay products of the initial b-hadron, either directly or by a cascade decay involving a c-quark, e.g. $B^- \rightarrow D^0 X \rightarrow K^- \mu^+ \nu_\mu X$.

Almost 100% of all B^\pm -mesons decay to charmed mesons. Thus, cascaded decays $B^+ \rightarrow \bar{D}^0 + X \rightarrow \mu^- + X$ are frequent: about 6% of all B^\pm decay to a μ via a D^0 or \bar{D}^0 . The intermediate D^0 is not identified in the analysis. This virtually doubles the apparent probability of a b-hadron to decay to a μ . Similar arguments hold for B^0 , B_s^0 and Λ_b .

2.4.3 Azimuthal Jet Separation

For a two-body hard scatter, the azimuthal separation of the outgoing partons is expected to be $\Delta\phi = \pi$. Higher order radiative processes can create outgoing momentum flow that is not detected, for instance because its energy is too low or because the jet is too

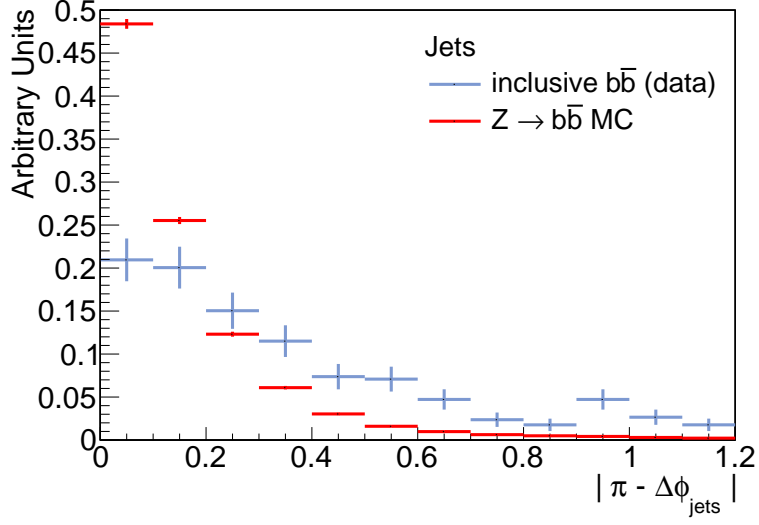


Figure 2.7: Pythia Monte Carlo prediction of the $|\pi - \Delta\phi|$ distribution between b-jets from a $Z \rightarrow b\bar{b}$ decay, and of b-tagged jet pairs from data.

forward to be measured. These effects dilute the azimuthal separation into a distribution with a maximum at $\Delta\phi = \pi$.

The Monte Carlo prediction for the azimuthal separation, $\Delta\phi$, of the $b\bar{b}$ -parton pair produced by inclusive QCD production in comparison to $b\bar{b}$ -partons from $Z \rightarrow b\bar{b}$ decays is shown in Fig. 2.6. The inclusive b-simulation used for Fig. 2.6 required a minimal $\hat{p}_T = 10 \text{ GeV}$; shown is the separation of the two leading b-partons (i.e. before hadronization); no further event selections were applied.

The Monte Carlo prediction for the azimuthal separation of two b-jets stemming from Z-bosons versus the measured separation for b-tagged jets from data is shown in Fig. 2.7. Monte Carlo predicts a wider $|\pi - \Delta\phi|$ distribution for inclusive b-jet pairs than for b-jet pairs from Z decays.

Color flow between an incoming particle and the outgoing b-jets can influence the $\Delta\phi$ distribution. The $Z \rightarrow b\bar{b}$ is color neutral, “cutting” a color connection between the beam’s interaction remnants and the b-jets. Inclusive b production on the other hand involves (many) gluons and thus color flow. This will be used to distinguish QCD and Z production later.

2.5 b-Jet Production through the Strong Interaction

For this analysis, *background* consists of two jets that are identified as b-jets, and that are not produced by the decay of a Z. There are several sources for this background, the most relevant being:

- production of a $b\bar{b}$ -jet pair by virtual photons, as discussed in Section 2.2.2,
- production of a $b\bar{b}$ -jet pair via the strong interaction,
- misidentification of a pair of light jets as b-jets. These light jets are produced dominantly by direct QCD processes,
- misidentification of one light jet as a b-jet, where the opposite jet is a merged jet from b and \bar{b} decays, or a single b-jet where the matching b-jet remained undetected.

This analysis uses a combination of Monte Carlo predictions for these backgrounds (for instance for jets from virtual photons) and measurements from data. To study and reduce the backgrounds using data, events will be characterized by decay products (light and heavy jets, leptons, and long lived particles). This characterization will be discussed in the following sub-sections.

2.5.1 Strong Production

Di-jet production described by QCD (see Fig. 2.8) exhibits a monotonically falling invariant mass distribution above twice the b-mass. The invariant mass distribution of resonant production via an intermediary particle peaks near the intermediary particle's mass due to its propagator structure. For photons and gluons as intermediary particles, the peaking at zero shows as a monotonically falling distribution in $\sqrt{\hat{s}}$; see for instance Section 2.2.5. At large invariant mass $m_{jj} \gg m_q$, jets of all flavors are expected to have a similar di-jet invariant mass distribution.

At energies relevant for Z production, though, the different production mechanisms have slightly different contributions to the di-jet invariant mass distribution for light and heavy flavored jets — different in both normalization and shape. Only the shape of the invariant mass spectrum is relevant for this analysis; its flavor dependence is studied using data.

2.5.2 Light Flavor Contribution

Light flavor contributions are dominantly produced by the strong interaction. At DØ, the production of a light quark jet of 30 GeV is about 500 times more probable than the production of a b-jet of the same energy, as discussed in [66]. Even if the b-jet identification is tuned to yield only a small misidentification probability for light quark jets, the enormous amount of light jets compared to b-jets turns that small probability to misidentify a light jet as a b-jet into a considerable source of background events. Due to the semi-leptonic b-jet identification used in this analysis (see Section 4.3.3), the light jet production of leptons and long-lived particles contributes most to this background after b-jet identification.

Lepton Production

Leptons can be produced in light quark jets as decay products. Sources are the decay of heavy quark states, e.g. $J/\psi \rightarrow \mu^+\mu^-$, and π and K decays, e.g. $\pi^+ \rightarrow \mu^+\nu_\mu$.

Muons from light and b-jets can be distinguished using the p_T^{rel} parameter, the momentum fraction of the muon that is orthogonal to the jet axis. This parameter determines the “softness” of the lepton with respect to a jet; while muons commonly carry a small fraction of a decay’s momentum orthogonal to the jet, the high mass difference of the B and its decay products will result in muons with on average larger p_T^{rel} . Muons from charm decay tend to have a p_T^{rel} value intermediately between those from b-hadrons and light flavour decays. The p_T^{rel} spectrum can be decomposed to statistically distinguish b-hadrons from c-hadrons and from light quark hadrons as the parent of the lepton.

2.5.3 Heavy Flavor Contribution

The total production of b-jets by QCD and other mechanisms is called *inclusive* b-jet production. As shown in Fig. 2.8 and Fig. 2.9, several leading and sub-leading contributions to inclusive b-jet production can be distinguished, depending on the type of QCD interaction:

- *direct production* generates a $b\bar{b}$ pair from a $q\bar{q}$ interaction of the incoming $p\bar{p}$ beam particles (Fig. 2.8),
- b-quarks can be produced by a final state *gluon splitting* into a $b\bar{b}$ pair (Fig. 2.9(a)),

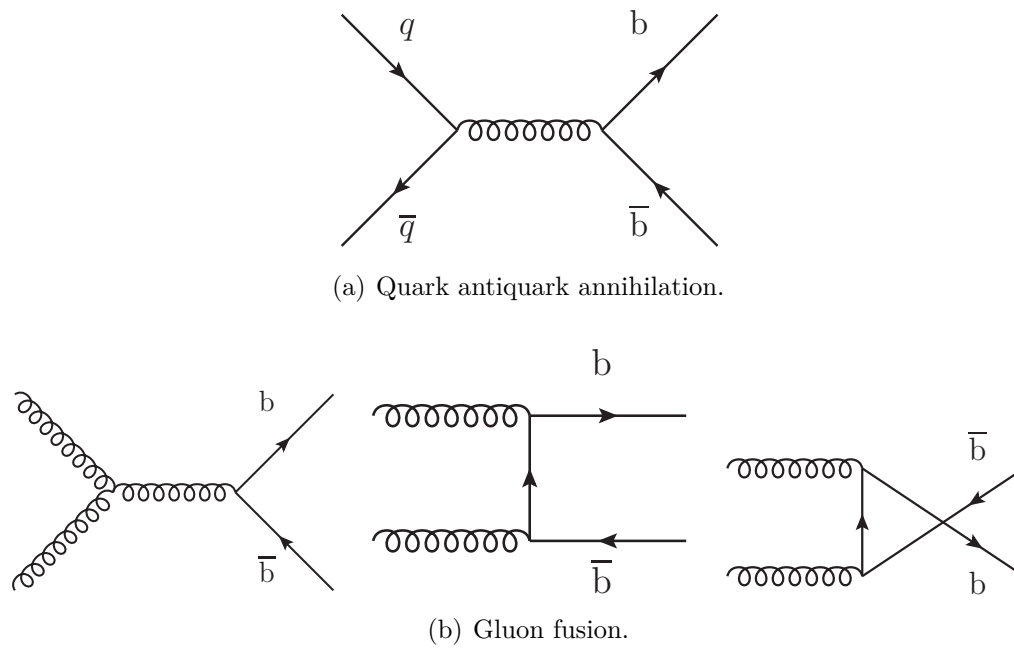


Figure 2.8: Direct b-quark production in leading order QCD.

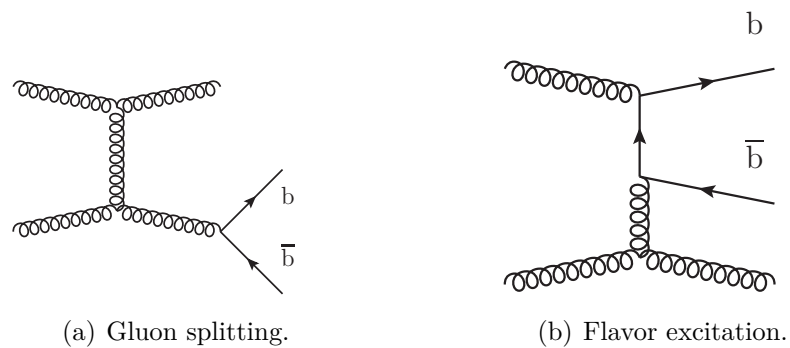


Figure 2.9: b-quark production in next to leading order QCD.

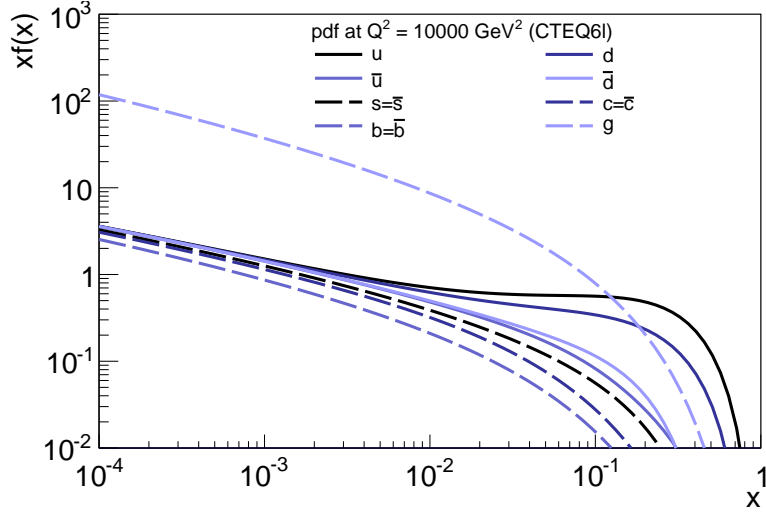


Figure 2.10: CTEQ6l parametrizations of the parton densities for $Q^2 = 10000 \text{ GeV}^2$, a typical value at the Tevatron for a process with a di-jet invariant mass of the order of 100 GeV.

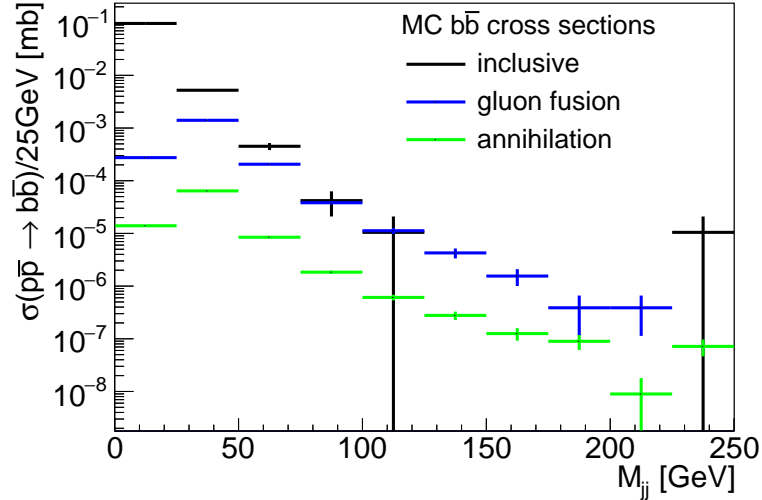


Figure 2.11: Monte Carlo prediction (Pythia8) of QCD $p\bar{p} \rightarrow b\bar{b}$ production cross sections for different mechanisms versus the resulting di-parton invariant mass. Due to limited statistics in the inclusive sample, no data points have passed the event selection in the range $125 \text{ GeV} < m_{jj} < 225 \text{ GeV}$.

- *flavor excitation* causes one incoming gluon to split into a $b\bar{b}$ pair, of which one interacts with a second incoming gluon (Fig. 2.9(b)).

The relative contributions of these production mechanisms change as a function of the invariant mass of the resulting di-parton system, as shown in Fig. 2.11. This prediction was done with Pythia8 [78] using a $\hat{p}_T^{\text{min}} = 10 \text{ GeV}$, no hadronization, and with soft QCD

interactions for the inclusive cross section. The distribution labeled as $q\bar{q}$ corresponds to Fig. 2.8a; gg corresponds to gluon fusion as shown in Fig. 2.8b. The difference to the total cross section is due to higher order production mechanisms (notably flavor excitation) and interference.

The colliding protons' quark and gluon momentum distributions (parton density functions, pdfs) favor a small invariant mass, as shown in Fig. 2.10. Because of the different masses of light and b-quarks and different relative occurrences of production processes, interactions producing light jets have a different invariant mass distribution than those producing b-jets. The “valence” u- and d-quarks have a much higher probability to interact with a significant fraction of the proton momentum than b-quarks and gluons. Most b-quarks in final states are produced through quark annihilation, whereas light flavor events are dominantly produced by “t-channel” elastic scattering. The flavor dependent differences of invariant mass spectra will be studied as part of the signal extraction procedure.

Given a color configuration of the initial and final state quarks, one can unambiguously determine whether a tree level process involved a Z or photon: the color-neutral Z-boson or photon “cuts” the color connection of the incoming and the outgoing quarks. Most of the other processes leave the outgoing quarks color connected; even though higher order processes can generate color neutral quark pairs.

For tree-level Z production, the incoming $q\bar{q}$ -pair must thus have a color-anti-color state. Gluons, on the other hand, will carry a color charge. This also explains why there is practically no interference between the processes $p\bar{p} \rightarrow Z \rightarrow b\bar{b}$ and $p\bar{p} \rightarrow g \rightarrow b\bar{b}$; to first order, both processes add incoherently.

A relevant higher order process for Z production via gluon fusion is shown in the two right diagrams of Fig. 2.8b. These processes have a relatively low contribution to the overall production; the above statement thus holds for the vast majority of QCD produced $b\bar{b}$ -pairs.

A b-jet stemming from QCD production is thus generally color-connected with the remnants of the interaction, which usually do not pick up enough transverse momentum to be measured. In clean environments, this color connection can be seen by energy deposits between the jet and the beam. It provides a means of separating QCD-generated b-jets and b-jets produced without color-flow, as e.g. by a decaying Z-boson, by vetoing events with energy deposits between jets and the remnants of the incoming partons. A preliminary study showed that the suppression power of this criterion is not sufficient

at $D\bar{O}$ to be useful. This can be explained by the hadron collider environment, which provokes energy deposits, e.g. due to underlying and overlapping events. In addition, also within QCD parton final states can be produced without apparent color connection to the initial state, the so called rapidity gap events [43].

Azimuthal Jet Separation

The separation of two b-jets stemming from a Z has been described in Section 2.4.3. For a $b\bar{b}$ -jet pair generated by a QCD process, the azimuthal difference (i.e. $\Delta\phi$) distribution is more complex. The different leading and sub-leading processes have different contributions to the distribution. The leading order $2 \rightarrow 2$ processes $q\bar{q} \rightarrow b\bar{b}$ and $gg \rightarrow b\bar{b}$ (flavor creation) have an azimuthal distribution similar to that of the $Z \rightarrow b\bar{b}$ process (except for contributions from color connection of the $b\bar{b}$ QCD production). The $2 \rightarrow 3$ processes (for instance gluon splitting) on the other hand, but also initial or final state showering of $2 \rightarrow 2$ processes, contribute to a much wider azimuthal distribution, due to one or more extra outgoing particles.

Detailed studies of the different contributions to the kinematic distributions can be found in [86] and [67]. The distribution of the azimuthal jet separation can be seen in Fig. 2.7. Monte Carlo simulation of the di-jet separation for inclusive $b\bar{b}$ events is known to not describe data well [73]; the distribution has thus been measured on data. For jet pairs from inclusive b production, the width of a Gaussian fit centered at $\Delta\phi = \pi$ is $\sigma = 0.23$, while for jet pairs stemming from a $Z \rightarrow b\bar{b}$ decay this width is $\sigma = 0.15$.

2.5.4 Mixed Flavor Contribution

Light jets can be misidentified as b-jets. If in a two-jet event the other jet contains at least one b-hadron, then this event is part of the *mixed flavor* background. There are several mechanisms for producing this kind of background:

For b-jet production, the two b-jets are sometimes too collinear to be identified as separate jets. To balance p_T , this joint $b\bar{b}$ -jet is opposite another jet, which is usually a light flavored jet, for instance a gluon jet. The $b\bar{b}$ -jet is likely identified as b-jet: its high multiplicity increases the probability to have many large impact parameter tracks, and its two b-hadrons can each decay into a muon, doubling the probability for a muon based b-identification to succeed.

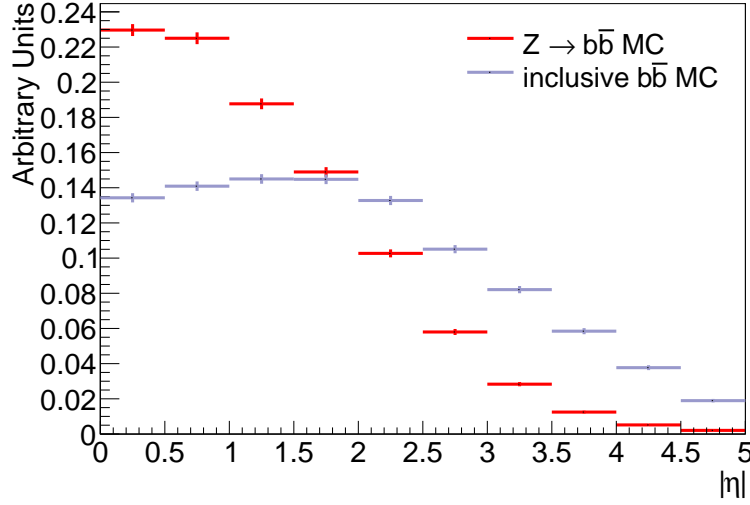


Figure 2.12: Pythia Monte Carlo prediction of the $|\eta|$ distribution for partons from a $Z \rightarrow b\bar{b}$ decay and inclusive b production.

Another possible cause for a mixed flavor jet pair is that one b -jet has a rapidity too high to be detectable, i.e. it does not leave the beam pipe within the detector, while the other b -jet appears in the normal acceptance. The p_T of the jet inside the acceptance is then balanced by a light flavored or gluon jet. This type of event is very rare, because most of the phase space is covered by the detector (up to $|\eta| \lesssim 4$), and most of the b -partons are created at lower rapidities as shown in Fig. 2.12.

This analysis requires both jets to be identified as b -jets. Mixed flavor events can only pass the event selection if the light jet is misidentified as a b -jet. Taking into account that mixed flavor events are less probable than “pure” di- b -jet events (because they are a small sub-class of di- b -jet events), and the suppression from the small misidentification probability, the background from mixed flavor events is expected not to influence the result of the analysis.

Chapter 3

The DØ Detector

The DØ detector is a traditional symmetric, full-coverage (4π) detector. It was first producing physics results in the data-taking period of 1985 to 1996, known as Run I. The most spectacular result of Run I was undoubtedly the discovery of the top quark.

Since then it has undergone an upgrade, adding key elements like a magnetic field in the central detector. Physics data-taking for Run II started in April 2002, and continued until September 2011. The detector setup used to collect this analysis' data (Run IIa) is described in the following sections.

The Run IIa detector was designed to study processes that are created in symmetric $p\bar{p}$ collisions at a center-of-mass energy of $\sqrt{s} = 1.96$ TeV. The protons and antiprotons were delivered by Fermilab's Tevatron accelerator complex, which will be described in the following.

3.1 The Tevatron

Fermilab's accelerator complex and its storage ring Tevatron combine all the ingredients from proton extraction, antiproton production, acceleration, cooling, to storage. An overview of the Fermilab accelerator complex is shown in Fig. 3.1.

3.1.1 Proton Production and Acceleration

Protons are ionized by adding an electron to form H^- -ions using a Cesium catalyzer. The H^- -ions are accelerated by a Cockroft-Walton accelerator to 750 kV. Subsequently, they

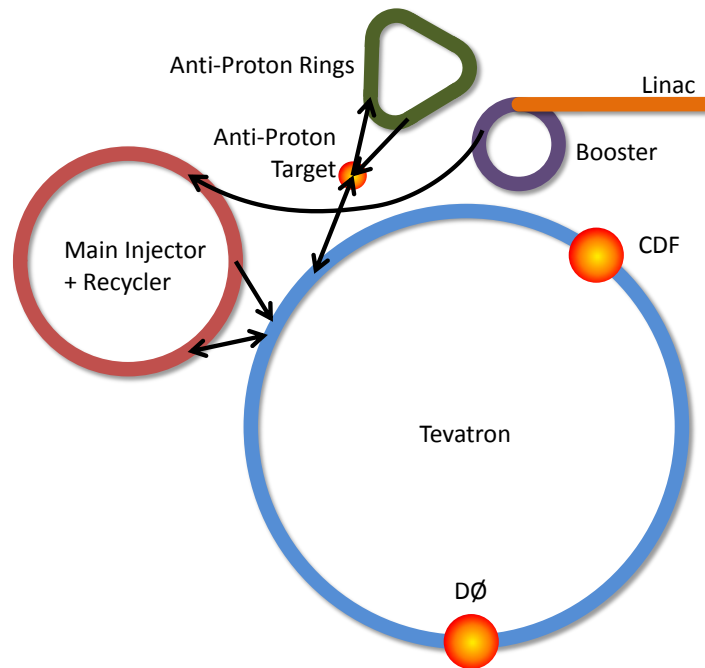


Figure 3.1: Schematic view of Fermilab's particle accelerator and storage complex.

are accelerated in an Alvarez-style Linac (linear accelerator). Here, bunches of H^- -ions are created due to the acceleration by electromagnetic radio frequency waves (RF). In the Booster, the H^- -ions are coalesced with bunches of protons already in the machine to collect high current bunches. The electrons are then stripped off the hydrogen ion by passing them through a carbon foil, leaving bare protons. The Booster is the first synchrotron the protons see. It accelerates the protons from 400 MeV to 8 GeV.

The next stage of acceleration is the Main Injector which yields 150 GeV protons for the Tevatron. It injects the protons into the Tevatron synchrotron where they get accelerated to the final energy of 980 GeV. The Tevatron was the first synchrotron that used superconducting magnets operated at liquid He temperature to conserve energy. It has a radius of 1 km, and accommodates the two collider experiments DØ and CDF.

3.1.2 Anti-Proton Production and Acceleration

In principle one could collide protons against protons as for instance at CERN's LHC. This requires magnets with two separate fields, as the colliding proton beams point into opposite direction, and thus need opposite fields to bend them into the same ring. The

Tevatron collides a proton against an antiproton beam, which allows it to use the same set of magnets for both.

Anti-protons are created from 120 GeV protons coming from the Main Injector, which are directed onto a fixed Nickel target. The production efficiency (rate of antiprotons per incoming protons) for antiprotons above 8 GeV is only about $20 \cdot 10^{-6}$. These antiprotons are focused into the beam line using a Lithium cylinder with a high current of 650 kA. Lithium is used as the metal, as it is light enough to reduce the probability of the antiprotons to interact with the cylinder. The high current provides a lensing effect for the antiprotons. Other particles created by the collision of the protons onto the Nickel target are removed from the beam, using a bending magnet as a charge/mass spectrometer.

The antiprotons are bunched, due to the bunching of the initial protons. Being products of a fixed target reaction, they have a very inhomogeneous energy distribution, which is difficult to handle for accelerators. The next stage of the antiproton production, the synchrotron called Debuncher reduces the energy spread of the protons, by forcing a common RF phase onto them, which decelerates the high-energy antiprotons and accelerates the low-energy ones. This in turn dissolves the bunches, as the higher-energy antiprotons need to be directed through a loop with a higher radius, which translates to lower turning frequencies.

The Debuncher and also the following stage, the Accumulator, use Van-der-Meer stochastic cooling to reduce the inhomogeneity of the antiproton momenta, by manipulating the antiprotons' orbits using a kicker magnet operated on feedback signals from lateral displacement [76]. The Accumulator collects the Debuncher's antiproton output over a period of many hours up to days. This accumulation is known as *stacking*. Once the amount of collected antiprotons is high enough to allow a reasonably high collision luminosity they get transferred to the Main Injector, which in turn injects them into the Tevatron — just like protons, only in the opposite direction.

The Recycler ring acts as a spill-over for antiprotons from the Accumulator: after a certain amount of collected antiprotons, stacking becomes inefficient, and the antiprotons are transferred into the Recycler. It is a simple, highly reliable storage ring, which uses permanent magnets to make it more robust against power failures.

This complex chain of accelerator modules allowed peak luminosities of $3 \cdot 10^{32} \text{ cm}^{-2} \text{ s}^{-1}$ and a total Run II integrated luminosity of 12 fb^{-1} . For the analysis in this thesis, the

data collected up to 2004 were used: after this date the trigger changed, making this a natural cut-off date. Even later, also the detector itself was modified.

3.1.3 Beam Characteristics

The Tevatron’s accelerating RF waves have stable regions for protons and antiprotons where acceleration and deceleration match; leading particles will be slowed down, trailing particles will be accelerated. These regions are called *buckets*. At the injection energy from the Main Injector, each of them is approximately 18.87 ns long. Their length decreases with increased beam energy, resulting — after focussing — in a luminous region within the detector of approximately 30 cm.

The groups of protons and antiprotons that are assembled in the buckets are usually called *bunches*. Before injecting beam (in *shots*) into the Tevatron, several buckets are combined (*coalesced*) into four bunches in the Main Injector. This coalescing empties six out of seven consecutive buckets. The group of one filled bucket and the following six empty buckets is referred to as a *tick*. The ring holds 1113 buckets, and thus 159 ticks.

After injection, the Tevatron stores 36 bunches of protons and 36 bunches of antiprotons. These bunches are grouped into 3 consecutive and symmetrically spaced *trains*; each pair is separated by empty buckets of approximately 2.64 μs — the reaction time for the beam abort system. Each bunch is separated by two empty ticks within one superbunch; the bunch crossing intervals are thus at least 396 ns.

There can be wide variations of particle densities between crossings of the different proton and antiproton bunches, which has implications for the luminosity, as outlined in Section 3.6. The luminosity \mathcal{L} quantifies the expected number of events N per unit time for a given cross section σ : $N = \mathcal{L}\sigma$. The total luminosity in the Tevatron is mainly limited by the number of available antiprotons.

3.2 The DØ Detector

The DØ detector has a traditional layered, “onion-style” layout [47]. As shown in Fig. 3.2, its central part is the tracking system, with the silicon microstrip tracker surrounded by the central fiber tracker. This tracking system is embedded in the solenoid magnet.

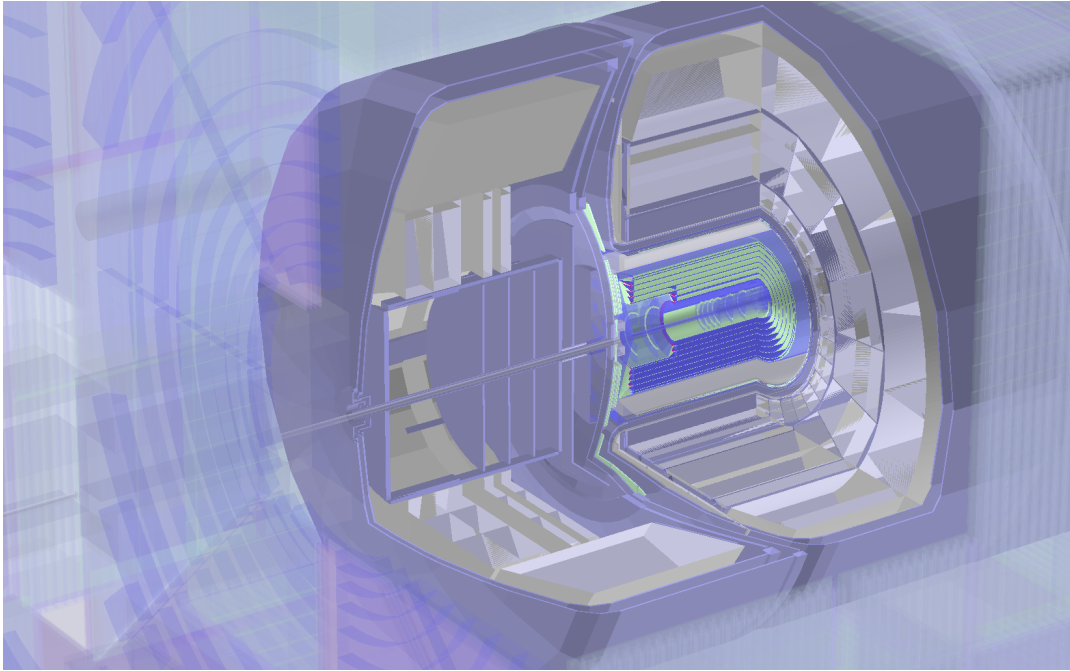


Figure 3.2: Schematic view of the DØ detector.

Outside the solenoid, the calorimeters follow. They are surrounded by muon detectors which are interspersed by the toroid magnet.

3.3 Tracking

The tracking system consists of a silicon microstrip detector in the inner part, surrounded by a scintillating fiber tracker; both are surrounded by a solenoid magnet to bend particles depending on their momentum.

3.3.1 Solenoid Magnet

The solenoid is a superconducting magnet producing a 2 T magnetic field in the direction of the beam axis z . It is built as a two layer coil with a mean radius of 60 cm, accounting for a total thickness (coil and cryostat) of about 0.9 radiation lengths. The magnet does not use a field-shaping iron return yoke; instead, higher current conductors are used at the ends of the coil to reach a field uniformity of $\sin \theta \int B_z dl < 0.5\%$ and to increase the momentum resolution for particle tracks. The experiment uses a coordinate system with an origin in the nominal interaction point and the following bases: the z -axis is the

detector's symmetry axis along the beam line; ϕ is the angle around that z -axis, starting at zero in the direction pointing to the middle of the Tevatron and becoming positive in the upward direction; θ is the angle with the positive z -axis.

The solenoid is operated close to its maximum current of about 4800 A; during operation it stores an energy of 5 MJ. Its polarity is flipped every two weeks to reduce systematic effects like forward-backward asymmetries. Before it was put to use, the magnet's field was precisely mapped inside the magnet's enclosed volume. Hall probes are used to measure the magnetic field stability at several positions inside the tracking volume during detector operation.

3.3.2 Silicon Microstrip Tracker

As the tracking detector closest to the beam pipe, the Silicon Microstrip Tracker (SMT) [46, 50] collects signals of penetrating charged particles. It has a total of 800,000 readout channels spread over 6 barrels (around the beam) and 16 disks (perpendicular to the beam), as shown in Fig. 3.3.

The barrels each consist of eight layers of detector modules (*ladders*); they are grouped into four *super-layers*, each covering the whole ϕ -range by means of overlaps, as shown in Fig. 3.4. The barrels cover the rapidity region $-1.5 < \eta < 1.5$. The layers' distance from the nominal beam center is between 2.715 cm for the inner layer and 10.51 cm for the outer layer.

A ladder consists of two silicon sensors mounted side-by-side nearly touching at their short sides. Each sensor is 6 cm long, 2.1 cm wide, and 300 μm thick. Most sensors have readout strips on both the inner and the outer side; only the first and third super-layers of the outer-most barrels contain single-sided sensors. All barrels have readout strips in the z direction, allowing precise measurements of the hit position in the ϕ direction. The first and third barrel layers have sensors that also have 90° stereo angle strips, allowing precise measurements of the hit position in the z direction. The second and fourth barrel layers of the four inner barrels have 2° stereo angle strips, providing an improved vertex resolution, for instance to separate primary vertices. The position in the radial direction is given by the radial position of the detector wafer.

There are two types of disks: of the total of twelve F-disks four are in between each pair of barrels except at $\eta = 0$. An additional four disks are on each outer end in z of the barrels. The F-disks are made of twelve slightly overlapping wedges of double-sided

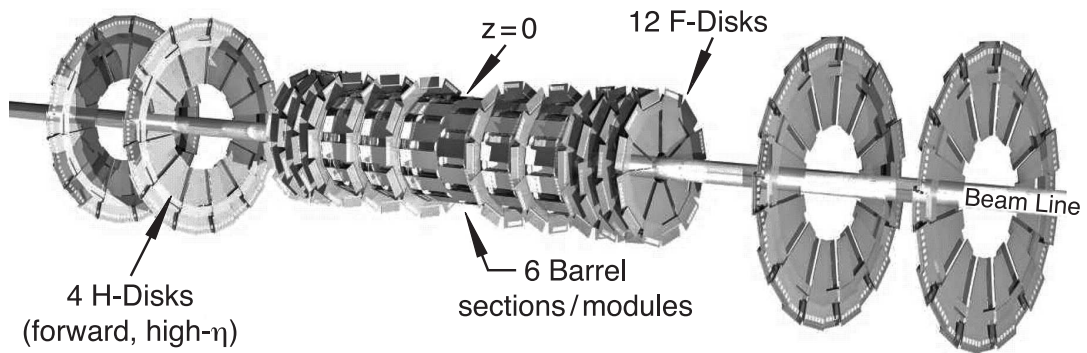


Figure 3.3: The Silicon Microstrip detector.

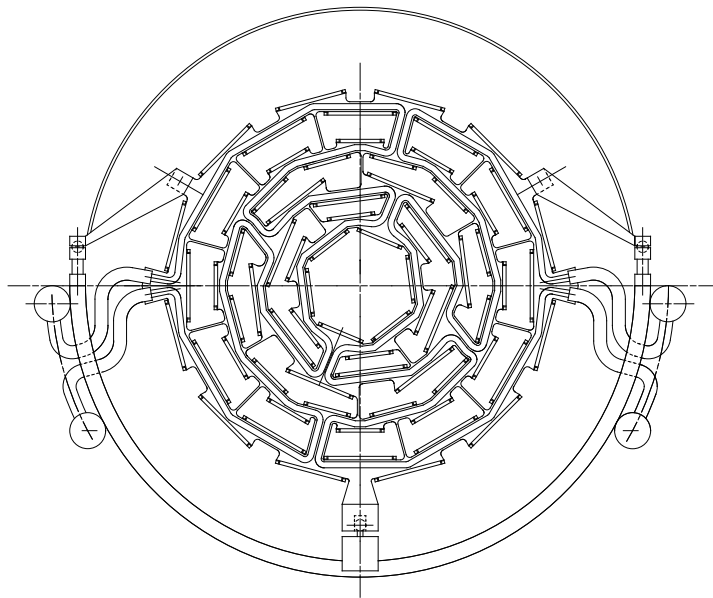


Figure 3.4: The layout of a silicon microstrip detector's barrel as a slice orthogonal to the beam direction.

sensors. They cover the full ϕ range due to the overlaps; their inner radius is 2.57 cm, the outer one is 9.96 cm. The F-disks cover a rapidity region $-1.5 < \eta < 1.5$. The H-disks are located further away from the nominal interaction point, extending the tracker's coverage to $-3 < \eta < 3$; their hit information is not taken into account by the tracking algorithm used for this analysis.

Most F-disk modules contain a pair of sensors glued back-to-back that are relatively tilted by 2° stereo angle, allowing some position measurement in the radial direction. The position in z of the wafers yields a position measurement along z .

The SMT's large coverage combined with the closeness of the first barrel layer to the interaction point allows for an excellent capability to reconstruct secondary vertices e.g. from decays of b-hadrons, as will be shown in Section 4.3.

3.3.3 Radiation Protection System

The radiation level, especially for the inner modules of the silicon microstrip detector, is high enough to deteriorate the quality of the silicon detector modules over time. There are two main radiation-dependent effects, increasing leakage currents and change of depletion voltage. Higher leakage currents cause an increasing signal noise, while an increase in depletion voltage may cause electrical break-down at some point. Radiation damage can also occur by the beam not being focused or centered; this can especially happen when a new batch of protons and antiprotons are injected into the Tevatron, and when the beam is conditioned for collisions. The DØ detector has not acquired a higher radiation dose than was optimistically expected. No silicon detector malfunction has been ascribed to radiation effects. The effects from regular, non-accidental radiation have been studied before the detector was assembled. Severe negative effects were not expected to occur below an integrated luminosity of 5 fb^{-1} . This has been confirmed: no problematic radiation effects have been observed for the data taking period of this analysis [50]. The exposure to the total luminosity of 10 fb^{-1} [21] has led to a foreseen reduction in hit efficiency in the inner barrel layer, but to no problems in the rest of the SMT. In 2006 an additional radiation hard inner detector layer has been introduced at a very small distance from the beam. A prerequisite for this new layer was a new beam pipe with a smaller diameter in the collision region which was installed simultaneously. This analysis does not include data taken with this new SMT layer. For the data used in this analysis the original inner SMT layer was fully efficient.

The radiation level and the integrated dose are monitored constantly by two systems, the beam loss monitors and the radiation monitors. Both alarm systems have been successfully protecting DØ's SMT from fatal radiation deposits.

Beam Loss Monitors

These monitors consist of an array of (non-proportional and thus fast) argon gas counters called Beam Loss Monitors (BLMs). They have a direct connection to the Tevatron controls to be able to trigger a Tevatron beam abort. The beam loss monitors were already used by CDF and the Tevatron Beams Division during Run I, and are known to be stable and reliable. The beam loss monitor tubes have an active volume of about 100 cm^3 of argon at 0.97 bar surrounded by two cylindrical, concentric nickel electrodes. The inner electrode is charged to 2000 V. The outer electrode is held at ground potential and is surrounded by a glass envelope.

Eight of these tubes are deployed at DØ. They are located just outside each of the two end caps, parallel to the beam pipe. Their center is at a distance of 12.2 cm from the beam axis, which allows them to be inside the shielding, and about 4 m away from the interaction point in the beam direction.

The BLMs are read out and powered by a chassis located in the DØ counting room. Two separate high-voltages are run to the detector. Each 4-tuple of the BLM tubes (on each side of the detector) shares one HV supply by connecting them in parallel. The CAMAC log integrator electronics convert the wide dynamic signal range to a voltage proportional to the logarithm of the signal: $V_{\text{out}} = V_{\text{slope}} \log((I_{\text{in}} + I_{\text{bias}})/I_{\text{ref}})$ with $V_{\text{slope}} = 10\text{ V}/4\text{ decades}$, in current $I_{\text{bias}} = 1.6\text{ nA}$, $I_{\text{ref}} = 1.0\text{ nA}$, and $I_{\text{in}} = Q/\tau$ with the collected charge Q and a time constant of $\tau = 0.94\text{ s}$.

The Tevatron's control system Acnet is used to process, archive, and access both instantaneous and integrated signal readings. The interface from the BLM read-out and the Beams Division system is located in a dedicated Beams Division rack in the DØ control room. The instantaneous reading is used to trigger the beam dump by cutting the voltage of the beam permit wire that runs from the DØ control room to the Tevatron main control room. Dropping the beam permit activates fast magnet kickers that steer the beam out of the machine in one turn. An alarm sounds in the DØ control room whenever the abort system is triggered. This kind of beam aborts is handled by the operators of the DØ and the Tevatron main control room according to a defined protocol.

There are distinct allowed levels for the different states of the Tevatron. Automatic aborts are issued if the BLM reading exceeds 10 rad/s during setting up the beams and 2 rad/s during stable colliding beams. Warnings are issued in the control room at lower instantaneous readings. A detailed description of the BLM system is available in [13].

The integrated dose measured by the BLMs gives an estimate of the radiation seen by the silicon tracker system. Due to the non-linear signal shaping and pile-up of the instantaneous reading, the integration is not straight-forward; it can only be measured with a large systematic error. To allow for a cross-check, thermoluminescent dosimeters were deployed very close to the beam pipe right outside the end caps and around the BLMs. Their dose measurements are used to cross-check the archived BLM readings, and to determine the total dose seen by the silicon tracking detector independently. Their readings confirm those of the BLM system.

Radiation Monitors

The fine-grained online radiation monitoring system gives a readout proportional to the particle flux at the SMT using silicon test diodes from SMT production wafers. Two of these diodes together with pre-amplifiers are mounted on a *finger*; 24 diodes are deployed close to the silicon tracking system, on an F- and an H-disk on both sides of the center of the SMT detector. This positioning covers the full r and ϕ range of the SMT.

The diodes are read out with two different amplifications such that valid readings both for a low dose integration and a high dose alarm can be obtained. Short integration times of the accumulated current allow for a time resolution of $O(1\text{ ms})$ even for high instantaneous losses.

The diodes are depleted with a reverse voltage bias. Ionizing particles passing through the diode create an electron-hole pair the charge of which is collected on opposite sides of the diode. The height of the signal is proportional to the total charge deposited. The signal's combined rise and fall time is less than 100 ns. The diodes are selected to have a high breakdown voltage of $V_b > 400\text{ V}$, reducing their sensitivity to radiation damage which lowers the breakdown voltage. This allowed their proper functioning during the full lifetime of the SMT.

The fingers are read out by an amplifier and a shaper in a custom electronics module in a standard VME crate. The same crate contains a module that supplies low voltage to the front-end electronics and bias voltages to the diodes. The shaped signal is fed

into an ADC module that is read out by a PowerPC module. The real-time PowerPC module provides access to the reading via a 1553 bus, which connects the radiation monitoring system with the DØ online GNU/Linux cluster. Certain combinations of fingers with high radiation trigger the readout of a buffer that holds the traces of the radiation monitor readings for close inspection afterwards. Otherwise integral dose values per minute are recorded.

The GNU/Linux cluster is used for DAQ access to the radiation monitor readings, archiving of the monitoring data, and access by a graphical user interface (GUI) to the readings. The data is held for seven to fourteen days on the cluster; older data is archived and available through the DØ mass storage system SAM. The GUI allows straightforward reading of the integrated and instantaneous radiation doses as measured by the radiation monitors; excesses above preset thresholds are clearly visible.

A detailed description of the system together with results of the first years of operation can be found in [12, 40, 46].

3.3.4 Central Fiber Tracker

The second part of the central tracking system is built from scintillating fibers. Clear fiber waveguides carry their scintillation light to Visible Light Photon Counters (VLPCs) for readout. The central fiber tracker (CFT) surrounds the SMT with eight cylinders at radii of 19.5 cm, 23.4 cm, 28.1 cm, 32.8 cm, 37.5 cm, 42.1 cm, 48.8 cm, and 51.5 cm. The two innermost cylinders are 166 cm long, the others are 252 cm long, covering a rapidity region $|\eta| < 2$. The 76,800 channels of the central fiber tracker are divided into 80 sectors in ϕ with 960 fibers each.

Each cylinder consists of a pair of fiber layers parallel to the beam and a pair of layers tilted by $+3^\circ$ (-3°) for even (odd) cylinders. This stereo angle helps to identify the hit position along a fiber by matching clusters of different stereo angles, just like for the SMT modules.

The second layer of a pair is shifted by half a fiber diameter (i.e. $835\text{ }\mu\text{m}/2$) and sandwiched with the first layer, allowing for a 99% efficiency in the fiducial region for at least one of the layer pairs to produce a hit. The light of the scintillating fibers is transported to visible light photon counters using clear fibers [80]. The VLPCs are located close to the detector, and to allow low noise and high single photon efficiency they are operated at a temperature of about 9 K. This highly sensitive system is needed,

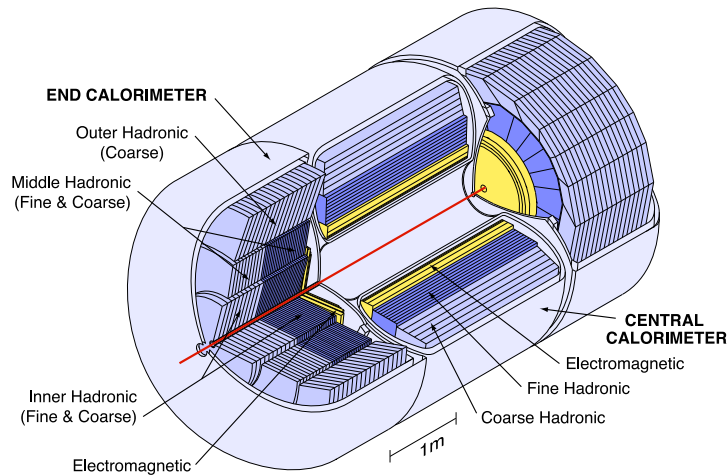


Figure 3.5: The DØ calorimeter detectors.

as in average only 10 photons are detected from a minimum ionizing particle crossing a fiber.

3.4 Calorimetry

While tracking detects the paths of charged particles, DØ's calorimeter encloses the interaction to measure the energy distribution of both neutral and charged particles. It is constructed as a combination of different, specialized subdetectors: the preshower detector can help localize electrons in a thin layer in front of the main calorimeter, the electromagnetic calorimeter has a higher resolution and lower interaction length but higher radiation length than the hadronic calorimeter. This makes the electromagnetic subdetector more sensitive to photons and electrons, whereas the hadronic subdetector is suitable to fully contain the energy of hadrons.

The calorimeter hardware is unchanged since Run I — only the read-out electronics have been updated to support the higher read-out frequency of Run II. A sketch of the calorimetry detectors is shown in Fig. 3.5.

3.4.1 Preshower Detectors

The preshower detectors are thin layers just outside the solenoid which accounts for $1.1 X_0$ radiation lengths. They serve as a tracking and calorimetry device, measuring the position and width of the early particle showers and a small fraction of their energy

deposit. They can improve the matches between tracks and calorimeter showers and thus the resolution of the electromagnetic energy measurement. The preshower detector can also help in distinguishing electrons from pions: showers inside the preshower detector are more likely generated by electrons than by pions [8].

There are two different kinds of preshower detectors, a central (CPS) and a forward (FPS) one. Their scintillator signals are guided through wavelength shifting fibers to the same kind of VLPCs as for the CFT. The CPS's three layers of scintillators cover the region $|\eta| < 1.2$. They are mounted at a radius of 72 cm, with a $0.9 X_0$ radiation lengths lead absorber in front, adding to the $1.1 X_0$ radiation lengths of the superconducting coil.

The four layers of the FPS scintillators are mounted at the inner face of the end calorimeter cryostats, covering $1.4 < |\eta| < 2.5$. The two pairs of scintillator layers are separated by a $2 X_0$ absorber made of lead and stainless steel. The jet reconstruction software used in the analysis did not take the preshower data into account.

3.4.2 Calorimeter

During Run I, DØ's full-coverage calorimeter showed an excellent performance. It was thus kept for Run II; only the read-out electronics were changed to account for the higher bunch crossing frequency. The signal shaping time was reduced (compared to Run I) to 200 ns, compatible with the charge drift time and the 396 ns bunch crossing period.

The different calorimeter systems are divided into three η -regions (one at $|\eta| < 0.8$ and two at $0.8 < |\eta| \lesssim 4$) and contained in separate cryostats, which allows access to the central tracking system by moving the forward cryostats aside. The energy of particles that interact primarily through the electromagnetic interaction (electrons and photons) is measured by the inner, electromagnetic part of the calorimeter. It is contained in a fine hadronic calorimeter, which in turn is contained in a coarse hadronic calorimeter, with decreasing depth resolution.

The calorimeter needs to have a large depth in radiation and interaction length, to contain the full energy of the particles. As most heavy absorbers cannot be used to determine the energy deposit, the calorimeter consists of alternating absorber and detection materials. The absorber is uranium, copper, or stainless steel; the detection material is liquid argon.

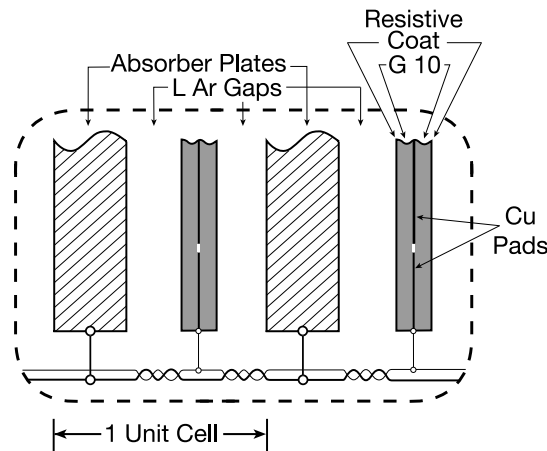


Figure 3.6: The layout of a typical calorimeter cell.

The calorimeter consists of cells with absorber plates of different thickness in different regions of the calorimeter, 2.3 mm liquid argon, and signal boards, followed again by 2.3 mm liquid argon and the next absorber, argon, board, argon combination. The signal boards consist of a copper pad, on which the signal is capacitively induced. The pads are surrounded by insulator plates, which are coated with resistive epoxy. The layout is depicted in Fig. 3.6.

The absorbers are electrically grounded, whereas the epoxy is charged to 2.0 kV, providing a drift field for ionization across the gap. The insulator plates decouple the high voltage from the readout pads and their pre-amplifiers. The 2.0 kV field is strong enough for a charge collection time of ≈ 450 ns [68].

Electromagnetic Calorimeter

The inner part of the calorimeter is highly sensitive to charged particles. It uses uranium absorbers that are 3 mm thick in the central and 4 mm thick in the forward region. It accounts for a total radiation length of $20 X_0$. At the depth of the highest average energy deposit, the electromagnetic calorimeter has a segmentation of $d\phi \times d\eta = 0.05 \times 0.05$ to increase the positional and thus directional resolution of electromagnetic showers. The readout segmentation of the other depth sections of the electromagnetic and hadronic calorimeter is $d\phi \times d\eta = 0.1 \times 0.1$. The segmentation is shown in Fig. 3.7.

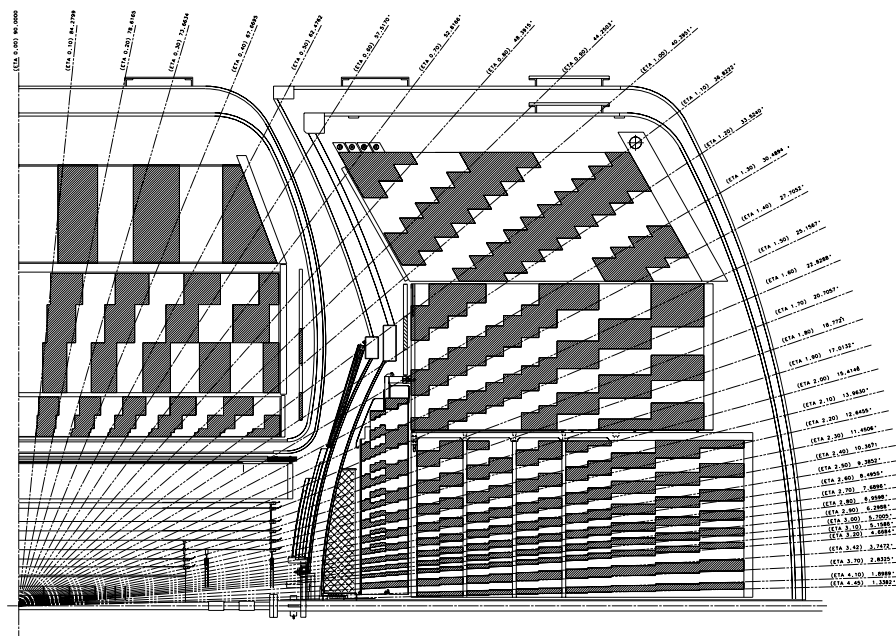


Figure 3.7: Projection of a quarter of the DØ detector, showing the calorimeter longitudinal and lateral segmentation. Each rectangle of the checkerboard pattern denotes a calorimeter cell.

Hadronic Calorimeter

The hadronic calorimeter's task is the energy measurement of hadrons. To stop even high-energy hadrons, it has approximately $6 \lambda_I$ interaction lengths in the central and $9 \lambda_I$ in the forward region. It is split into a fine part, containing 6 mm thick absorbers of an uranium-niobium alloy, and a coarse part, with absorbers that are 46.5 mm thick. The latter ones are made of copper in the central region and steel in the forward region.

Inter-Cryostat Detector

In the region $0.7 < |\eta| < 1.4$, the overlap region between the central and the forward cryostat, the coverage of the calorimeter is reduced due to high amounts of uninstrumented material, reducing the main calorimeter's resolution. To compensate for this gap, the inner cryostat detector (ICD) provides a measurement between the cryostat walls used to correct the main calorimeter's data.

The ICD consists of a single layer of 384 scintillator tiles with dimensions (0.1×0.1) in $(\eta \times \phi)$, matching the main calorimeter's cells. The scintillators' light signals are converted by wavelength shifting fibers outside the ICD, and then transported by clear fibers to VLPCs.

Similar to the ICD, thin cells called Massless Gaps are installed just inside the central and forward cryostats. The cells are almost identical to the main calorimeter's cells; unlike the main calorimeter's cells they do not have thin ground plate absorbers. The forward and central calorimeters, the Massless Gaps, and the ICD combined allow an almost hermetic coverage of the DØ calorimetry up to very large pseudo rapidity.

3.5 Muon System

The muon system is the outermost detector system of the DØ detector. It covers the toroid magnet from both the in- and outside. The magnet bends the muons to allow a measurement of their momenta. The momentum measured by the muon system differs from that at the vertex due to energy loss from traversing notably the calorimeter material. For high momentum muons the momentum measurement in the muon system is more precise than that of the central tracking system inside the solenoid. The muon system is divided in a central part at $|\eta| \lesssim 1$, and two forward parts at $1 < |\eta| < 2$. Each

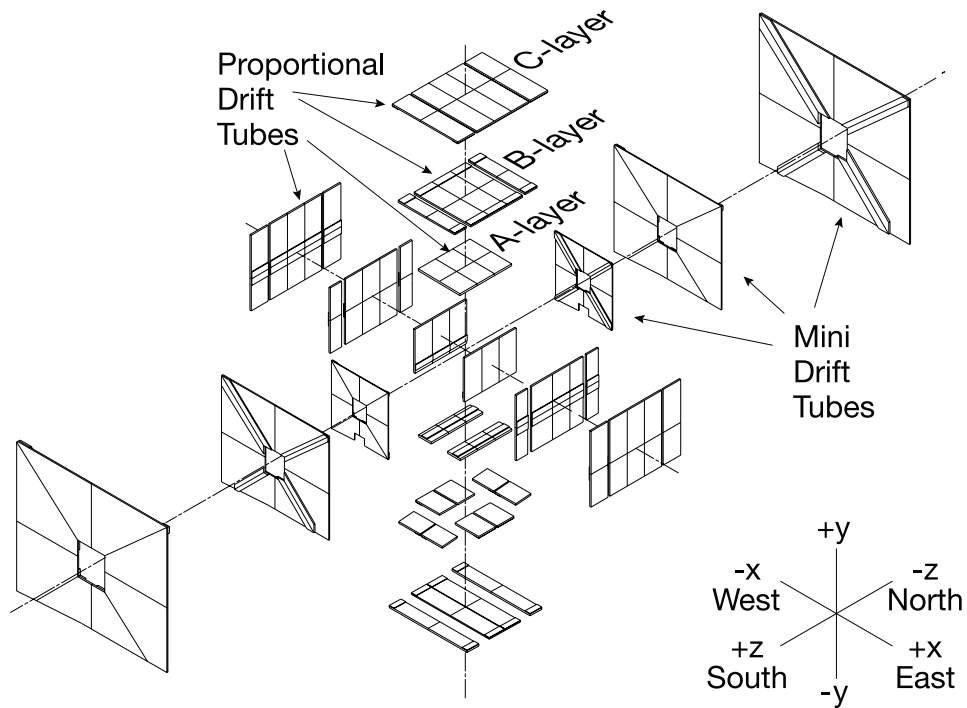


Figure 3.8: Schematic view of the muon detector's drift tubes.

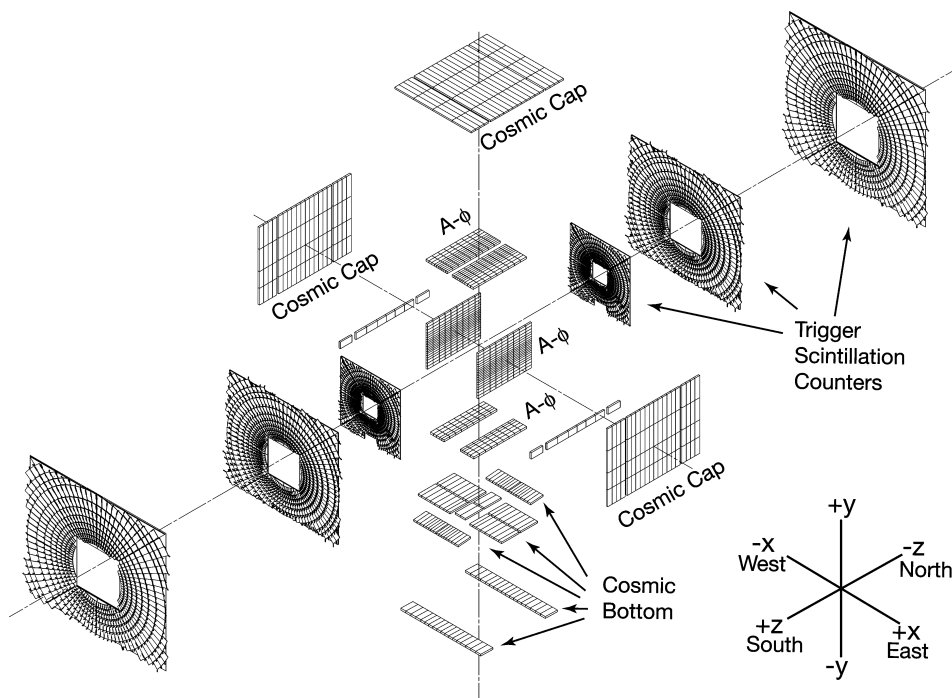


Figure 3.9: Schematic view of the muon detector's scintillators.

of them has three layers of drift tubes, where the one closest to the interaction point (the A layer) is just inside the toroid, while the B and C layers are outside the toroid, see Fig. 3.8. Several layers of scintillators give trigger and additional timing information, as shown in Fig. 3.9. A detailed description of the muon system can be found in [2].

3.5.1 Toroid Magnet

The toroid was already used in Run I. It is run at 1500 A; its magnetic field reaches a maximum of 1.8 T in some locations. The magnetic field lines in the region surrounded by the toroid at $x = 0$ are shown in Fig. 3.10. The field lines inside the toroid itself are perpendicular to the field of view in this figure (i.e. along the x-axis) in the top and bottom parts, and along the y-axis in the left and right parts. Muons are thus bent in the $r - z$ plane. The offset from a straight line produced by the bend is measured by the drift chambers.

3.5.2 Proportional Drift Tubes

Three layers of drift tubes cover the toroid magnet; two (layer B and C) are outside, layer A is inside the magnet. The central muon detector uses proportional drift tubes (PDTs), while the forward one uses Iarocci-type mini drift tubes (MDTs) [14].

Central Muon Detector

About 55% of the central detector region is covered by three layers of PDT drift chambers; 90% of the detector is covered by at least two layers. The incomplete coverage is mainly caused by detector and trigger electronics that need to be close to the detector: they are grouped below the detector, leaving no space for full muon chamber coverage and creating the so called *bottom hole* for the muon system.

The typical drift chamber size is $250\text{ cm} \times 550\text{ cm}$. The cells are made of extruded aluminum tubes of 10.1 cm width and 5.0 cm height. Typically, 24 tubes form one chamber. The chambers of most of the A layer have four decks of cells; the B and C layer and the bottom part of the A layer have three decks.

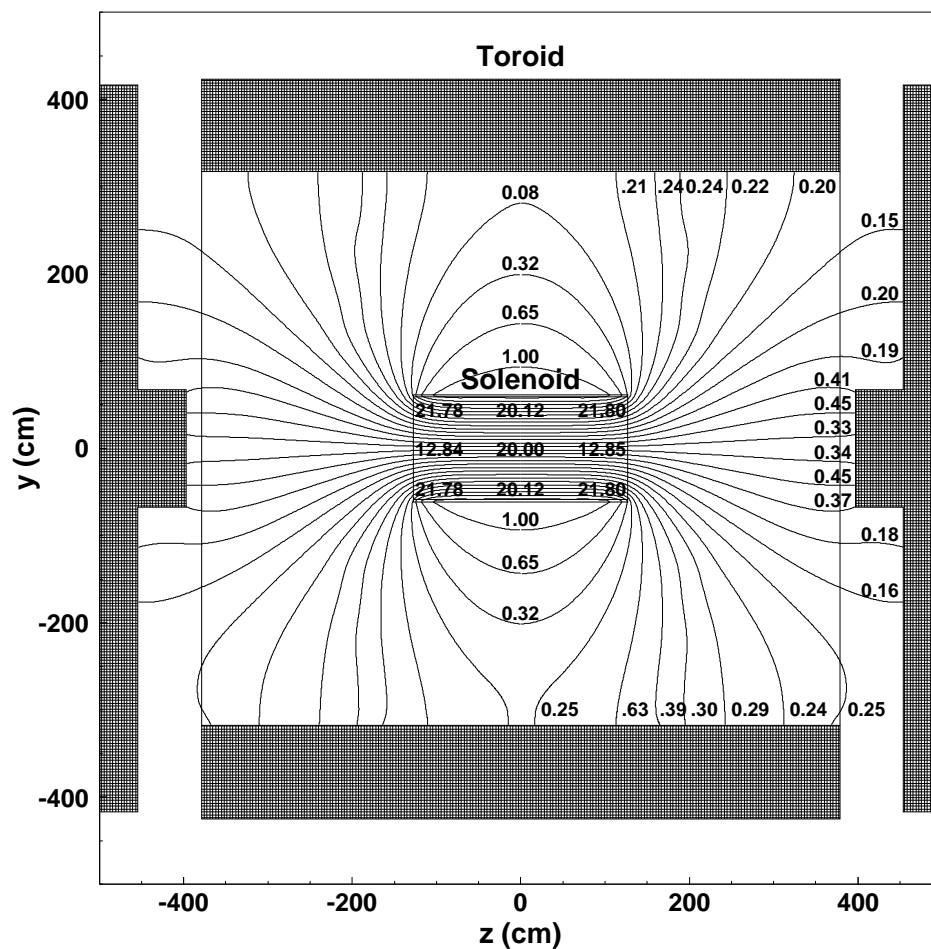


Figure 3.10: The toroid and solenoid magnetic field lines in the inner detector and calorimeter region at $x = 0$. The field strength is given in kGauss. Field lines inside the toroid are perpendicular to this plane for the top and bottom parts, and along the y -axis for the left and right parts.

Each cell has an anode wire in the center that runs along the tube; every two neighboring cells have their anode wire connected at the far end, as seen from the readout electronics. The wires are oriented along the toroid's field lines.

When a particle ionizes the gas mixture of 80% argon, 10% methane, and 10% CF₄, the charges are collected by an anode wire and pads at the long sides of the cell. The gas mixture and the operating voltages of 5 kV for the anode and 2.5 kV for the pads allow for a fast drift velocity of $\approx 10 \text{ cm}/\mu\text{s}$, yielding a maximum drift time of about 500 ns.

The charge is read out with a time stamp at both ends of the wires. The location of the hit along the wire is calculated from the difference of the time stamps: the smaller the difference, the closer the hit is to the end where the two cells' anode wires are connected. This allows a resolution of 10 to 50 cm, depending on the distance of the hit to the readout electronics.

To increase the precision of the position determination the pads employ a vernier mechanism: they are built from two insulated conducting bands, an inner and an outer one. The charge is deposited partly on the inner and partly on the outer plate. Their common contact has a zigzag shape. The measured ratio of the inner and outer band's signal yields an additional position information, with a precision of up to 3 mm modulo 610 mm, the repeat period of the vernier pads' zigzag pattern.

The total positional resolution can be translated into an expected muon momentum resolution of $\sigma(1/p) = 0.18(p - 2)/p^2 \oplus 0.005$ (with p in GeV/ c). The first term is a result of the muons' multiple scattering in the toroid iron, the second, constant in p , is due to spatial resolution and alignment errors. The resolutions determined from data show that the momentum dependent part is underestimated by approximately 10% [38]. The efficiency is approximately 95% for each layer at $10 \cdot 10^{30} \text{ cm}^{-2} \text{ s}^{-1}$, with a 1% decrease for each five-fold increase of the instantaneous luminosity up to $50 \cdot 10^{30} \text{ cm}^{-2} \text{ s}^{-1}$, as shown in [42].

Forward Muon Detector

The forward muon system was upgraded from Run I and consists of Iarocci mini drift tubes (MDTs). The A layer consists of four decks of muon chambers, while the B and C layers each have three — just as for the central system. The cells are extruded aluminum tubes, sized $9.4 \text{ mm} \times 9.4 \text{ mm}$. They are aligned with the forward toroid's magnetic field lines to have the muon bending perpendicular to the wire direction.

The MDTs' drift time is ≈ 60 ns; the positional resolution is ≈ 700 μ m. Due to shielding walls and dead zones at the ends of the MDTs, the overall reconstruction efficiency of the MDTs is approximately 90%.

3.5.3 Scintillator Counters

The scintillator counters are used for triggering and time stamping muon signals with a precision of 2.5 ns. This precise timing allows to determine the bunch crossing a muon stems from, and it improves the positional measurement of the PDTs by allowing a precise estimate for the drift time correction. It is also used to veto cosmic muons, i.e. muons that are not the result of the $p\bar{p}$ -collision but are decay products of cosmic ray showers.

In the central region of the DØ detector, at $|\eta| < 1$, the toroid is covered by one scintillator layer from the inside called *A - ϕ* , and one from the outside called *Cosmic Cap*. In the forward region, at $1 < |\eta| < 2$, one layer is inside the toroid and two layers are outside. The scintillator signals are transmitted via wavelength shifting fibers to photomultipliers contained in light-tight, magnetic field shielded boxes.

3.6 Luminosity System

The instantaneous luminosity can be measured [34, 75] with the interaction rate of a known process

$$\mathcal{L} = -\frac{f_x}{\sigma} \ln(1 - P) \quad (3.1)$$

with σ the cross section of the process and P the probability of having at least one interaction of that process per bunch crossing. The bunch crossing frequency is $f_x = 2.5$ MHz. It can be also calculated from the properties of the beams as:

$$\mathcal{L} = \frac{f_R B N_p N_{\bar{p}}}{2\pi (\sigma_p^2 + \sigma_{\bar{p}}^2)} F(\sigma_l/\beta^*) \quad (3.2)$$

where $f_R = 47,713$ kHz is the revolution frequency of the beams inside the machine, $B = 36$ is the number of bunches in each beam, N_p ($N_{\bar{p}}$) is the number of (anti-)protons in each bunch, σ_p ($\sigma_{\bar{p}}$) is the RMS transverse size of the (anti-)proton beam at the

interaction point, and F is a form factor that depends on the ratio of the bunch length σ_l to the β -function at the interaction point, β^* . The factors $f_R BN_p$ and $f_R BN_{\bar{p}}$ can be measured as they correspond to the beams' currents. Whereas Equation 3.1 can be used to experimentally determine the luminosity (see later in this section), Equation 3.2 is useful to compare luminosities and to study the instantaneous luminosity's dependencies for instance on the beam geometry.

At DØ, the luminosity is monitored by measuring the rate of non-diffractive, inelastic $p\bar{p}$ collisions in the interaction region. The rate is determined by scintillators surrounding the beam pipe at a distance of $z = \pm 135$ cm from the nominal interaction point. They cover the pseudorapidity range $2.7 < |\eta| < 4.4$.

The luminosity detectors measure the fraction of beam crossings that generate no signal, i.e. that caused no non-diffractive, inelastic collision. Using Poisson statistics, the average number of interactions per crossing is calculated. The measured rate can then be converted into instantaneous luminosity (see [22]) using the known cross section for this process of (60.7 ± 2.4) mb (see [53]) and the detector efficiency and acceptance. The product of efficiency and acceptance has been determined as $(75.8 \pm 3.8)\%$ from Monte Carlo simulations.

The luminosity is calculated and stored for a range of events called luminosity blocks, referred to by their Luminosity Block Number (LBN). Each data-taking run consists of at least one LBN and each LBN can only be part of one run. Grouping events into sub-run blocks allows to take into account changes in instantaneous luminosity during a run; usually, instantaneous luminosity decreases due to beam losses and reduced beam focus resulting in a larger beam width.

The luminosity measurement has an uncertainty of 6.1 % [48]. The main contributions are the uncertainty of the non-diffractive, inelastic cross section and the detector efficiency and acceptance.

3.7 Data Acquisition and Trigger

DØ was upgraded for Run II to be able to take data with the design luminosity of $\mathcal{L} = 2 \times 10^{32} \text{ cm}^{-2}\text{s}^{-1}$, with a bunch crossing frequency of 2.5 MHz. Each bunch crossing yields an average of $\langle n \rangle = 3.9$ events; only about 2 % of all crossings do not produce

a collision. The event rate that the detector readout system has to withstand is thus almost identical to the 2.5 MHz bunch crossing rate.

The rate of events produced is too high for storing them all. Most of these events are “soft QCD” events that are of limited interest for most physics analysis anyway. An obvious solution to the event rate reduction is thus to select only events that are interesting for physics analyses, for instance events with high-momentum jets or jets that are relevant for studying the physics of b-quarks. Any such rate reduction requires to compromise between physics relevance and event bandwidth.

For DØ, this selection was done using a three stage trigger system: the first level trigger (L1) is designed to reduce the event rate to 10 kHz, the second level (L2) to 1 kHz, and L3 to around 50 Hz. The remaining events are sent to tape for permanent storage. They are then processed (“reconstructed”) to find physics objects in the event. The actual maximum event rates changed considerably during the data taking period used in this analysis, increasing over time in an effort to reach the design rates. The reduced rates during the first years were mostly due to limitations in the electronics’ performance.

Each trigger system has a limited time to determine the properties of the event. The L1 trigger must provide a trigger decision at the bunch crossing rate, 396 ns. To have more time for the decision making process, the detector data is buffered in pipeline analog memory for 25 consecutive beam crossings. However, this was designed for a bunch crossing rate of 132 ns, hence there is a fixed total latency of $3.30\,\mu\text{s}$ for each decision. Since there is always an L1 decision at the end of the pipeline, the L1 trigger process itself does not generate dead-time. For L2 and L3, the incoming event rate combined with the size of the random access buffer limit the time that trigger algorithms are allowed to work on the event. By also pipelining these trigger levels, the processing time can be much longer than the decision repetition rate, but filling up the buffers introduces dead-time at L2 and L3.

If a trigger, i.e. its combination of L1, L2 and L3 selections is firing at a rate that is too high, it can be *pre-scaled*. A pre-scale of 10^6 means that, on average, only 1 out of every 10^6 triggered events is accepted. This is implemented by randomly ignoring events that pass the pre-scaled trigger at level 1. The randomness ensures that there is no correlation between the pre-scale vetoes of different triggers.

3.7.1 First Level Trigger System

The first level trigger expects its inputs from the sub-detectors (so called input *And/Or terms*) to be available 3.30 μs after the beam crossing. The detector readout crates allow for data of 32 crossings to be pipelined before they must be moved out or discarded. Hence, 7 times 132 ns (924 ns) is available for the central trigger and its distribution to the components.

There are 256 input And/Or term bits in total, representing coarse measurements (both with respect to the uncertainty of the energy measurement and the localization of the detector response) from the calorimeter, the muon system (drift tubes and scintillators), the preshower detectors and the central fiber tracker.

Each of these input elements can set a number of output bits corresponding to a sub-trigger decision. The trigger decision of L1 is a boolean combination of these terms; it typically requires a coincidence (“AND”) of two or more terms. The L1 framework supports 128 trigger decision bits, each representing a combination of the And/Or terms. A number of field programmable gate arrays is used to combine the L1 trigger terms and the luminosity readout, and to determine the final trigger bits. The trigger result is the logical “OR” of its output trigger bits, taking into account the pre-scaling of a number of these bits. The trigger provides the result of its decision within 164 ns [9].

If the L1 trigger lets the event pass, the readout data is digitized and moved to the random access memory buffer, waiting for the L2 decision.

First Level Calorimeter Trigger

Two types of calorimeter triggers exist: one using data from the electromagnetic part of the calorimeter to trigger on e.g. photons and electrons, the other using the full depth of the calorimeter to trigger on jets. The latter, used in this analysis, uses a schema $\text{CJT}(n, e)$, requiring n calorimeter towers of energy $\geq e \text{ GeV}$. The size of each tower is 0.2×0.2 in $\eta \times \phi$, covering a range up to $\eta < 2.4$. They consist of radially aligned sets of calorimeter cells extending over the full depth of the calorimeter, as shown in Fig. 3.7. The trigger term $\text{CJT}(1, 5)$ used in this analysis requires at least one tower with a signal corresponding to an energy deposited of at least 5 GeV. The towers’ energy is uncorrected for any jet energy effects, reducing the efficiency of this trigger for jets with

transverse energies even up to $E_T = 20$ GeV as shown in Section 4.2.1. Nevertheless, this trigger term triggers at a very high rate, which often requires pre-scaling.

First Level Muon Trigger

The muon trigger depends on the readout of the muon scintillators and wire hits. Signals from the muon scintillators need to pass timing cuts with respect to the beam crossing time. The purity of this trigger is rather low, especially in the vicinity of jets. It, too, fires at rather high rates, which often causes triggers based on this L1 trigger term to be pre-scaled.

3.7.2 Second Level Trigger System

The second level trigger algorithms use the L1 information and a subset of the digital detector readout as inputs. The algorithms are divided into two classes: those that run on L2 preprocessors and those that run on L2 global processors. The former create physics objects from the input, e.g. jets from calorimeter towers; they only access one sub-detector per algorithm. The global processors on the other hand can combine all preprocessor results, even across detector parts. This allows e.g. to create L2 muon candidates that are matched to a central track.

The L1 trigger bits determine which global scripts will be run; the global scripts determine which L2 preprocessors need to be run to generate the global scripts' input. The full digitized readout data is made available to L3 if a L2 trigger term selects an event.

3.7.3 Third Level Trigger System

Only the third level trigger has access to the full detector readout. Its filter software runs on a cluster of standard PCs with many events being processed in parallel. L2 trigger decisions are signaled to the Event Builder, which in turn collects the detector readout and trigger output (“builds” the event) and makes it available to a free cluster node of the L3 trigger.

L3 trigger scripts depend on L2 trigger bits; they are only run if the L2 trigger bits have selected the event for the specific script. These scripts contain at least one filter;

each filter either combines the results of filters logically or compares values calculated from physics objects to predefined thresholds, e.g. $p_T > 5 \text{ GeV}$ for a track. There is not enough time for L3 to perform a full event reconstruction using the offline software. Instead, it reconstructs physics objects with fast algorithms with lower precision and efficiency, sufficient for the needs of a trigger to select events based on correlations (missing E_T or maximum distance of two objects). If a script finds all its filters to be satisfied it will set its trigger bit.

3.7.4 Online Event Selection

The set of active triggers is defined by a trigger list. Each run period has a given trigger list version, with a defined version of trigger algorithms. Each trigger list comes with its set of pre-scale numbers, for several ranges of instantaneous luminosities. These pre-scales keep the data acquisition rate in a range that maximizes the utilization of the available bandwidth without exceeding it.

Events that pass a trigger are sent to the tape system for permanent storage and offline analysis. They can be accessed through a distributed mass storage and file cataloging system called SAM [69].

3.8 Monte Carlo Event Modeling

Some of the efficiencies used in this analysis were determined with the help of simulated data. This event simulation consists of generating events, usually specifying a range of physics processes to study. These events describe particle types and their momentum.

The detector does not measure these initial particles, but energy deposits from a combination of the behavior of initial particles and their decay products. The interaction of particles with the detector (both its active, measuring part and its passive part) is the second stage; this also includes the decay of relatively long lived particles. The final stage is the simulation of the detector response to the particles' energy deposits. Reconstruction of physics objects from the detector readout is done with the same software for simulated and for real data.

3.8.1 Pythia

The Monte Carlo Events used in this analysis have been generated using Pythia [77] version 6.202 with CTEQ5L for the parton distribution functions. The b-jet samples have been generated as inclusive QCD events (MSEL=1 for Pythia), selecting those events that contain at least one b-quark.

To be useful for this analysis, the simulated events have to cover a wide range of the interaction's p_T (called \hat{p}_T for Pythia). Due to QCD's sharp reduction in cross section for higher p_T , almost all events are generated with very low p_T . To increase the statistical resolution in the high invariant p_T tails of the distribution, several samples with different \hat{p}_T have been combined, adjusting their respective event weights to avoid double-counting. In total, 1,800,000 simulated events were used for simulating b decays.

Simulated $Z \rightarrow b\bar{b}$ events were used to determine the efficiency of the analysis' cuts. In total, 800,000 events have been generated with an invariant mass of the initial partons between 60 GeV and 120 GeV. The generator was set to produce g/Z events (MSEL=11, MSTP(43)=3), the decay was selected to be $b\bar{b}$.

For all events, impact parameters have been generated using a double Gaussian matter distribution (MSTP(82)=4), and the turn-off was smoothed below $p_T = 2.4$ GeV (PARP(82)).

3.8.2 Simulation of the Detector Response

The detector's response to the particles' energy deposits has been simulated with the GEANT3 [59] based software `d0gstar` for the geometry and the particles' passage and interaction with the detector. The response of the detector's electronics has been simulated with `d0sim` [55]. The versions of these software packages were defined by the reconstruction software version p14 (p14.05 and higher) used in this analysis.

3.9 Event Reconstruction

Events from Monte Carlo simulation as well as data events were processed by the same software to identify physics objects, and to apply offline corrections to measurements, e.g. for alignment, timing, and energy. The data was reconstructed with the “pass2 tmb-

fixed p14” version of DØ’s reconstruction program **d0reco**. This corresponds to version p14 (p14.05 and higher) of **d0reco**, with additional improvements (“fixes”) applied to the analysis data format (TMBfixer) during reprocessing. They applied improved τ identification for pass 1 and optimized clustering algorithm (T42 in killing mode) and calorimeter cell noise suppression for pass 2 [83].

Chapter 4

Data Selection

The events used for this analysis have to pass a chain of selection criteria, from the trigger during data taking to the event selection within the final analysis. The efficiency of these selection steps for the $Z \rightarrow b\bar{b}$ process must be known to be able to calculate a cross section times branching ratio from a number of events passing these cuts.

This analysis uses two distinct di-jet samples where both jets are within $|\eta| < 1.2$ and have a transverse energy of $E_T > 15$ GeV. One sample consists mostly of jets from light (u, d, s and c) quark partons and gluons, from here on called “light jet sample”. The other sample has an enhanced fraction of b-jets, from here on called “b-jet sample”.

Both jets of the light jet sample must be anti-tagged with the *Jet Lifetime Probability* (JLIP) tag, see Section 4.3.3. The light jet sample is required to have *exactly one* jet with at least one associated muon, where a muon is associated only to the closest jet within $\Delta R = \sqrt{\Delta\eta^2 + \Delta\phi^2} < 0.5$. The b-jet sample requires that *both* jets have at least one muon associated, see Section 4.4.1.

The efficiency of the jet acceptance cuts is not corrected for in the data, but is also applied to the Monte Carlo simulation as an overall scaling. Other selection efficiencies are calculated separately for the two data samples and, except for the jet acceptance cuts, an event weighting procedure using the inverse of the efficiency is applied.

4.1 Efficiency Correction

A common approach is to determine the overall analysis efficiency for the signal events by applying trigger simulation, reconstruction and analysis algorithms to a Monte Carlo

sample. Only some of the Monte Carlo sample's events will pass the trigger simulation, reconstruction and selection criteria; the ratio of events passing over the number of original events allows to calculate the overall efficiency. It is extremely difficult to simulate data events such that the efficiencies for all stages can be properly evaluated; e.g. the calorimeter's response to jets in real data is extremely complex and is hard to simulate.

To reduce the effect of this problem, efficiencies are often determined on data. Usually, Monte Carlo simulation is then used to calculate the overall (trigger, reconstruction and offline selection) efficiency for the signal events, by probing the signal events' phase space. Additional correction factors must usually be applied to simulated events to get the proper behavior as seen in the data (e.g. Monte Carlo-specific jet energy scale factors). These corrections can only be determined by comparing the predictions from Monte Carlo samples to measurements from data. Strictly speaking they can only apply to the exact same type of events: their underlying physics must be identical to ensure that the same set of parameters is relevant, and their distribution in these relevant variables must be identical. In practice this is not the case, and efficiencies and data to Monte Carlo scale factors determined on one type of events are applied to a slightly different type of events.

Another complicating issue is the Monte Carlo sample itself: it is generated from a combination of physics laws and empirical distributions; it reproduces the data distributions only as well as the underlying processes are modeled. For this analysis, the opening angles of jet pairs in di-jet events are of paramount importance; they are known to be difficult to simulate for b-jets [86]. If the Monte Carlo distribution does not resemble reality closely enough, the efficiency determined from Monte Carlo will be incorrect.

This analysis depends critically on an excellent model of the efficiencies: the analysis signal is a small deviation of the "turn-on" shape that is caused by large changes in efficiencies as a function of the di-jet event's invariant mass. Correcting the Monte Carlo predictions for the efficiencies to match those from data is near impossible: determining the correction factor would require a data sample with a known $Z \rightarrow b\bar{b}$ contribution, to use a matching Monte Carlo sample. But measuring that contribution is one of the required intermediary steps of this analysis.

To solve this challenge, the analysis uses a completely different approach. Here, the efficiencies are determined from data and parametrized in the relevant variables. But the overall signal efficiency is not calculated from Monte Carlo. Instead, *all* data events

are weighted by the inverse of their efficiency.¹ As this analysis will show, this approach depends on a sufficiently large data sample, such that all regions of the phase space are sampled with high statistics.

Thus the data sample itself is used to sample the phase space to determine the overall efficiency. In the limit of an infinite amount of events, this approach gives an unbiased and most precise representation of data events, without any bias from Monte Carlo distributions. Even with a limited number of events the efficiency prediction is well defined: it is unbiased and its uncertainty is simply the statistical uncertainty of the distribution used to derive an efficiency from.

The efficiency for each event is estimated from data, as a function of each event variable it can depend on (for instance an event's jet flavor tags).

4.2 Trigger

The optimal trigger would let all events with $b\bar{b}$ jet pairs pass; its efficiency would be high even for low invariant mass $b\bar{b}$ events to help find a peak on top of the inclusive $b\bar{b}$ background's invariant mass distribution; and it would be enabled for the whole data taking period used in this analysis. Combining samples from several triggers will increase the efficiency by increasing the sample size. But the combination requires an elaborate efficiency analysis due to possible correlations of the triggers [71], which in turn induces systematic uncertainties.

The single trigger *MU_2TRK3_L2M0* was selected because it meets these requirements best, while avoiding the trigger combination problems. All events that were stored because of this trigger in the run number range 161973 to 196584 are considered for this analysis.

In the following subsection, the implementation and efficiency calculation for this trigger will be discussed.

¹Weighting events by their inverse efficiency can be seen as effectively taking into account the events missed by the inefficiency: an efficiency of 1/10 will account for the total of 9 more similar events that would have been visible without inefficiencies.

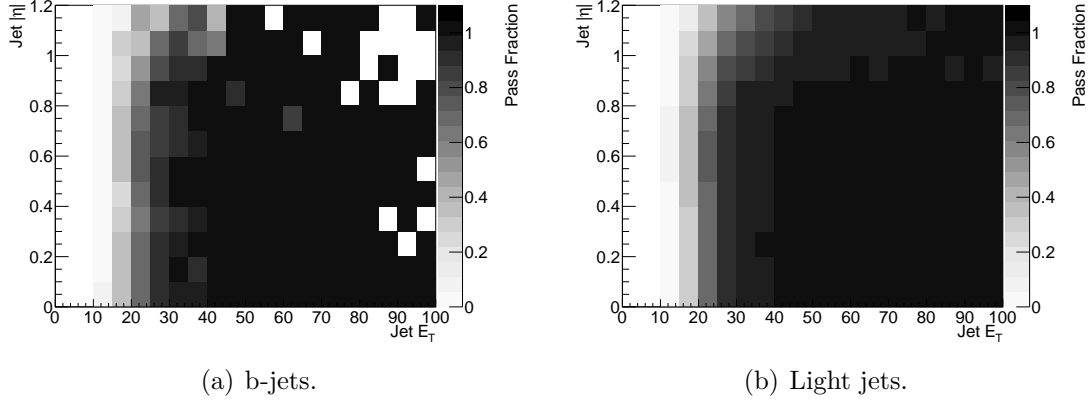


Figure 4.1: CJT(1, 5) efficiency. White bins at higher E_T in the b-jet sample signal an absence of data.

4.2.1 Level 1 Trigger

For the level 1 trigger, both a calorimeter and a muon signal have to be recorded.

Calorimeter Trigger

The *MU_2TRK3_L2M0* trigger requires a level one jet trigger called CJT(1, 5): at least one calorimeter tower must exist with $E_T > 5$ GeV. Even the highest energy tower usually only contains a small part of the energy of a jet. The 5 GeV requirement therefore is not fully efficient even for jets of substantially higher E_T . The pass rate (or efficiency) of jets increases with their energy up to a plateau; the function is called *turn-on*. Fig. 4.1 shows the turn-on for light and b-jets as a function of jet transverse energy and pseudorapidity; Fig. 4.2 shows the corresponding uncertainty. The uncertainty is binomial and thus asymmetric; while in the following the proper asymmetric distribution is used, Fig. 4.2 shows the geometrical mean of the uncertainty.

The efficiency is determined from data using the tag and probe algorithm: a sub-sample is built from all di-jet data events where at least one jet satisfies the L1 trigger requirement. For each event of this sub-sample, the jet satisfying the calorimeter tower requirement is defined as the *tag* jet; if there are two, a random one is chosen as the tag jet. The efficiency is determined on the *other* jet, called *probe* jet. This jet is by definition unbiased, due to the tag jet already satisfying the calorimeter tower requirements. The CJT(1, 5) efficiency is then given as the fraction of probe jets satisfying the L1 trigger requirement.

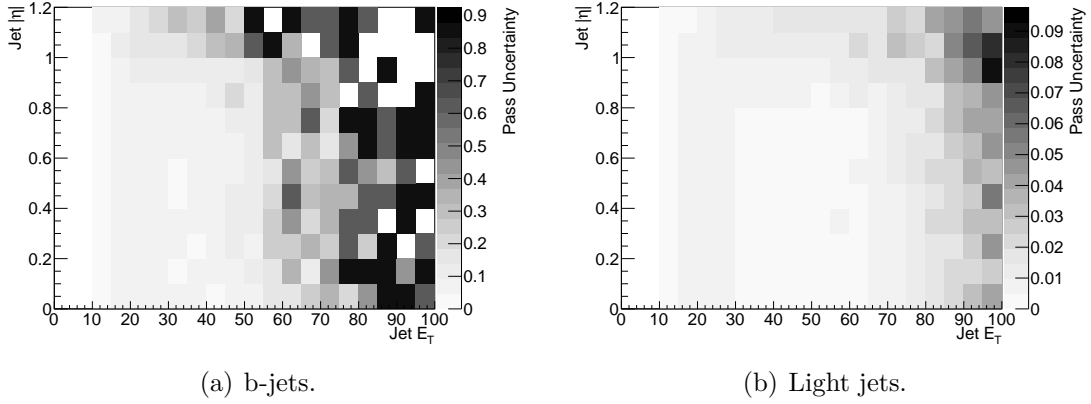


Figure 4.2: Uncertainty on the CJT(1,5) efficiency.

The efficiencies are parametrized as a function of the jet’s $|\eta|$ and the jet’s transverse energy without jet energy scale correction, E_T^{uncorr} . The uncorrected version of the jet E_T resembles more closely what the calorimeter and as a consequence the trigger systems see; it is thus a more appropriate variable for parametrizing the jet trigger turn-on.

The $|\eta|$ dependence, while small, is included to correctly take into account different $|\eta|$ distributions of the samples used in this analysis. The response starts to be different for pseudorapidities where part of the jet is beyond the barrel region, see Fig. 3.5. The additional material between the barrel and the forward calorimeter cause the jet to shower closer to the interaction point, increasing the width, spreading the jet across more towers, and thus reducing the average tower deposit compared to a central jet of the same energy. This explains the lower efficiency at higher η .

To reduce systematic effects, the efficiency is not used as the raw histogram but as a parametrized 2d-function that is the result of a fit procedure. One such systematic effect is missing data, visible as white bins at higher E_T for the b-jet sample in Fig. 4.1a. Because the parametrization takes into account knowledge about the functional behavior of the efficiency (for instance its symmetry in η , the plateau at high E_T), the parametrization can cover (“fill”) the gaps left by bins with low statistics.

The parametrization uses the function

$$\varepsilon_{\text{CJT}(1,5)}(E_T^{\text{uncorr}}, \eta) = p_0^{[1]}(\eta^2) * \left(1 + \text{erf} \left(\frac{\sqrt{\log(E_T^{\text{uncorr}}) - p_1^{[2]}(\eta^2)}}{p_2^{[1]}(\eta^2)} \right) \right) \quad (4.1)$$

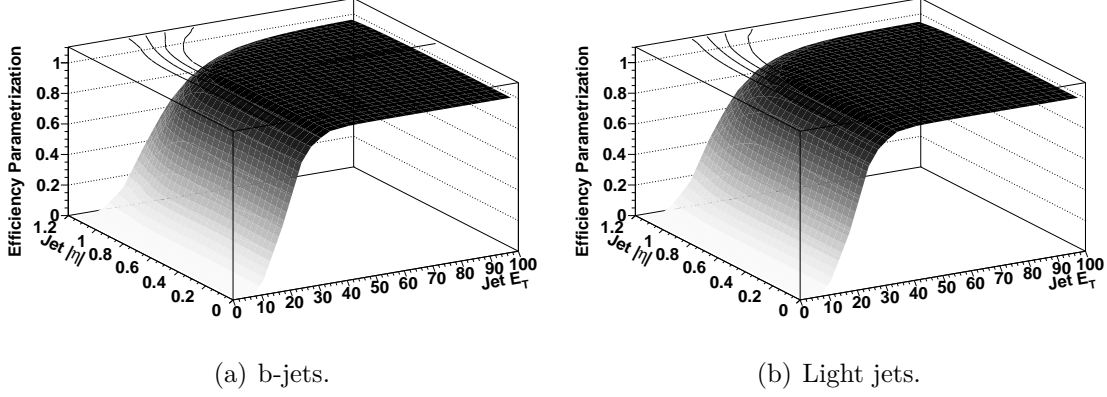


Figure 4.3: Parametrization of the CJT(1,5) efficiency.

with $p_i^{[n]}$ being an n -th order polynomial. The factor $1 + \text{erf}$ sigmoid is a common parametrization for trigger efficiency. It produces a smooth turn-on from zero to a plateau. The parametrization by η^2 allows for a symmetrical parametrization around $\eta = 0$, with a zero derivative at $\eta = 0$.

The parametrization's minimization procedure uses the asymmetric uncertainties on the efficiency: it minimizes the χ^2 of the difference between the measurement and parametrization, using the upper measurement uncertainty if the parametrization is higher than the measurement and the lower uncertainty otherwise. The result of the minimization of the parametrization is shown in Fig. 4.3. The 1σ confidence interval $\sigma \varepsilon_{\text{CJT}(1,5)}(E_T^{\text{uncorr}}, \eta)$ of the parametrization, shown in Fig. 4.4, is used as uncertainty on the parametrization. It is determined from the fit parameters' covariance matrix. For bins that do not have a confidence interval because of a lack of data, the efficiency uncertainty is determined as a linear regression from the eight neighboring bins, taking the distance of the bin center into account.

Using the fraction $r_{\text{CJT}(1,5)}(E_T^{\text{uncorr}}, \eta)$ of jets passing the selection, the pull of the fit can be calculated:

$$p_{\text{CJT}(1,5)}(E_T^{\text{uncorr}}, \eta) = \frac{r_{\text{CJT}(1,5)}(E_T^{\text{uncorr}}, \eta) - \varepsilon_{\text{CJT}(1,5)}(E_T^{\text{uncorr}}, \eta)}{\sigma \varepsilon_{\text{CJT}(1,5)}(E_T^{\text{uncorr}}, \eta)} \quad (4.2)$$

The distribution of the pull is shown in Fig. 4.5; the distribution of the counts of pull values is shown in Fig. 4.6. Neither of them are used directly in this analysis; they serve as illustration of the quality of the parametrization.

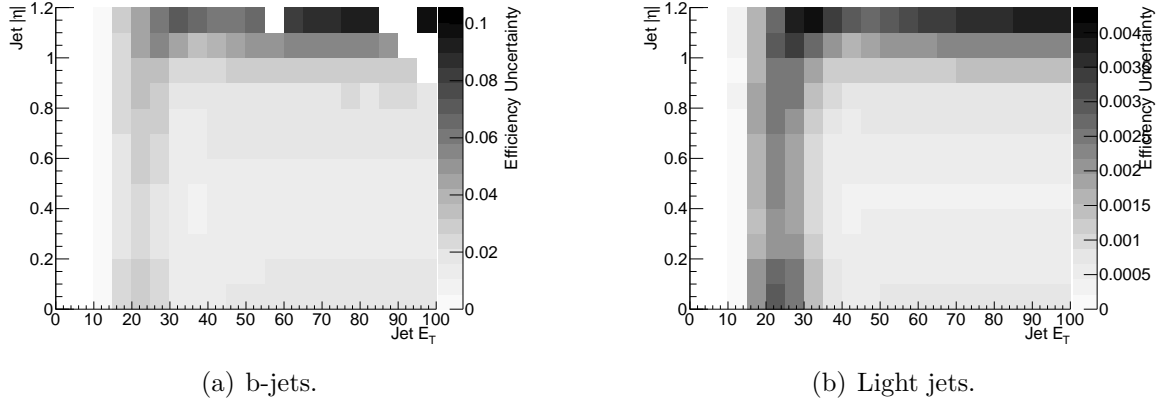


Figure 4.4: Uncertainty on the CJT(1, 5) efficiency parametrization as a function of jet E_T and jet η .

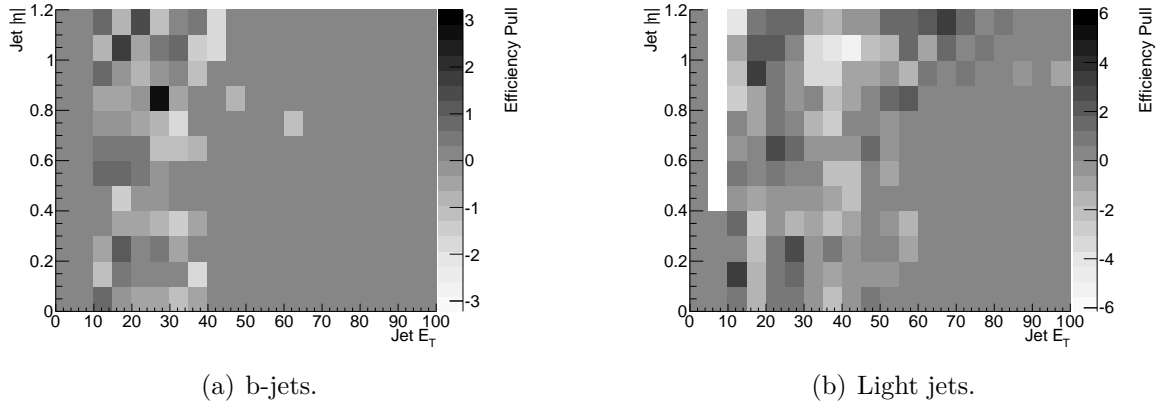


Figure 4.5: Distribution of pull values of the CJT(1, 5) efficiency parametrization as a function of jet E_T and jet η .

This analysis uses the parametrized efficiency and its 1σ confidence interval as the uncertainty of the efficiency.

As the pull distribution shows, the parametrization describes the measurement well. Also for light jets, the pull distribution follows a Gaussian distribution — but its width shows that either the parametrization is not adequate, or its uncertainties are mis-estimated. Fig. 4.5b shows that for instance the region around $E_T = 35$, $\eta = 1$ is not well modeled. A different parametrization has been attempted, shown in Fig. 4.7. It describes the data around $E_T = 35$, $\eta = 1$ better, but exhibits an overall pull distribution that corresponds less to a Gaussian distribution than the original parametrization. The original parametrization thus describes the overall efficiency distribution better. The

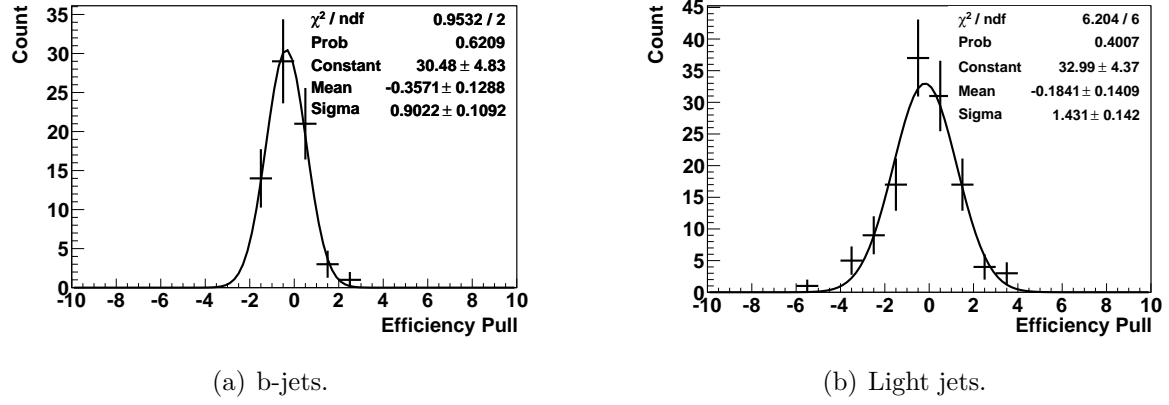


Figure 4.6: Pull values of the CJT(1,5) efficiency parametrization.

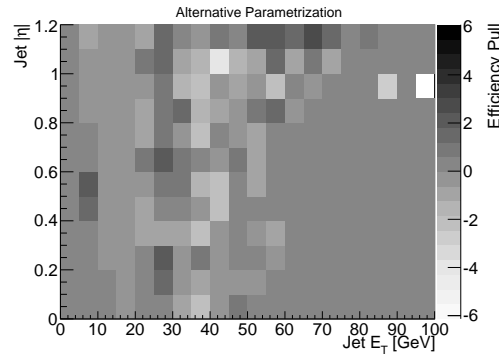


Figure 4.7: Distribution of pull values of a different CJT(1,5) efficiency parametrization as a function of jet E_T and jet η .

analysis was performed with this second parametrization, too; the differences will be discussed in Section 5.4.

Muon Trigger

In the first level trigger, the trigger *MU_2TRK3_L2M0* requires one “tight” muon scintillator signal called *mu1ptxatxx*, which is allowed to be recorded in the full muon system instrumented for triggering, i.e. not only in the central part but extending to $|\eta| < 2$. The tightness of the scintillator triggers refers to the requirement of coincidences between signals in at least two scintillator layers. There is no requirement for the muon PDT signals, i.e. no p_T threshold.

The efficiency for this trigger is determined as part of the jet’s muon association probability in Section 4.3.1. Muons passing the association requirements must have a level 1 scintillator signal associated with them, such that they could have caused this trigger to fire.

4.2.2 Level 2 Trigger

The trigger term *MU_2TRK3_L2M0* introduces a refinement of the muon trigger at Level 2, compared to the trigger requirement at level 1. At least one level 2 muon candidate must be found that has medium quality, without any region or p_T requirements. A muon candidate has medium quality if it has 3 PDT hits. Additionally, track fragments from within the A-layer must either show a drift time that matches the candidate’s track fit, or have an associated A-layer scintillator hit. BC-layers, on the other hand, must have hit patterns that include both B and C layers or an associated Cosmic Cap scintillator hit to be accepted as medium quality level 2 trigger muons. The exact procedure to define a medium quality level 2 muon candidate is explained in [70].

4.2.3 Level 3 Trigger

Level 3 of the trigger requires two tracks with $p_T > 3 \text{ GeV}$ to be found by the trigger system. While this looks like an additional requirement, it is almost always satisfied for events passing the level 1 and 2 criteria of this trigger, because all events are required to have at least one muon, essentially all identified muons have a $p_T > 3 \text{ GeV}$, and generally

because most hard interactions lead to a sizeable number of tracks with $p_T > 3 \text{ GeV}$. The probability of the tracks embedded in the events' two jets to provide one or two of the trigger tracks is also sufficiently high. The signal sample of this analysis is a double-muon tagged b-jet sample; the trigger term's efficiency is thus expected to be even higher for this signal sample because of the two required muons, each having the ability to satisfy the trigger requirement independently. The light jet sample used in this analysis is anti-JLIP tagged (see Section 4.3.3). This requires this sample's jets to have two tracks associated with them; that, too, increases the (already high) efficiency of this trigger.

Track Trigger

The trigger's *GlobalTracker* tool must find at least two tracks with $p_T > 3 \text{ GeV}$. As shown above, we can assume a sufficiently high efficiency of this trigger requirement. The matching efficiency between the level 3 muons (which are not used in this analysis but can be assumed to be of equal or inferior quality to the offline muons) and the level 3 *GlobalTracker* for 5 GeV muons was determined to be 99.4% [19]. The efficiency of the *GlobalTracker* in simulated $t\bar{t}$ events is greater than 90% for 3 GeV tracks [85] and — if tracks with large amounts of shared hits are excluded — greater than 95% with almost no dependence on track p_T . With the trigger's lack of dependence on p_T this inefficiency is expected to not introduce a kinematic bias. Instead of parametrizing the efficiency, a systematic uncertainty is assigned to the cross section measurement. Given the number of tracks and muons in signal events, a systematic uncertainty of 1% is attributed to the effect of the track trigger. This is a conservative estimate: with an efficiency of 95% per track, the inefficiency caused by the trigger on signal events from the b-jet sample is $< 1\%$ only due to the muons associated to the two jets. For background events, the inefficiencies are expected to cancel as a consequence of the background subtraction procedure used in the signal extraction (see Section 5).

4.3 Offline Object Identification

This analysis depends on the reconstruction of muons and jets, in particular b-jets, from the detector readout. First, the muon reconstruction and the resulting efficiency, purity and muon track parameter resolution will be discussed and subsequently the jet reconstruction and the jet energy determination.

4.3.1 Muons

Offline reconstructed muons are used for tagging b-jets (see Section 4.3.3) by associating them with jets. The efficiency for muons is determined as an overall efficiency for online and offline reconstruction and triggering, including physics parameters such as the probability of a b-jet or a light jet to contain a muon. Properties of the offline reconstructed muon serve as the parametrization of that combined efficiency.

Muon Reconstruction

Muons are reconstructed from wire and scintillator hits in the muon detector from all three layers A, B, and C, and from the tracks reconstructed in the central tracking detector.

Muon Detector Hits that occur in the muon detector outside the collision time window $|t_{\text{cosmic}}| \leq 10 \text{ ns}$ are rejected; they are assumed to stem from atmospheric muons (*cosmics*).

Accepted muons must have at least two A layer wire hits, at least one A layer scintillator hit, at least two BC layer wire hits, and at least one BC layer scintillator hit, corresponding to DØ's medium reconstruction criteria with $nseg = 3$.

Straight lines in the (η, ϕ, r) -space are fitted through the hits in the B and C layers, and independently through the hits of the A layer; they are called A and BC segments. For an A and BC segment pair to be taken into account for a possible matching, they have to come from overlapping octants, and their $\Delta\phi$ is required to be below 0.3.

An A and a BC segment are combined by fitting their hits, taking into account the toroid's magnetic field, the energy loss in the toroid and multiple scattering in the toroid. This yields a muon-system based muon candidate with defined position and momentum information and corresponding error matrix. The procedure to build candidates from the muon system is detailed in [41].

Due to support structures holding the DØ detector, the lower part of the muon detector is not fully instrumented, leading to considerably lower muon reconstruction efficiencies in that region. Instead of determining these efficiencies, muons that hit the A layer in the slice $225^\circ \leq \phi \leq 310^\circ$ are not taken into account in this analysis. This

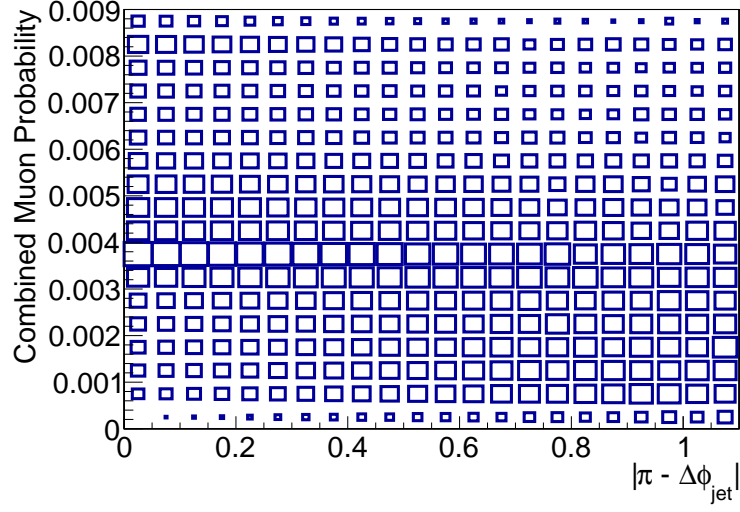


Figure 4.8: Combined muon probability (see Section 4.3.1) as a function of $|\pi - \Delta\phi_{\text{jet}}|$, normalized for each $|\pi - \Delta\phi_{\text{jet}}|$ bin for better comparability.

geometric acceptance cut decreases the overall muon reconstruction efficiency by the factor $\varepsilon_{\text{hole}}^{\text{muon}} = 0.76$, i.e. by 24%.

This cuts makes ϕ_{muon} a nontrivial parameter. As a consequence, ϕ_{jet} (because of the association criterion) and thus $|\pi - \Delta\phi_{\text{jet}}|$ become nontrivial, too. The combined muon probability, introduced in Section 4.3.1, is the variable with the highest dependency on the muon hole: it is close to 0 in the hole but close to 1 outside of the hole. This analysis does not use ϕ but $|\pi - \Delta\phi_{\text{jet}}|$ as a parameter. As can be seen in Fig. 4.8, there is no significant dependency of the muon probability on $|\pi - \Delta\phi_{\text{jet}}|$; existing dependencies are likely caused by correlations of the event topologies and efficiencies. The analysis does thus not need to take ϕ as a parameter into account, despite the nontrivial ϕ_{muon} .

Combination with Central Tracking System The muon detector’s candidate is combined with tracks reconstructed from the hits of the central tracking system. Muon system candidates are propagated to the central tracking system, and matched with all central tracks, using both the muon candidate’s and the track’s full error matrix. If such a match yields a $\chi^2/\text{d.o.f.} < 10$, the combination (a reconstructed muon) is taken into account for this analysis; the muon’s momentum and position is defined as the central track’s momentum and position.

All tracks with $p_T > 1 \text{ GeV}$ that have not been assigned to a muon during the first matching pass are extrapolated to the muon detector’s A layer. They are again

matched with the remaining muon candidates from the muon system; combinations with $\chi^2/\text{d.o.f.} < 10$ are also taken into account for this analysis. Also for these extrapolated tracks, the reconstructed muon's momentum and position is defined purely by the central track.

The lower the reconstructed muon's momentum, the higher the probability that this muon is mis-reconstructed, i.e. not reconstructed based on a muon particle passing through the detector, but because of combinatorics of random hits. Muons must also have a minimum momentum of about 3 GeV to be able to pass the toroid. Because of these two reasons, reconstructed muons are required to have a transverse momentum $p_T > 3 \text{ GeV}$.

The muons used in this analysis are required to have at least one scintillator hit. They must fulfill any two out of the following three requirements:

- at least two wire hits in the B or C layers,
- at least one scintillator hit in the B or C layers,
- at least two wire and one scintillator hits in the A layer.

Alternatively, they may have at least one scintillator and two wire hits in any layer and be matched to a central track. They correspond to DØ's *loose* muon candidates with the additional requirements of a central track match with $\chi^2/\text{d.o.f.} < 10$ and a transverse momentum $p_T > 3 \text{ GeV}$.

Efficiencies The reconstruction efficiencies are discussed in detail in [38]. For this analysis, a breakdown in different sources of muon inefficiencies (trigger or reconstruction) is not relevant. As a matter of fact, the muon is only used to tag jets. The only relevant measure for this analysis is the probability to find a muon in the reconstructed data for a b- or light jet, respectively. These values are a combination of

- the probability that the muon caused the muon trigger to fire;
- the probability that the reconstruction software reconstructs a muon;
- the probability that the reconstructed muon is associated to a b-jet or light jet.

A muon is associated to a jet if it is within $\Delta R = \sqrt{\Delta\eta^2 + \Delta\phi^2} < 0.5$ of the jet axis, and if there is no closer jet in R -space. To satisfy the requirements, the reconstruction software can either reconstruct a muon particle (which exists for about 15% of all b-jets)

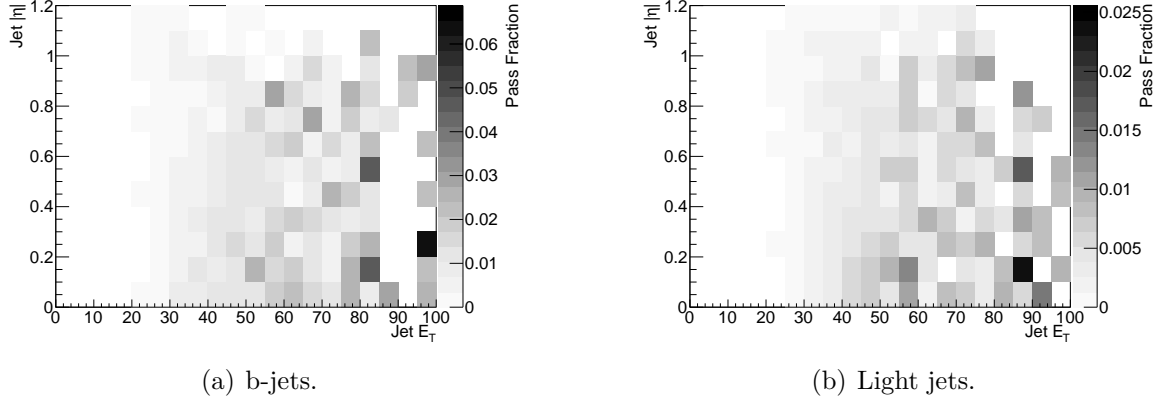


Figure 4.9: Combined muon probability (trigger, reconstruction, and analysis cuts) as a function of the associated jet’s E_T and η , determined with the tag and probe algorithm.

or misinterpret the detector readout (fake). The probability to associate a muon to a jet is determined by the tag and probe algorithm as introduced in Section 4.2.1. This probability is a convolution of the branching ratio (i.e. the production probability) and its detection and reconstruction efficiency. It is parametrized in jet- E_T and jet- η . This is an uncommon parametrization for muons, which are normally characterized in their own p_T and η . But as in this analysis the muons merely play a tagging role for the jets, the properties of the muon are less relevant.

Ideally, one would want to determine the combined muon probability for the b-jet sample. But as that consists of di-jet events where both jets are associated with a muon, one cannot find an unbiased jet for probing. Instead, the efficiency is estimated by using a sample of di-jet events with one jet being associated to a muon (the “tag” jet). The other, “probe” jet must be JLIP tagged at the “loose” working point (see Section 4.3.3) to increase the fraction of probe b-jets, i.e. in the end to get to a b-purity that is similar to that of the original b-jet sample.

The requirement of a JLIP-tagged jet can introduce a bias on the muon association efficiency. This analysis uses $P(\text{muon}|\text{JLIP}) = P(\text{muon})P(\text{JLIP}|\text{muon})/P(\text{JLIP})$. As has been shown in [29], the JLIP tagging efficiency does not depend on the presence of a muon: $P(\text{JLIP}|\text{muon}) = P(\text{JLIP})$. Thus $P(\text{muon}|\text{JLIP}) = P(\text{muon})$; the requirement of a JLIP tag should not affect the efficiency of the muon association.

The combined muon trigger and reconstruction efficiency is shown in Fig. 4.9. As expected, the probability rises with jet E_T : larger jet E_T means on average a larger

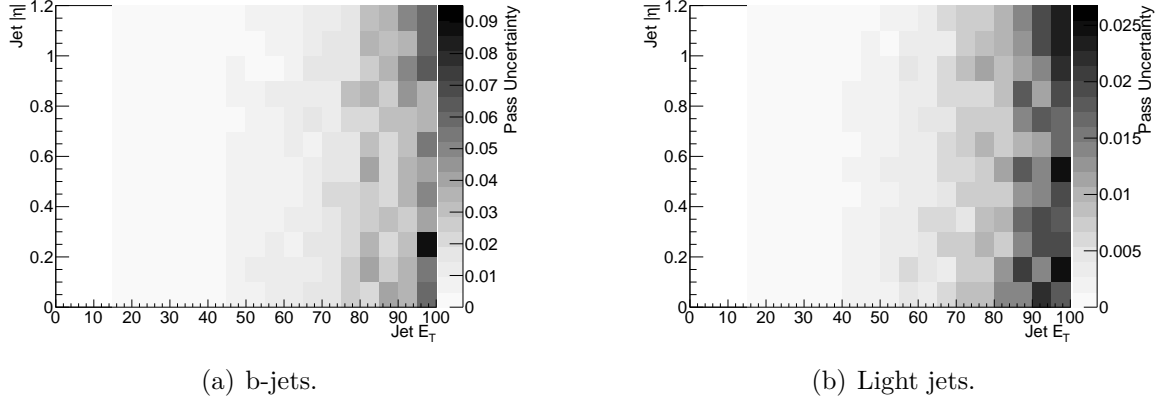


Figure 4.10: Uncertainty on combined muon probability (trigger, reconstruction, and analysis cuts) as a function of the associated jet’s E_T and η , determined with the tag and probe algorithm.

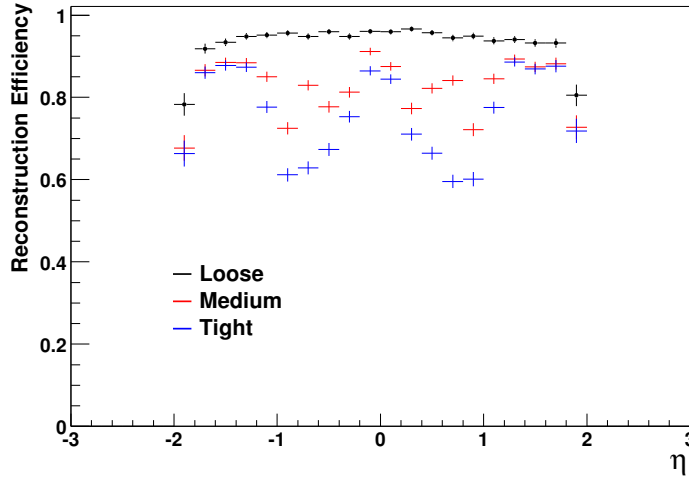


Figure 4.11: Muon reconstruction efficiency as a function of muon η for different quality requirements for muon candidates; from [38].

muon p_T , which in turn increases its probability to fire the muon trigger and to be reconstructed. The geometric mean of the asymmetric, binomial uncertainty on the efficiency is shown in Fig. 4.10.

To reduce systematic effects, the combined muon probability is not used as the raw histogram but as a parametrized 2d-function that is the result of a fit procedure.

This parametrization uses a sigmoid (erf) to model the turn-on. Two Gaussians model detector effects; one centered at $\eta = 0$ and one centered at $|\eta^{\text{jet}}| = 0.5$. The muon reconstruction efficiency, determined in [38], motivates this parametrization, see Fig. 4.11.

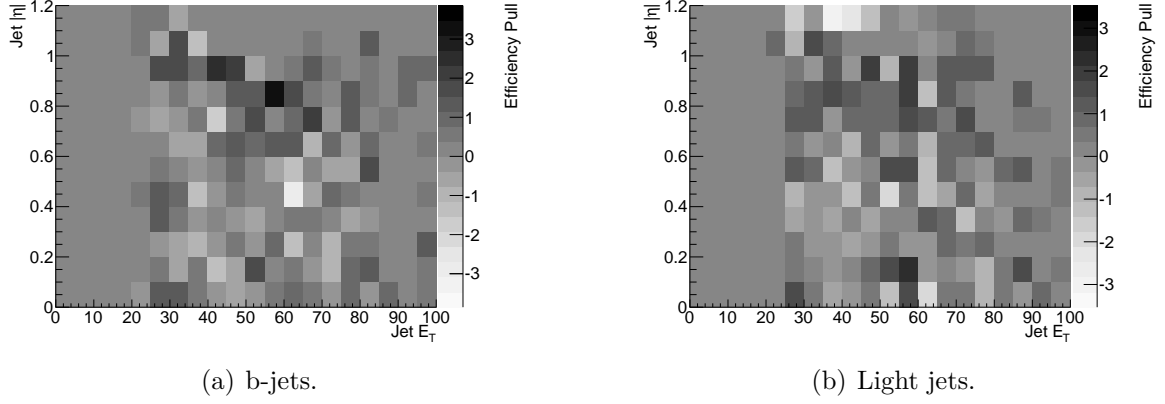


Figure 4.12: Pull distribution of the muon probability parametrization as a function of the associated jet's E_T and η .

The muon selection criteria and the event selection (for instance in jet η) will likely have an impact on the reconstruction efficiency determined in [38]. This analysis is thus (re-)determining it as one element of the combined muon probability.

Nonetheless, this combined muon probability must show similar features as the reconstruction efficiency for the very similar medium muons. It thus needs a complex η dependence with a local minimum around $\eta \approx 0.5$. For the reconstruction efficiency, this is really the muon's η , which on average corresponds to the jet η . The two dimensional fit function is

$$\begin{aligned} \epsilon_{\text{muon}}(E_T^{\text{jet}}, |\eta^{\text{jet}}|) &= \left(1 + \text{erf}\left(\frac{E_T^{\text{jet}} - p_0}{p_1}\right)\right) \\ &\quad * p_2 * \left(\text{Gaus}(|\eta^{\text{jet}}|, 0, p_3) - p_4 * \text{Gaus}(|\eta^{\text{jet}}|, 0.5, 0.2)\right) \end{aligned} \quad (4.3)$$

with $\text{Gaus}(x, \mu, \sigma)$ describing a Gaussian of mean μ and width σ at x . The fit procedure takes the asymmetric uncertainties on the efficiency into account.

The pull is calculated for this parametrization using the same procedure as for the CJT(1,5) efficiency in Section 4.2.1. Its distribution is shown in Fig. 4.12; the occurrences of pull values and their Gaussian parametrization are depicted in Fig. 4.13. The parametrized combined muon probability is shown in Fig. 4.14; its uncertainty (1σ confidence interval) is shown in Fig. 4.15.

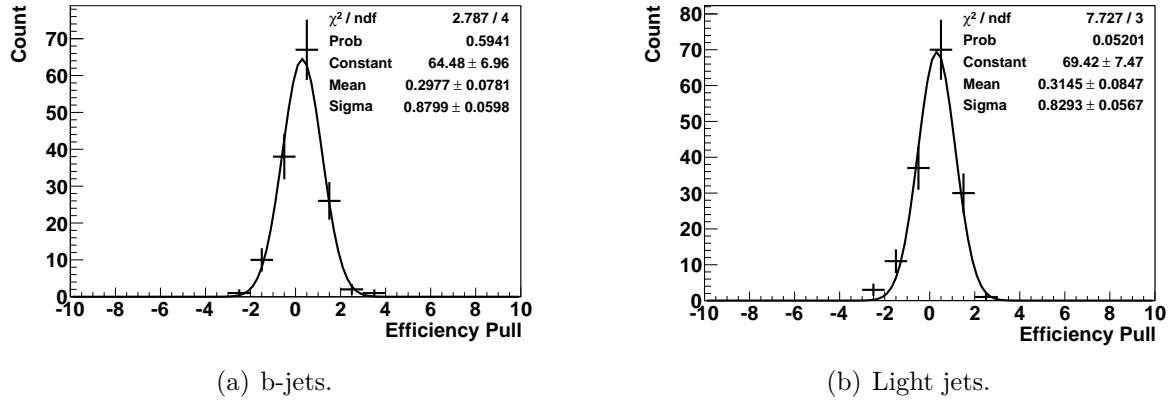


Figure 4.13: Distribution of pull values of the muon probability parametrization.

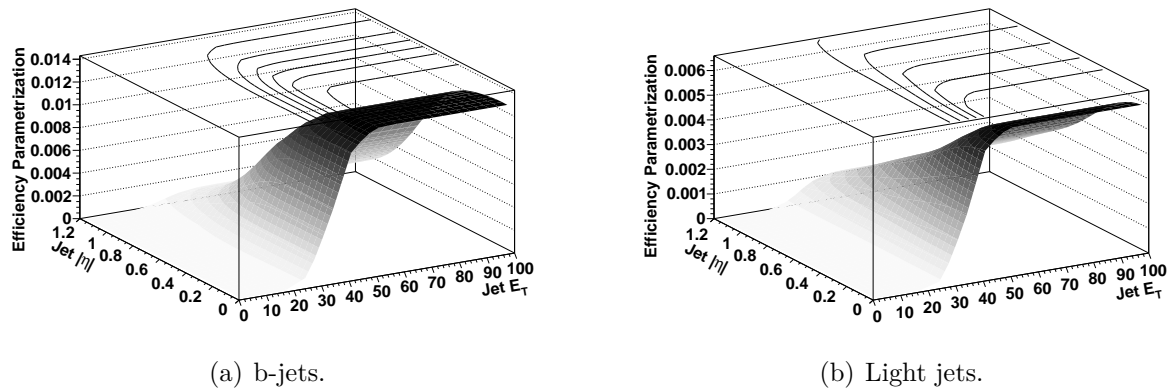


Figure 4.14: Parametrization of the combined muon probability (trigger, reconstruction, and analysis cuts).

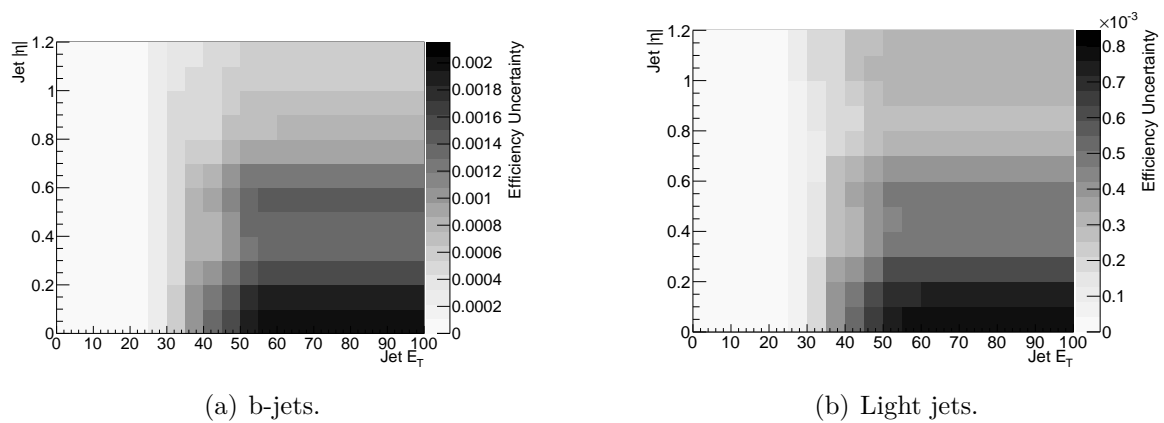


Figure 4.15: Uncertainty on the muon probability parametrization.

Muon Momentum Resolution

The muon momentum resolution influences this analysis only indirectly: it determines the turn-on of the 3 GeV muon transverse momentum cut-off and the width of the jet energy scale correction which takes muons associated to (assumed b- and c-) jets into account, see Section 4.3.3.

The momentum resolution is influenced by multiple scattering, the measurement precision of the single hit position, and the reconstruction algorithm: multiple scattering will deviate the muon from the path it would have without material. For the muon momenta considered in this analysis, multiple scattering in the central tracker can be neglected.

The precision of the detector’s positional measurements is the foundation of the track fit done by the reconstruction software, its precision is thus a fundamental ingredient and a lower limit for the momentum resolution. The limited positional precision is mostly due to imprecisions in the signals’ readout (timing, pileup², etc.) and misalignment of detector parts. The muon detector elements with their respective positional measurement precision have been described in Section 3.5.

The reconstruction algorithm might assign hits to the wrong candidate tracks, miss hits, or not take detector misalignment into account properly. The overall momentum resolution has been determined in [38]. This was done in two steps: first, the resolution predicted by Monte Carlo studies was confirmed to be comparable to the measured resolution for a given signal, in this case $J/\psi \rightarrow \mu^- \mu^+$. With this confirmation, the resolution of reconstructed muon Monte Carlo tracks was compared to the Monte Carlo truth. The muon momentum resolution has been determined as $\sigma \left(\frac{\Delta(1/p_T)}{1/p_T} \right) = 0.011 + 0.0021 p_T$.

4.3.2 Jets

Jets are reconstructed from the calorimeter’s measurements. The precision of this reconstruction influences the precision of this analysis. Common effects include jets that have not being identified by the reconstruction, fluctuations where the “center” of a jet

²Pileup is the phenomenon where more than one interaction is measured, either due to multiple interactions during the same beam crossing, or due to slower subdetectors’ readout that integrate the measurement over multiple bunch crossings. In either case the detector sees the superposition of the interactions as one event.

is not the direction of the outgoing parton, and misinterpretation of the calorimeter's signal response when translating it into a jet's energy. Because many b-jets come with a high-momentum neutrino they pose additional problems to the jet reconstruction requiring additional corrections, as shown in Section 4.3.3.

Jet Reconstruction

The calorimeter is subdivided into cells (see Section 3.4.2). For this analysis, the *DØ Run II “Improved Legacy” Cone Algorithm* (see [31]) with a cone size of $R = 0.5$ and the T42 correction (see also [83] for the algorithm, [27] for the effects on jet identification) was used to combine these cells into jets.

Cells with the same angular position are merged into towers; those energetic enough are used for creating jet candidates (*seeds*) for the jet reconstruction. Active cells surrounding these seeds within the cone region are assigned to the jet candidate, with the nominal interaction point being the cone's origin. In a final step, overlapping jets are merged into a new jet candidate, or the overlap region is appropriately distributed over the jets. The jet's position is determined as the center of gravity of the participating clusters. The jet's direction follows from pointing to the jet center from the interaction point.

The algorithm is described in detail in [28]; this chapter focuses on the parts relevant for the discussion of this analysis. The efficiency of the jet reconstruction and identification is $> 95\%$ for jets with $E_T > 20$ GeV and $> 99\%$ for jets with $E_T > 50$ GeV as determined by the JetID certification version 1.2. The procedure is described in [58]. It also shows that Monte Carlo predicts the reconstruction efficiency well; the scaling factor between data and Monte Carlo is between 0.95 and 1 for jets with $E_T > 20$ GeV. The precise parametrization of the efficiency is not relevant for this analysis: as laid out in Section 5, the analysis compares samples for which the parametrization is expected to be sufficiently similar to cancel deviations of the simulated efficiencies. This means that the jet reconstruction efficiency is modeled well enough to use Monte Carlo to simulate it for this analysis; no additional correction factor is used.

Jets with $E_T < 15$ GeV have not been studied as part of the jet ID certification. They are not known well enough to be included in this analysis. Jets are also required to be central within $|\eta| < 1.2$, simplifying the trigger efficiency determination at the expense of

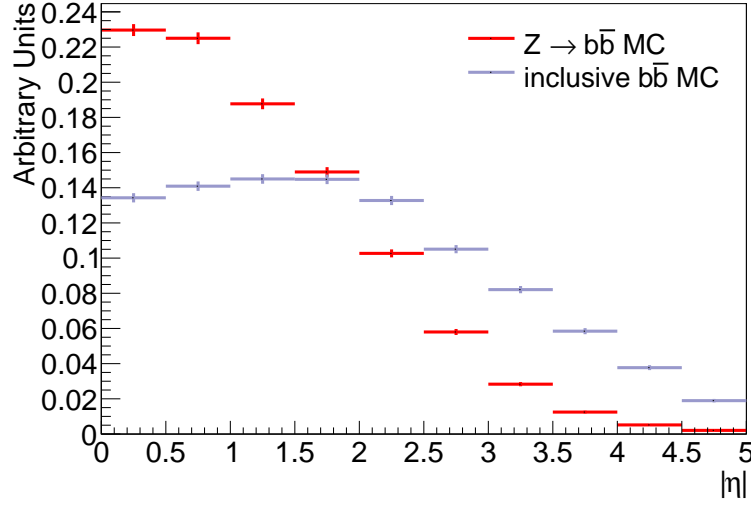


Figure 4.16: Monte Carlo simulation of the $|\eta|$ distribution for jets from a $Z \rightarrow b\bar{b}$ decay and inclusive b production.

decreasing Z-boson yield by more than a factor two, as shown in Fig. 4.16. Incidentally, this η cut also reduces the background from inclusive b-jet production.

These jet selections and the di-jet selection are the only cuts not modeled with an event weight, as outlined in Section 4.1. Instead, the same cut is applied to the Monte Carlo signal prediction. Even though this might seem inconsistent, this approach is in fact advantageous for two reasons: the simulation of the jet E_T and multiplicity distributions are well understood and reliable. On the other hand it is not in the scope of this analysis to analyze the (non trivial) signal efficiencies of these cuts from data. It is thus more consistent to apply the cuts also to Monte Carlo, which is used to determine the efficiencies to begin with.

Jet Energy Scale

The decay of intermediary particles, for instance inside jets, as well as the decay of leading b- and c-hadrons can produce neutrinos. Neutrinos do not contribute to the calorimeter's energy measurement of these jets. The fraction of the total jet's energy that is carried by neutrinos cannot be measured directly, and must be inferred from theoretical or heuristic models, or from measurements using the production of a momentum balanced pair of a jet and a photon, as an average property of jets. These parametrizations allow a correction of the jet energy measured by the calorimeter detectors to the expected energy of the parton that formed the jet.

The jet energy scale analysis is an integral part of the $D\bar{O}$ jet calibration [63]. It uses events with a single jet and a non-associated electromagnetic shower. The absolute value of a jet's energy is determined by the relatively clean recoil of a quark or a gluon versus a photon; their transverse energies must be identical. The photon's energy can be determined by the electromagnetic part of a calorimeter, which in turn can be calibrated by electron pairs from Z , Υ and J/ψ decays. Still, a systematic uncertainty on the jet energy calibration persists. Sources include out-of-cone showering, i.e. fragmentation and decay products that escape from the jet's cone; the unknown fraction of energy that is carried by neutrinos (with a noticeable jet flavor dependence); and the limited resolution of the calorimeter.

The correction can have different goals: it can e.g. be optimized to correspond to the particles that are part (i.e. within the cone) of the jet, or to reflect the energy of the incoming parton that created the jet through hadronization. Here, the jet should reflect the energy of the quark that was generated by the Z decay, which in turn means the jet's parton correction is most suitable. The analysis uses the jet energy correction version 5.3, which is the final version for the reconstruction software that was used to reconstruct the analysis' data samples. A dedicated jet energy correction is applied to jets that have been identified as b-jets. It is discussed in Section 4.3.3.

4.3.3 b-Jets

As will become clear in Chapter 5, the analysis needs two samples: a collection of di-jet events where both jets stem from the hadronization of b-quarks, and a collection where both jets stem from gluons, u-, d-, s- and — as little as possible — c-quarks. This implies the need for jet flavor tagging. Two approaches are used: anti-JLIP for the tagging of light jets, and double soft-lepton tagging for the identification of b-jets.

Soft Lepton Tag

Muons are considerably easier to identify by particle detectors than electrons or taus, due to their long lifetime and minimal interaction (their particular mass and relative stability make them minimum ionizing particles over a wide momentum range). This makes semi-leptonic decay to muons the preferred channel for this analysis: only events with at least one muon per jet are accepted in the b-jet sample. To determine the trigger efficiency for light jets, events from the light jet sample (see Section 4.3.3) are required to

have at least one jet with a muon associated to it. The association is defined as before: a muon with $p_T > 3 \text{ GeV}$ that is within $\Delta R < 0.5$ of the jet axis, and for which no other, closer jet exists.

The b-hadrons decaying to muons can be used to increase the fraction of b-jets in a sample that would otherwise be dominated by light jets. Tagging one jet leaves a considerable fraction of events with light jets pairs in the sample. Even if one of the jets was produced by a b-quark, events exist where the $b\bar{b}$ -jet pair is merged, and balances with a light recoil jet. These recoil events exhibit a completely different invariant mass spectrum; it is thus desirable to exclude them from the b-tagged sample. The cleanest solution — with respect to systematic uncertainties — is to simply require both jets to have a muon associated with them, even though about $1 - 0.15 * 0.15 \approx 98\%$ of all b-hadrons are rejected by introducing this requirement, given that about 15% of the b-hadrons' decays result in a muon [26].

Performance The performance of the soft lepton tag is determined as part of the muon tag efficiency described in Section 4.3.1. The tag's purity is not as relevant for the analysis because possible light jet ingredients cancel as part of the background subtraction that will be discussed in Section 5.3.4. The performance of the soft lepton tag is evaluated in Section 4.4.1.

b-Jet Energy Scale

A major difference between light and b-jet energy scales is introduced by requiring a muon to be associated to both of the event's jets. This decay process also produces a neutrino; neutrinos do not leave any traces in the detector. A goal of the b-jet energy scale is thus to account for the energy carried away by the neutrino. One cannot algorithmically determine the exact energy of the neutrino. The expected, average neutrino energy scales with both the jet's and the muon's momenta. The scale factor is determined from Monte Carlo; it is part of the jet energy correction certification version 5.3 [63]. As an example for the neutrino-induced jet energy correction, a distribution of the jet energy correction factor solely due to an associated muon (i.e. the multiplicative factor on top of the intrinsic jet energy correction factor without muons) is shown in Fig. 4.17. This distribution is for jets from data events with only one reconstructed vertex, which have an associated 5 GeV muon with $\Delta R = 0.14$ from the jet axis.

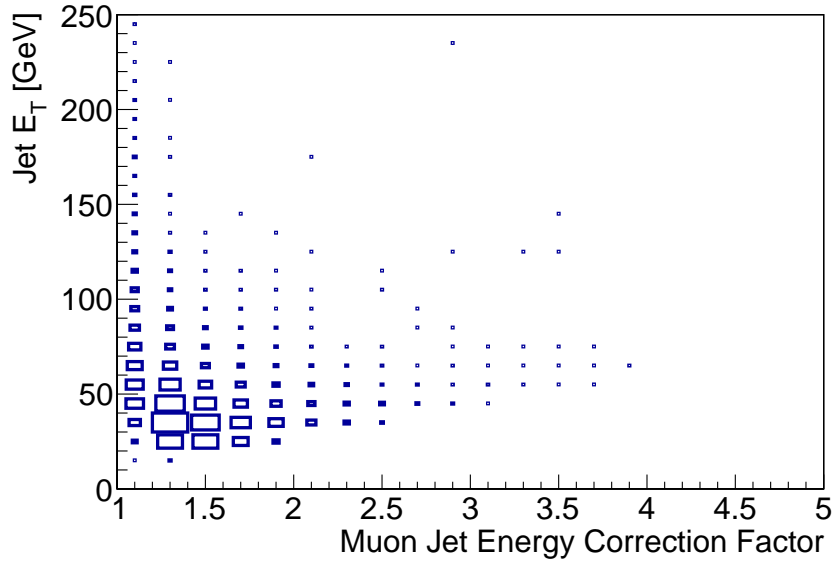


Figure 4.17: Distribution of DØ's jet energy correction for the muon / neutrino, sampled from the b-jet data sample, as a function of jet E_T .

The current jet energy scale parametrization is based on both theoretical models and Monte Carlo studies at relatively low (compared to m_Z) jet energies. Finding a Z signal would allow to search for a better parametrization of the jet energy scale than those currently used, to improve the energy scale correction to the jet E_T ranges seen in the $Z \rightarrow b\bar{b}$ analysis. These corrections could in turn improve the precision of measurements of the Higgs width with b-jets in the final state.

JLIP

To determine the probability of a b-jet to have a muon associated with it, b-jets must first be identified. This of course cannot be done with a muon-tagged sample; instead an independent, unbiased tag must be used. It has been shown that the track-based impact parameter tag called JLIP (*Jet Lifetime Probability*) is just that [86], see also Section 4.3.1.

Algorithm As introduced in Section 2.4.2, b-hadrons have a typical decay length of a few millimeters. The significant decay length and the high number of charged decay products can be exploited by tracking detectors when searching for b-hadrons: the fraction of b-mesons decaying slightly away from the primary interaction point is much higher than the fraction of b-mesons decaying at the interaction point. The high

multiplicity increases the probability of reconstructing the b-hadron's decay vertex. If such a secondary vertex is reconstructed, and its position is within the beam pipe inside the detector, it can be assumed to stem from the decay of a b-hadron. In fact, this analysis uses a parametrization based on the *impact parameter*: the distance of closest approach of a track to the primary vertex. In contrast to the position of the secondary vertex, the impact parameter only depends on a particle's lifetime (at least to first order), and not on its boost. For particles with a short lifetime, the tracks of the decay products will seem to come from the primary vertex, smeared by resolution effects. For particles with a longer lifetime however, most tracks will have an impact parameter that significantly differs from zero. Moreover, for positive lifetimes the track will originate on the side of the primary vertex in the direction of the jet.

The JLIP algorithm tabulates the tracks' distance of closest approach (DCA) to the primary vertex, for all tracks with $p_T > 0.5 \text{ GeV}$ and within $\Delta R < 0.5$ from the jet axis. The tracks' DCA must be $< 0.2 \text{ cm}$ in the ϕ plane, i.e. perpendicular to the beam axis, and $< 0.4 \text{ cm}$ along the beam axis, and the track must have at least one SMT hit.

The signed impact parameter (IP) is constructed out of a track's DCA in the plane perpendicular to the beam axis. Tracks that have their point of closest approach inside the jet's half-sphere as shown in Fig. 4.18 are assigned a positive IP, the others are assigned a negative sign. The JLIP tag does not use the signed impact parameter directly but its pull, the signed impact parameter divided by its uncertainty.

Without a secondary vertex one would expect the distribution of positive and negative impact parameters (and thus their significance) to be symmetric, being dominated by tracking resolution effects and the decay of short-lived particles. For the long-lived b-hadrons, on the other hand, several particles will be created within the jet's half-sphere, as a decay product of the b-hadron. They thus have positive impact parameters, giving an enhancement of positive impact parameters.

The distribution of the signed impact parameter significance has been studied as a function of a set of parameters, e.g. the tracks' η , p_T , and fit χ^2 . Given a point in this parameter space one can determine the probability for that track to be part of a b-jet. A convolution of the probabilities for all tracks associated with a jet (i.e. within $\Delta R < 0.5$ for the JLIP tag) gives the jet's JLIP tag value [4]. As a prerequisite for applying the JLIP tag the jet is required to be taggable: there must be a reconstructed primary vertex and at least two tracks satisfying the JLIP track requirements, one of which must have a $p_T > 1 \text{ GeV}$.

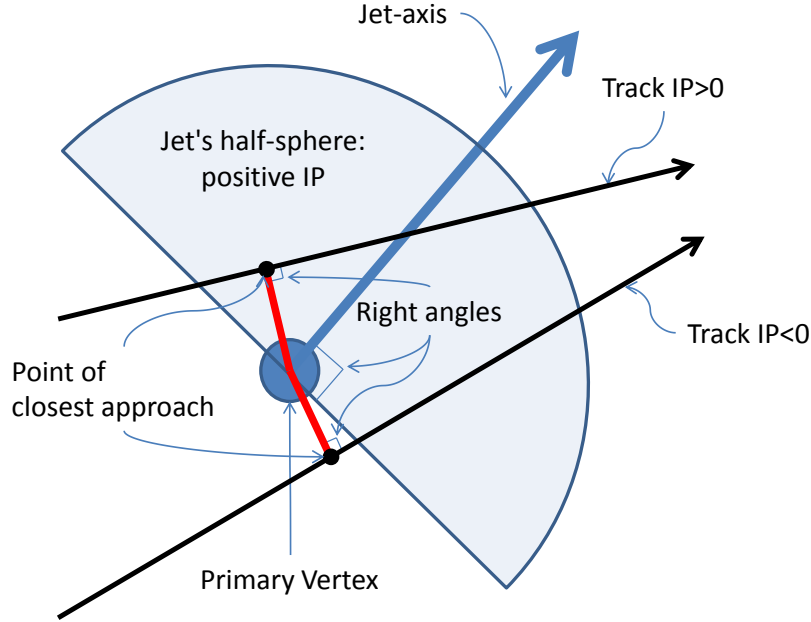


Figure 4.18: Definition of the sign of impact parameters.

Performance Several cut values on the JLIP joint probability have been defined as working points for which efficiency and mistag rate (i.e. the light jet, anti-tag efficiency) have been evaluated. This analysis uses those jets with a joint probability larger than 0.986 (*loose JLIP tag*) for defining b-jets for the muon probability study: the probe jet has to be JLIP tagged when evaluating the muon probability for b-jets.

It also uses the loose JLIP working point for tagging light jets: all jets that are taggable and that are not tagged as b-jets are assumed to be light jets. This anti-tag is required for both jets for an event to be considered as part of the light jet sample. The efficiency for this tag is well known, it is simply the one minus the mistag rate of the working point. Using this anti-JLIP tag thus further increases the already large light-jet purity of di-jet events.

While there might be a difference in the decay length caused by the different Lorentz boosts of b-jets in Z decays and QCD production, the effect is taken into account by parametrizing the JLIP performance as a function of the jet energy and (pseudo-)rapidity. To first order, though, the signed impact parameter significance does not depend on the particles' boost. Hence, only a weak dependence on jet energy is expected.

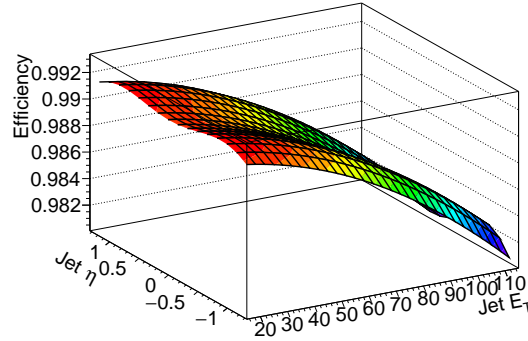


Figure 4.19: Parametrization of the JLIP anti-tagging efficiency, as a function of jet E_T and jet η .

DØ’s parametrizations for the JLIP efficiencies for anti-tagging light jets at the “loose” working point are shown in Fig. 4.19. It does not include the effect of the taggability criterion on the efficiency.

Taggability The fraction of JLIP taggable jets has been studied, even though it is not directly relevant for the result of the signal height efficiency. It does however influence the invariant mass spectrum, as the taggability for low energetic jets is lower. The b-jets used in this analysis are not JLIP tagged but soft lepton tagged; they are not required to be JLIP taggable. The light jet sample, on the other hand, requires both jets to be JLIP taggable, introducing an additional inefficiency varying with the event’s invariant mass. The light jet sample’s taggability must thus be taken into account to make the two samples’ invariant mass spectra comparable.

The efficiency of the taggability criterion is determined from data using the tag and probe algorithm as described in Section 4.2.1. For the determination of the taggability, all events where at most one jet has an associated muon are assumed to be light jet events. Only the tag jet has to be JLIP anti-tagged. The light flavor jet sample used in the taggability determination will thus still contain some b-jets. The b-jet contamination is small due to the much higher light flavor jet cross section. The exclusion of the double muon tagged events, on the other hand, has only a small effect on the contamination. The taggability times efficiency of light flavor jets is only slightly larger than that of b-jets. The definition of the light flavor jet sample is slightly different in this taggability determination from the rest of the analysis. Nonetheless, the set of jets used to determine the taggability is sufficiently similar to the light jet sample’s jets used in the rest of the analysis. The taggability determined here can thus be applied to the light jet sample.

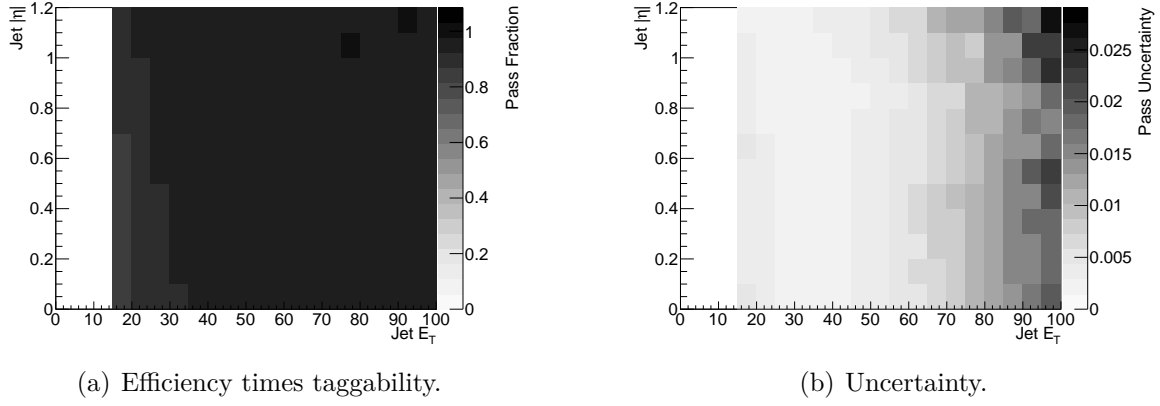


Figure 4.20: Anti-tag efficiency times taggability and its uncertainty, as a function of jet $|\eta|$ and E_T , as determined with the tag and probe algorithm.

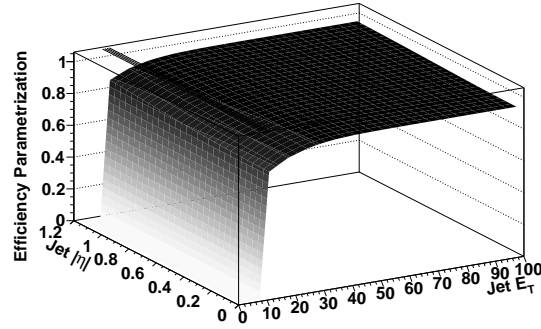


Figure 4.21: Parametrization of the taggability times anti-tag efficiency, as a function of jet E_T and jet η .

Fig. 4.20(a) shows the taggability times JLIP anti-tag efficiency for light jets, Fig. 4.20(b) shows the geometrical mean of the corresponding binomial uncertainties. This distribution is parametrized using the same procedure as for the muon probability from Section 4.3.1, resulting in the distribution shown in Fig. 4.21 with the uncertainty (1σ confidence range) shown in Fig. 4.22. The parametrization of the convolution of the anti-tag efficiency as determined by the DØ b-ID group [29], shown in Fig. 4.19, and the taggability uses the function

$$\varepsilon_{\text{tag}}(E_T, \eta) = (p_0 + p_1 \eta^2) \left(1 + \text{erf} \left(\frac{E_T - p_2}{p_3} \right) \right) \quad (4.4)$$

with parameters p_i . Its pull distribution is shown in Fig. 4.23 (parametrized in jet E_T and η) and Fig. 4.24 (counts of pull values).

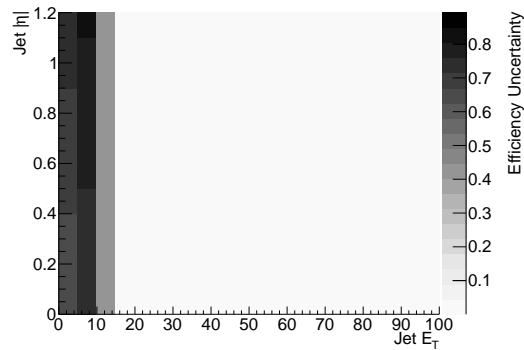


Figure 4.22: Uncertainty on the taggability times anti-tag efficiency parametrization, as a function of jet E_T and jet η .

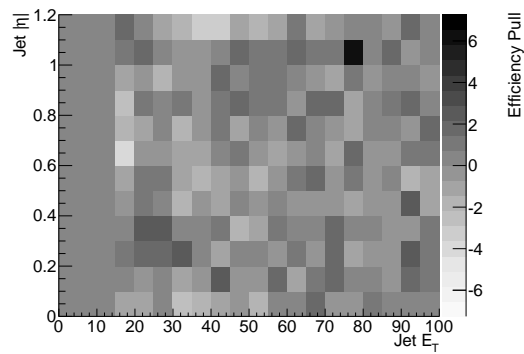


Figure 4.23: Pull distribution as a function of jet E_T and jet η of the taggability times anti-tag efficiency parametrization.

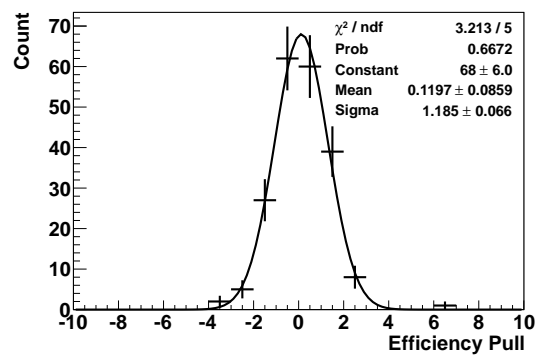


Figure 4.24: Distribution of pull values of the taggability times anti-tag efficiency parametrization.

4.4 Event Selection

Selections are applied to increase the relative abundance of $Z \rightarrow b\bar{b}$ events in the sample in order to make a Z peak more pronounced in the invariant mass spectrum. Selecting $Z \rightarrow b\bar{b}$ events means suppression of light jets and of jets from inclusive QCD b production.

As a first step, only di-jet events are used. Both jets must have a transverse energy $E_T > 15 \text{ GeV}$; only these jets have been studied in $D\bar{O}$. At least one of the jets must have a muon associated with it. Two samples are drawn from the remaining events: a sample with an enhanced b -jet fraction (“ b -jet sample”), and a sample with a reduced b -jet fraction (“light jet sample”). The b -jet sample requires both jets to have a muon associated with them (see Section 4.3.3), not only one, and both jets to be within $|\eta| < 1.2$. The light jet sample requires two JLIP anti-tags, even when at least one jet must have an associated muon. More details of the selections are discussed in the following paragraphs.

4.4.1 b -Jet Selection

The signal sample’s contribution of light jets has to be reduced because the inclusive light jet production cross section $p\bar{p} \rightarrow q\bar{q}$ is orders of magnitude larger than the b -jet production cross section. As the events of the signal sample are triggered by a muon trigger, most of them contain a reconstructed muon. The fraction of b -hadrons decaying (cascade decays included) into a muon with $p_T > 5 \text{ GeV}$ that is close to a jet is much higher than the fraction of c -hadron decays producing such a muon, or of light jets containing a *decay in flight* of e.g. π - or K -mesons producing such a muon. Thus, already requiring a jet to be associated with a muon decreases the light jet contribution, while rejecting only relatively few events containing b -jets. This leads to a considerable net b -enrichment of the sample, see Section 4.3.3.

An associated muon is required for a jet to be called *muon tagged*, see Section 4.3.3. Due to the required jet separation $\Delta\phi > \pi - 0.15$ (see Section 5.3.1), it is geometrically impossible for the two jets to share the same muon for the muon tag: $\Delta R > \sqrt{(\pi - 0.15)^2 + 0} > 0.5$ between jets. To reduce the amount of $b\bar{b} + \text{jet}$ events where the quark and antiquark end up in the same jet, both jets are required to have an associated muon for the b -jet sample.

4.4.2 Measurement of b-Jet Purity Using p_T^{rel}

Muons can be used to determine the b-content of the b-jet sample: muons from b decays and muons from decays of light flavored hadrons have a different transverse momentum distribution with respect to the respective hadrons' momenta. The b-hadron momentum direction is unknown, it has to be approximated by the direction of the jet. Here, as in all other cases of muon-tagged jets in this analysis, the jet's momentum \vec{p}^{jet} is meant to include the muon momentum \vec{p}^μ .

With that, the transverse momentum is given by:

$$p_T^{\text{rel}} = \frac{|\vec{p}^\mu \times \vec{p}^{\text{jet}}|}{|\vec{p}^{\text{jet}}|} \quad (4.5)$$

Especially for light flavor hadrons, the approximation of the hadron direction by the jet direction leads to substantial changes for the distribution.

It is studied as a function of transverse muon momentum $|\vec{p}_T^\mu|$, which is related to the muon momentum $|\vec{p}^{\text{muon}}|$, and jet transverse energy E_T , which in turn is related to the jet momentum $|\vec{p}^{\text{jet}}|$. For muons as decay products of a b-hadron, the p_T^{rel} value tends to be larger than average. This is caused by the relatively large mass difference of the b-hadron and its decay products. The p_T^{rel} distributions for light jets and c-jets differ only slightly. Their separation is not used in this analysis.

The remaining light flavor jet contribution after the soft muon b-tags is determined using these p_T^{rel} distributions. Monte Carlo simulation is used to generate predictions in bins of these parameters called *templates*; merged b-jets with the second jet being a recoil jet are included in the b-jet p_T^{rel} template. Given a muon-jet pair, these templates give a prediction of the p_T^{rel} distribution for light (Q), c- (C) and b-jets (B). The measured distribution D contains an unknown fraction of light (f_q), c- (f_c) and b-jets (f_b); it corresponds to the the sum of these predicted contributions, weighted by their relative fraction:

$$D = f_q Q + f_c C + f_b B \quad \sum_{i=q,c,b} f_i = 1 \quad (4.6)$$

The values of f_q , f_c , and f_b are thus a prediction of the sample's relative composition. The prediction of the f_b component (and thus indirectly also the Monte Carlo predictions

entering here) has been validated with data, using a method called SystemD [4]. The statistical uncertainties of the Monte Carlo templates are considered as part of the uncertainty of the purity. Due to the background subtraction procedure used in the signal extraction (see Section 5), neither the value of the purity nor its uncertainty (statistical or systematic) have an effect on the analysis result.

The templates as well as the measured distribution have a statistical uncertainty due to the limited statistics of the Monte Carlo samples. The minimization procedure to find the optimal values for f_i takes these uncertainties into account by allowing them to fluctuate according to their statistical uncertainty [25]; the fitted distributions can thus differ from the predicted templates. Fig. 4.25 shows the result of the template fits, using the standard $D\bar{O}$ p_T^{rel} template binning in muon- p_T and jet- E_T . Because the statistical uncertainty of the templates is much lower than that of the data distribution, the templates remain almost unchanged during the minimization. Some of the $(p_T^{\text{muon}}, E_T^{\text{jet}})$ templates regions do not have enough data to perform a fit. Given the little data in these regions they will also only have a small influence on the b-purity.

Other regions show no light or charm content in the minimization result. This is an artefact of the very similar light and charm templates, with the minimization procedure failing to distinguish them. As a consequence, the b-jet contribution to the minimization result is relatively stable under fluctuations between the light and charm contributions: the minimization procedure nonetheless provides a meaningful prediction of the b-jet content.

The fraction of b-jets in the b-jet enhanced sample as shown in Fig. 4.26 (a projection of the template fit results on the E_T^{jet} axis) exhibits a dependence on jet E_T and thus, given the sample's event topology, on the di-jet invariant mass m_{jj} . We determine the fraction of b-jets in the b-jet enhanced sample to be $r_b \approx 45\%$; by far most jets are in the lower jet m_{jj} region.

The actual value of the purity is not used in this analysis, it is only used here to cross check the sample's signal yield: the b-jet enhanced sample will be split into two parts, one with enhanced Z content and one with reduced Z content (see the following sections). Subtracting the two will remove both the inclusive b-jet background as well as remaining light jet contamination. A m_{jj} dependence of the b-jet purity will also cancel out and cannot influence the measurement of the $Z \rightarrow b\bar{b}$ signal height and mass.

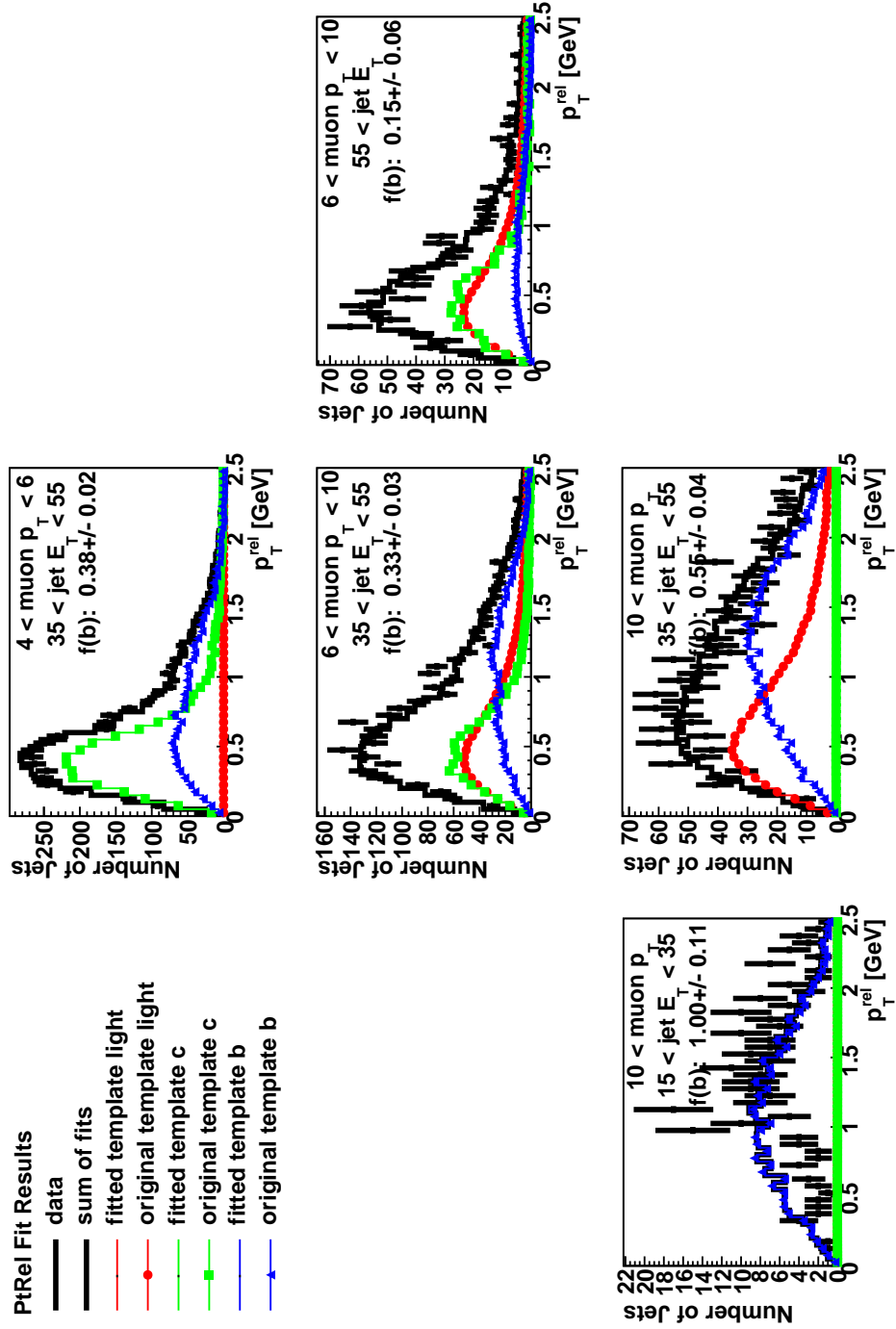


Figure 4.25: Data distribution and p_T^{rel} templates, before and after fitting, for different p_T^{muon} and E_T^{jet} bins. Missing histograms signal a failed fit due to a lack of data in these regions.

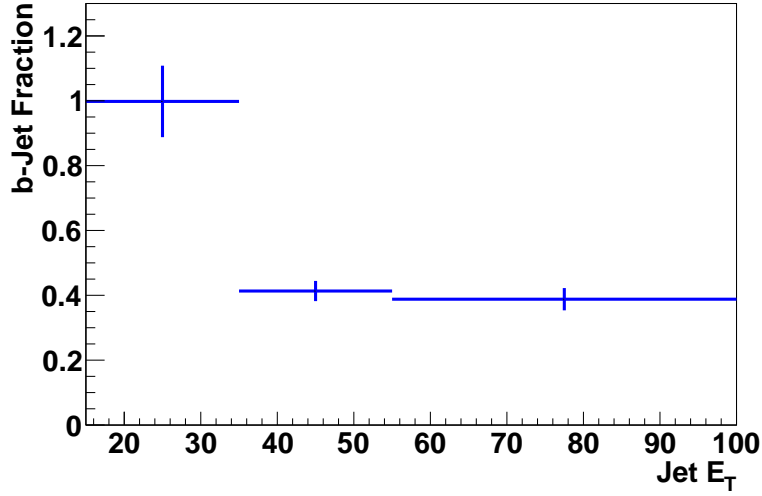


Figure 4.26: The fraction of b-jets in the selected data sample as a function of jet E_T as determined by p_T^{rel} template fits.

4.4.3 Suppression of Inclusive b Production

Those b-jets produced from a Z decay can be mostly found in the central rapidity region around $\eta = 0$, whereas direct production of di-b-jets distributes the jets over a wide range of rapidity. Due to color connection in direct $b\bar{b}$ production, these events are not completely balanced in ϕ ; instead, the jets experience a “pull” towards one another [57, 5]. Hence, b-jets from direct production can be suppressed by requiring a minimal $\Delta\phi$ separation of the two jets, and a minimal $|\eta|$. The exact cut values will be determined when optimizing the signal significance in the next chapter.

The inclusive $b\bar{b}$ contribution could be further reduced by requiring a higher minimal jet E_T . Alas, this also reduces the amount of events with low invariant mass, producing an additional turn-on effect which makes it harder to identify an excess in the invariant mass spectrum around the mass of the Z, about 91 GeV.

4.5 Invariant Mass Spectra

The simplest way to extract the Z signal from the measured invariant mass spectrum would be by comparing measured (Z events and inclusive b-jets) with simulated data of inclusive b-jets only. There are several issues with this approach. The reliability of simulated events with respect to their invariant mass spectra (especially when including a

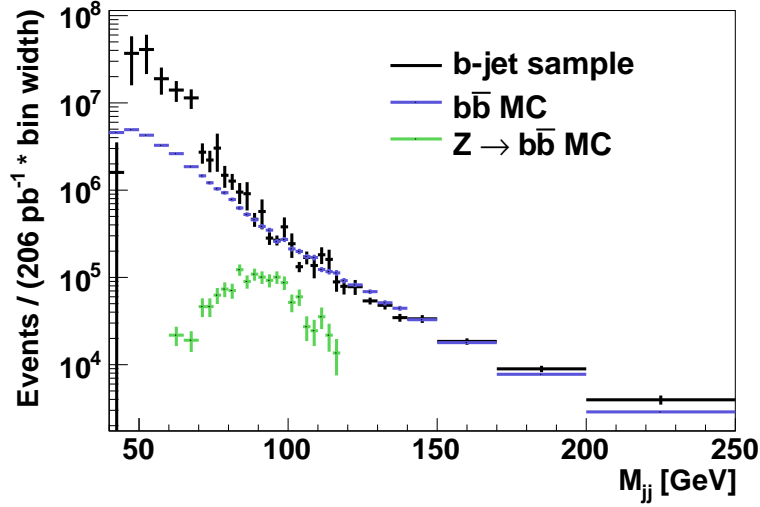


Figure 4.27: Di-jet event invariant mass distribution of the b-enhanced data sample and the Monte Carlo prediction for inclusive b-jets and for the $Z \rightarrow b\bar{b}$ signal.

$\Delta\phi$ -cut, which is sensitive to the relative contributions of different production processes) is not known. The small impact of the Z resonance on top of the invariant mass continuum requires simulation with an exquisite precision. But above all, the unknown contamination of light jet events in the b-jet sample makes it implausible to extract a signal by comparing data with Monte Carlo invariant mass spectra. This is especially true as the contamination varies with invariant mass.

4.5.1 QCD Prediction

The measured and QCD predicted invariant masses of events selected in the light jet sample can be seen in Fig. 4.27 for b-tagged events. Differences between the two spectra are expected to stem from the lack of purity of the b-enhanced sample and the different turn-ons for data and simulated reconstruction efficiencies.

Hence, Monte Carlo simulation cannot be relied on for extracting a $Z \rightarrow b\bar{b}$ signal from the inclusive di-b-jet invariant spectrum.

4.5.2 Impact of the Z Resonance

The QCD cross section for $p\bar{p} \rightarrow b\bar{b}$ is much higher than the $p\bar{p} \rightarrow Z + X \rightarrow b\bar{b}$ cross section. Even when ignoring the bulk of the events at low invariant masses, the effect of

the $Z \rightarrow b\bar{b}$ events is hard to discern from the continuum of QCD generated $b\bar{b}$ events. Fig. 4.27 shows the expected signal and the measured $M_{b\bar{b}}$ distribution.

The Z mass resolution and the low relative cross section do not allow easily for a $Z \rightarrow b\bar{b}$ peak to be observed in the continuum background. Hence, a signal cannot be extracted directly from the inclusive $b\bar{b}$ invariant mass spectrum.

In the next chapter a method will be devised to subtract the continuum $b\bar{b}$ production from the invariant mass spectrum to arrive at a pure signal spectrum.

Chapter 5

$Z \rightarrow b\bar{b}$ Cross Section Measurement

The $p\bar{p} \rightarrow Z$ production cross section times the $Z \rightarrow b\bar{b}$ branching ratio, $\sigma(p\bar{p} \rightarrow Z) \times \text{BR}(Z \rightarrow b\bar{b})$, is determined by counting the number of events in the Z resonance on top of the continuum $b\bar{b}$ invariant mass spectrum. Correcting for the efficiency of the $Z \rightarrow b\bar{b}$ events to be part of this signal sample and accounting for the luminosity corresponding to the sample size, this event count is converted into an estimate of the cross section times branching ratio.

5.1 Outline

The isolation of a $p\bar{p} \rightarrow Z$ signal proceeds in multiple steps. In Chapter 4, the selection of events with two b-jets has been discussed, and the light flavor background to the invariant mass spectrum of the two b-jets has been determined. This chapter continues by describing how $Z \rightarrow b\bar{b}$ events are isolated from the (QCD) continuum of di-b-jet production.

In the previous chapter, a sample with a reduced fraction of b-jets (the “light jet sample”) and one with an increased fraction of b-jets (the “b-jet sample”) have been constructed. Both contain di-jet events where both jets satisfy $E_T > 15 \text{ GeV}$ and $|\eta| < 1.2$. The light jet sample requires both jets to be loose JLIP anti-tagged. The b-jet sample requires both jets to be associated with a muon.

As shown in the previous chapter, a $Z \rightarrow b\bar{b}$ signal excess cannot simply be extracted from an invariant mass spectrum of inclusive b-di-jet data sample, because the signal is too small. Comparing the data sample to Monte Carlo is unfeasible, because the signal is

in the turn-on region of the invariant mass spectrum and the simulation of the relevant efficiencies has uncertainties that can (and as a matter of fact will) introduce excesses when comparing the simulated with the data invariant mass spectrum.

Instead, a Z-enhanced and a Z-suppressed sample are built from the b-enhanced sample described in the previous chapter using different jet separation $\Delta\phi$ cuts. Subtracting their invariant mass spectra ($M_{b\bar{b}}^l(m_{jj})$ for the Z-enhanced, $M_{b\bar{b}}^{\prime}(m_{jj})$ for the Z-suppressed) could then show a possible Z signal. But the $\Delta\phi$ cut introduces a bias on the invariant mass distribution, which needs to be corrected for. To do that, identical cuts are applied to the light jet sample, yielding the two samples $M_{q\bar{q}}^l(m_{jj})$, $M_{q\bar{q}}^{\prime}(m_{jj})$. As the effect of the jet separation cut on the invariant mass spectrum is expected to be largely due to phase space effects and thus flavor agnostic, the continua of the light and b-jet samples are expected to show the same bias. Applying the bias found in the light jet sample to $M_{b\bar{b}}^{\prime}(m_{jj})$ yields an expected distribution for the Z-enhanced spectrum $M_{b\bar{b}}^0(m_{jj})$. The difference of the measured signal spectrum $M_{b\bar{b}}^l(m_{jj})$ and its expected spectrum $M_{b\bar{b}}^0(m_{jj})$ should then show a signal that is not biased by jet separation cuts.

5.2 Efficiency and Statistical Uncertainties

The analysis samples contain only a subset of the events that were created from p \bar{p} collisions, even for Z \rightarrow b \bar{b} events. This inefficiency is caused by the trigger, the physics object reconstruction and the event selection. For an event to become part of the analysis's signal sample it must pass all these stages or causes of inefficiency; the probability for that is thus the product of the probabilities of each stage, given the inclusion in the previous stage.

The efficiency for a given stage depends on several properties; e.g. the efficiency might rise with the available jet energy. It can thus be parametrized by a set of relevant parameters. Additional corrections might be necessary to apply efficiencies determined on one sample to another sample. Here, the efficiencies are derived from and applied to the data sample itself, which removes (or in the case of the combined muon probability on the b-sample reduces) the possibility of systematic effects.

For the event selection of jet $E_T > 15$ GeV and of jet $|\eta| < 1.2$, no efficiencies have been parametrized. They are taken into account by applying these cuts also to the

Monte Carlo prediction of the $Z \rightarrow b\bar{b}$ signal. When calculating the cross section times branching ratio, the Monte Carlo efficiency is used for these global event selection cuts.

5.2.1 Efficiency Correlations

Some of these efficiencies could be correlated or conditional, in which case the combination is not a simple product of efficiencies. A muon could carry a fraction of the jet energy. But because the jet trigger efficiency is parametrized by the uncorrected jet E_T , it does not depend on any ingredient of the combined muon probability. The taggability and JLIP (anti-)tagging efficiencies are track-based, and should not affect the jet trigger efficiency and vice versa. The only remaining possible correlation is between the combined muon probability and the JLIP anti-tagging efficiency. A correlation between those has been ruled out in Section 4.3.1. Possible correlations caused by kinematic effects are accounted for by parametrizing the efficiencies in terms of the relevant kinematic variables, jet- E_T and jet- η .

5.2.2 Validity of b-Jet Efficiencies for $Z \rightarrow b\bar{b}$ Events

Efficiencies for inclusive b-jets are assumed to be also valid for b-jets stemming from a $Z \rightarrow b\bar{b}$ decay. A notable exception is that for $Z \rightarrow b\bar{b}$ events there is no color force between the b-jets and the beam remnants along the incoming beam axis. For most continuum background, on the other hand, there is a color force between the b-jets and the remnants along the beam axis. The energy deposited between the jet and the beam axis could thus serve as a discriminant between $Z \rightarrow b\bar{b}$ and inclusive b production. A study has shown that it is not significant enough [52]; a similar approach has been tried in the context of this analysis and showed insufficient discriminatory power to distinguish $Z \rightarrow b\bar{b}$ events.

Color connection between jets or the beam remnants could have an effect on the jet width $\sigma = \sqrt{\sigma_\eta^2 + \sigma_\phi^2}$. Fig. 5.1 shows the Monte Carlo prediction for the jet widths of inclusive b-jets and jets in $Z \rightarrow b\bar{b}$ production. According to this simulation, inclusive b-jets are slightly narrower. The difference is not significant enough to use it as a means of suppressing inclusive b-jets to form a Z-enhanced sample. On the other hand, the difference in jet widths is sufficiently small to apply the same efficiencies to both inclusive b-jets and those in $Z \rightarrow b\bar{b}$ events.

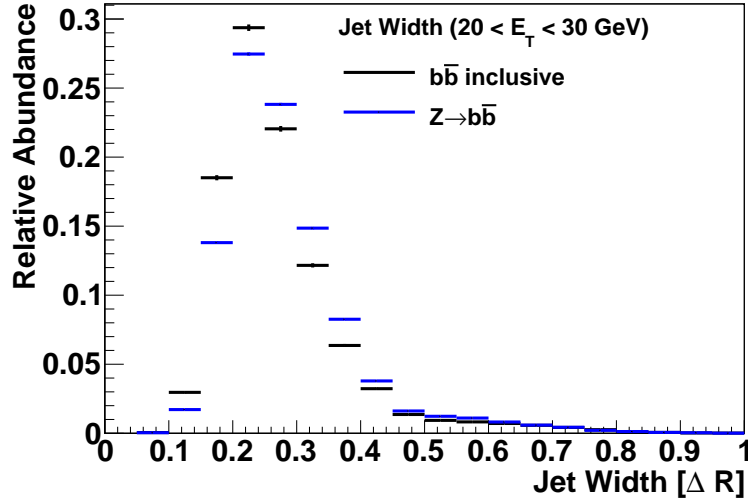


Figure 5.1: Distribution of the reconstructed jet width as predicted by Monte Carlo for b-jets from $Z \rightarrow b\bar{b}$ events and for inclusive b-jets; for $20 \text{ GeV} < E_T < 30 \text{ GeV}$.

Level 1 jet trigger CJT(1,5.)	both samples: 2 jets	jet E_T^{uncorr} , jet η
Associating a jet with a muon including the muon's trigger and reconstruction efficiency	b-jet sample: 2 jets; light jet sample: 1 jet	jet E_T , jet η
Taggability and JLIP anti-tagging	light jet sample: 2 anti-tagged jets	jet E_T , jet η

Table 5.1: Sources of inefficiencies and their parametrization, evaluated independently for the b-jet sample and the light jet sample.

5.2.3 Sources of Inefficiencies

A list of sources of inefficiencies and variables they can depend on can be found in Table 5.1. These efficiencies have been determined from data as shown in the preceding chapter. Note that the JLIP b-tagging efficiency is not used directly by this analysis, it is only used to construct a sample that in turn is used to determine the combined muon probability for the b-jet sample.

Fig. 5.2 and Fig. 5.3 show the distributions of the event selection efficiencies for the light and b-jet sample, respectively. For clarity of visualization, each m_{jj} slice of these distributions is normalized to 1: the small statistics for higher m_{jj} bins would render the distribution of weights invisible in these bins. The normalization allows the distribution of weights *for a given m_{jj} bin* to be seen more clearly.

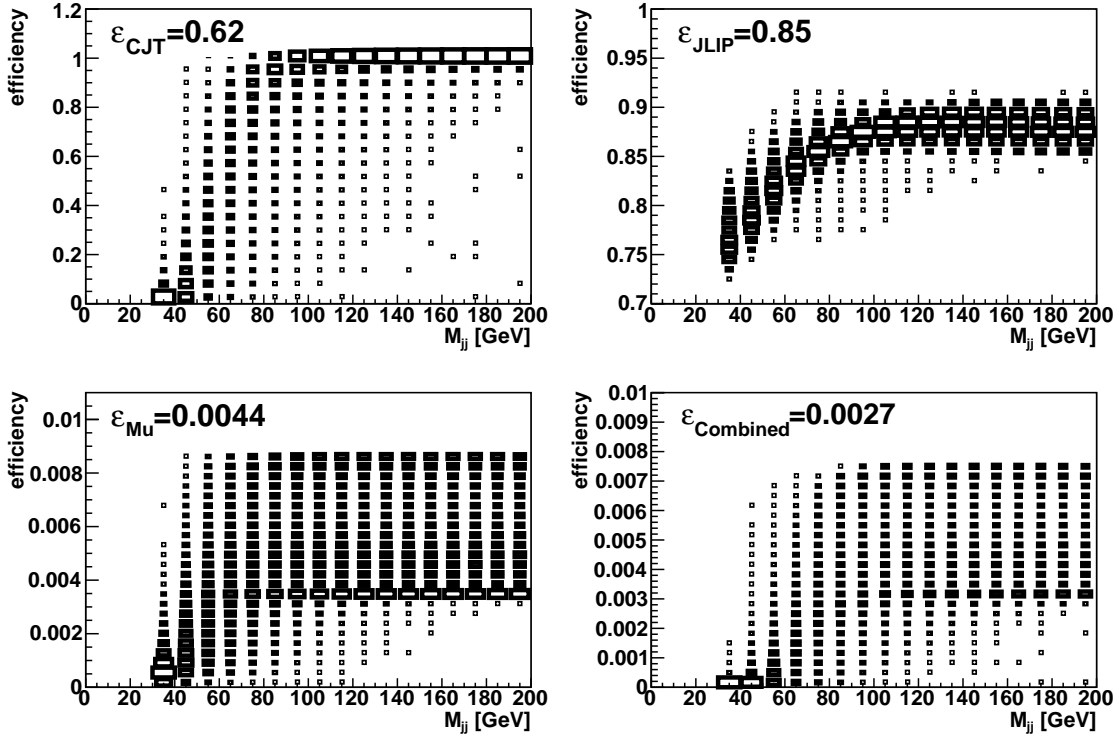


Figure 5.2: The distribution of the event selection efficiency obtained by applying the efficiency parametrization to the light-tagged sample, normalized to 1 for each m_{jj} slice. The integrated efficiencies are displayed in each case as a number.

The muon probability for events of a given m_{jj} is smaller for b-jets than for light jets because b-tagged events require two muons, light-tagged events only one. The structure in the muon probability (and thus in the combined efficiency) for light-tagged events at high m_{jj} stems from the convolution of the plateaus in the distribution of the muon probability (as visible e.g. in Fig. 4.11) and the jets' η and ϕ distributions. The JLIP efficiency distribution for the b-tagged sample is not shown because the JLIP tag is only used for light jet tagging.

5.2.4 Correlations across Invariant Mass Bins, Bin Uncertainty

Traditionally, the uncertainty on an efficiency (parametrized for instance in E_T and η) can have an effect on multiple invariant mass bins, depending on the mapping from E_T and η to the invariant mass bin. To account for this, a full covariance matrix is needed.

This analysis, on the other hand, calculates the efficiencies and their uncertainty for each entry in each of the invariant mass bins. The data sample used for filling the bin is

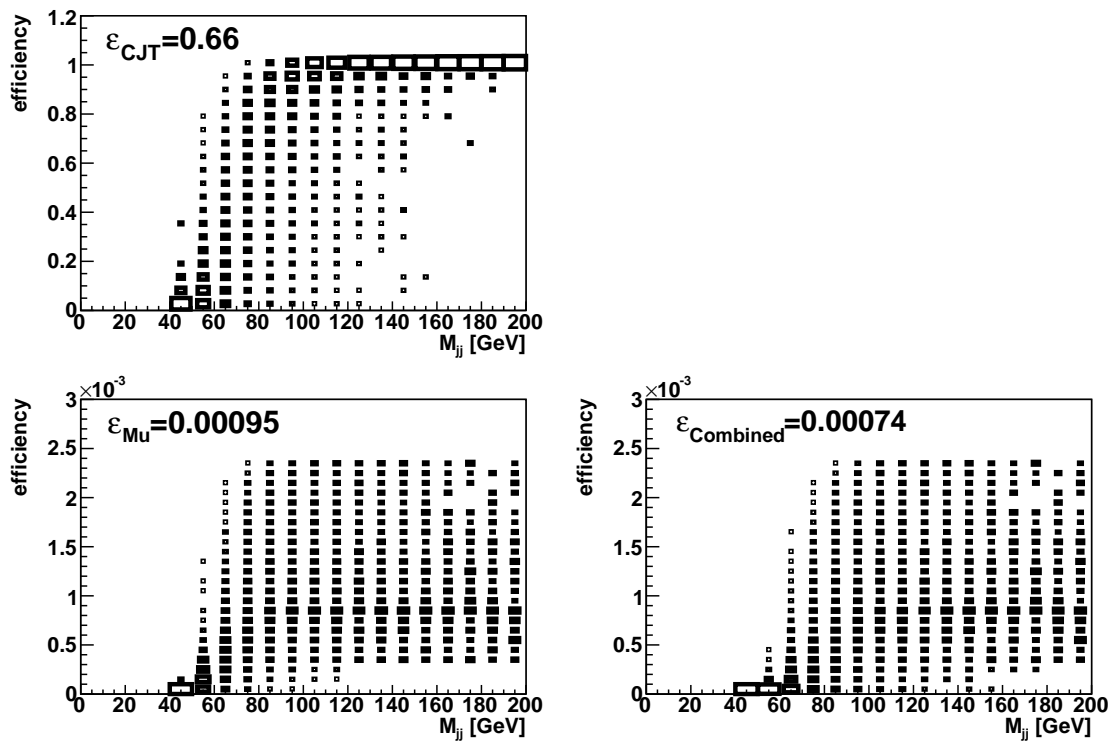


Figure 5.3: The distribution of the event selection efficiency obtained by applying the efficiency parametrization to the b-tagged sample, normalized to 1 for each m_{jj} slice. The integrated efficiencies are displayed in each case as a number.

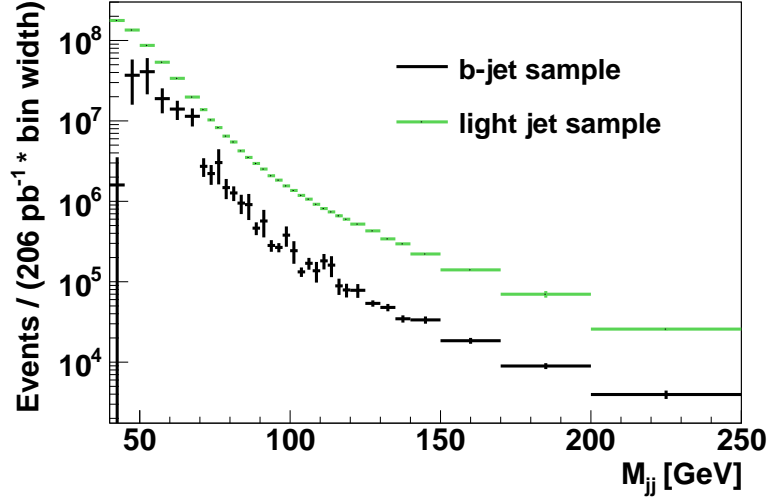


Figure 5.4: The m_{jj} spectra of the b-enhanced sample M_{bb} and -suppressed sample M_{qq} .

determining the mapping into the E_T and η space used to parametrize the efficiency and its uncertainty. As this data sample is sufficiently similar to the signal sample, possible inter-bin correlations of the efficiency uncertainty, when applied to the signal sample, are expected to be well-described by this efficiency determination, even without taking a full covariance matrix into account.

What is left to be determined is thus the uncertainty on an invariant mass bin sampled from weighted events, where an uncertainty is attached to each weight. The uncertainty for a histogram bin is a convolution of the Poisson uncertainty (the “counting” part) and the uncertainty of the weights (the inverse of the product of the efficiencies) that is different for each entry.

Instead of a full convolution, this analysis uses an approximation, treating these two contributions separately¹: $\sigma^2(\text{bin}) = \sigma_{\text{Poisson}}^2(\text{bin}) + \sigma_{\text{weights}}^2(\text{bin})$. A bin with N entries, with the weight of entry i being w_i , has a bin content of $\sum_{i=1}^N w_i$. The Poisson uncertainty is $\sigma_{\text{Poisson}}^2(\text{bin}) = \sum_{i=1}^N w_i^2$. The best estimate of the variance caused by the uncertainty on the weights is the average of the weights’ variances: $\sigma_{\text{weights}}^2(\text{bin}) = \frac{1}{N} \sum_{i=1}^N \sigma_{w_i}^2$.

5.3 Signal Extraction

Figure 5.4 shows the efficiency corrected distributions M_{jj} and $M_{b\bar{b}}$ of the invariant mass m_{jj} for the di-jet events, where the jets have been tagged as originating from a light and b-quark, respectively, as was discussed in the previous chapter, and the jets' azimuthal distance is $\Delta\phi > \pi - 0.8$. The turn-on at low m_{jj} is caused by the jet E_T cut introduced in Section 4.3.2, which is not modeled with event weights but applied equally to data and Monte Carlo.

The reason for dealing with this cut differently than what is discussed in Section 4.1 is the lack of understanding of low energetic jets, as presented in Section 4.3.2: DØ has not studied their behavior enough for them to be included in measurements, neither energy scales nor efficiencies are well determined.

Even after applying the event selection from Section 4.4.3 to increase the Z content, and even with a fitting procedure, a peak or shoulder around 91 GeV is impossible to discern in the $M_{b\bar{b}}$ spectrum. The Z \rightarrow b \bar{b} signal to b \bar{b} continuum background ratio is simply too small, as shown in Fig. 4.27.

In Section 4.4.2, the b-jet purity is estimated to be 45%. Further increasing it would not lead to a clearer signal — the problematic background is the b-jet continuum itself, with its limited statistics.

As the signal cannot be extracted from the signal sample's invariant mass distribution directly, it should ideally be compared to a sample containing the same continuum distribution, but without Z decays. The difference can then be attributed to Z decays.

In practice it will be impossible to obtain a continuum spectrum without any Z decay contamination. But this is not necessary: it is sufficient to be able to compare two spectra containing different numbers of Z decays, as long as the relative contributions of Z decays in each sample are known and sufficiently different.

As shown in Monte Carlo simulations (see Section 2.4.3), the azimuthal separation, i.e. the angle $\Delta\phi$ in the plane orthogonal to the beam, of the two b-jets stemming from a Z is strongly peaked around π ; it is much less collinear for two jets from QCD b production. Therefore, the opening angle between the b- and the \bar{b} -jets is used to construct a Z-enriched and a Z-suppressed sample.

¹Because the efficiencies are sampled from data, their uncertainties are effectively of statistical nature.

5.3.1 Z-Enriched Invariant Mass Spectrum

Additionally to the event selection introduced in Section 4.4, the two jets in an event are thus required to be separated by $\Delta\phi > \pi - 0.15$ to be accepted as contribution to the Z-enriched sample. It will be shown later that $\Delta\phi > \pi - 0.15$ is indeed the optimal cut value.

Monte Carlo studies predict that 72% of all di-jet $Z \rightarrow b\bar{b}$ events for which the jets pass the E_T and $|\eta|$ selections satisfy this requirement. The resulting spectrum, $M_{b\bar{b}}^l(m_{jj})$, is shown in Fig. 5.5.

The same selection is applied to the light jet event sample; the resulting distributions are shown in Fig. 5.6. These light jet distributions will be used to correct for the kinematic effects from the selection of collinear jets.

5.3.2 Z-Suppressed Invariant Mass Spectrum

For an event to be accepted in the Z-suppressed sample, its two jets have to be separated by $\pi - 0.8 < \Delta\phi < \pi - 0.30$. The lower limit of $\pi - 0.8$ reduces the contamination of 3-jet events with a non-reconstructed third jet. These events would invalidate phase space considerations and Monte Carlo studies of distributions of kinematic variables. To be able to compare this sample with the Z-enriched one, the amount of 3-jet events in this sample must be insignificant.

In principle a high lower $\Delta\phi$ limit would be desirable to further reduce the impact of unreconstructed jets. This will at the same time reduce the available $Z \rightarrow b\bar{b}$ events; the value of $\pi - 0.8$ is a reasonable compromise given the two conflicting goals: as can be seen from Fig. 2.7, the value of $\pi - 0.8$ removes almost no signal and keeps most of the $b\bar{b}$ -jet events.

The lower $\Delta\phi$ cut for the Z-enriched as well as the upper $\Delta\phi$ cut for the Z-suppressed sample are subject to an optimization of the signal significance and background description. Section 5.3.6 will explain the optimization procedure. $\Delta\phi < \pi - 0.30$ has been found as the optimal limit for this sample and will be used in the further discussion.

The Z-suppressed invariant mass spectrum $M_{b\bar{b}}^l$, scaled to the same integral as $M_{b\bar{b}}^l$ for easier comparison, is also depicted in Fig. 5.5.

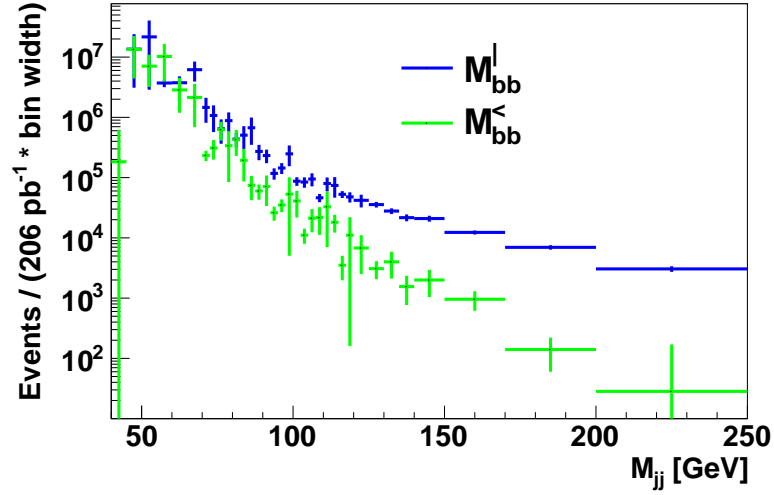


Figure 5.5: The invariant mass spectrum of the b-jet sample, for collinear jets M_{bb}^l and for non-collinear jets $M_{bb}^<$.

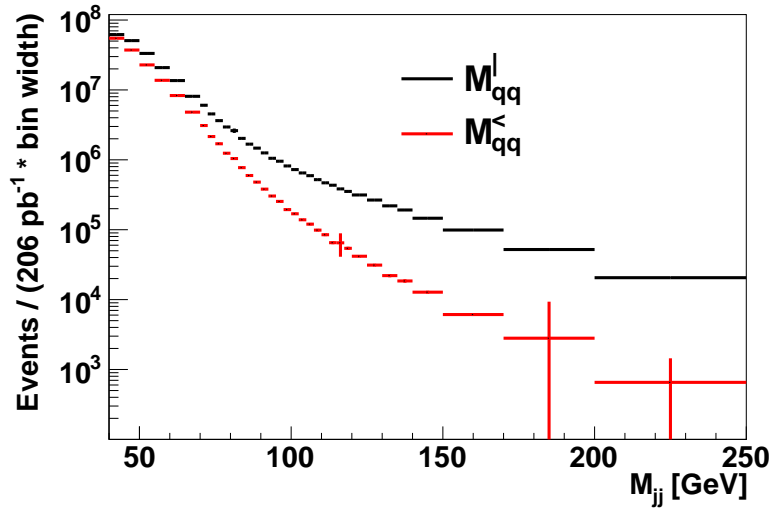


Figure 5.6: The invariant mass spectrum of the light jet sample, for collinear jets M_{qq}^l and for non-collinear jets $M_{qq}^<$.

According to Monte Carlo simulations, this Z-suppressed sample only includes 4% of all Z \rightarrow b \bar{b} events that satisfy the event selection. The Z-content is thus predicted to be a factor 18 lower than in the Z-enhanced sample.

5.3.3 Comparison of Z-Enriched and -Suppressed Samples

Apart from the Z \rightarrow b \bar{b} contribution, the difference between $M_{b\bar{b}}^l$ and $M_{b\bar{b}}^{\prime}$ is purely due to phase space effects caused by the samples' different cuts on $\Delta\phi$. These phase space restrictions result in different invariant mass distributions, even if nature had no Z for us to detect, an effect also observed in Monte Carlo simulations. This phase space effect can be corrected for from the data.

5.3.4 Phase Space Corrections Deduced from Light Jets

Under the assumption that this is purely a phase space effect, the jet flavor is not relevant, so the light jets' invariant mass distributions should show the same effect. The Z \rightarrow q \bar{q} cross section for $q = u + d + s + c$ is negligible compared to the QCD q \bar{q} cross section²:

$$\frac{\sigma(Z) \text{BR}(Z \rightarrow q\bar{q})}{\sigma(q\bar{q})} \ll \frac{\sigma(Z) \text{BR}(Z \rightarrow b\bar{b})}{\sigma(b\bar{b})} \quad (5.1)$$

as $\text{BR}(Z \rightarrow q\bar{q}) \approx 4 \text{BR}(Z \rightarrow b\bar{b})$ [26], and $\sigma(q\bar{q})/\sigma(b\bar{b}) = \mathcal{O}(40)$ [3][54].

The cross section ratio has been estimated from fully reconstructed Pythia6 Monte Carlo samples.

Any noticeable difference of the two light-tagged samples $M_{q\bar{q}}^l$ and $M_{q\bar{q}}^{\prime}$ is thus due to QCD phase space effects and different contributions of production mechanisms, and not due to the Z resonance. The phase space effects are assumed to be the same for light and b-quarks. Monte Carlo has failed to confirm or disprove this assumption: we found (suggested already by [73]) that particle level Monte Carlo simulation with Pythia8 does not model this aspect of the data properly, even after jet finding using the DØ Run II Legacy cone algorithm to cluster stable simulated particles.

²The symbol q will denote the sum of the up, down, strange, and charm quark flavor contributions. In contrast, b denotes the bottom/beauty quark contribution. Top quarks are too scarce to be relevant in this analysis.

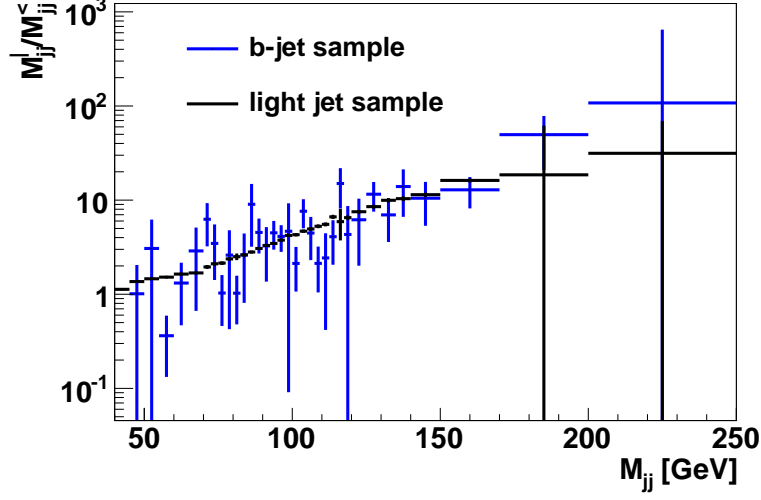


Figure 5.7: The ratios $M_{qq}^{l/\langle}$ and $M_{bb}^{l/\langle}$, determined from the light and b-jet data samples.

The distributions $M_{q\bar{q}}^l$ and $M_{q\bar{q}}^{\langle}$ are shown in Fig. 5.6; their ratio

$$M_{qq}^{l/\langle}(m_{jj}) = \frac{M_{q\bar{q}}^{\langle}(m_{jj})}{M_{q\bar{q}}^l(m_{jj})} \quad (5.2)$$

can thus serve as a prediction for the ratio $M_{bb}^{l/\langle}$ of $M_{b\bar{b}}^l$ and $M_{b\bar{b}}^{\langle}$ if no Z is present:

$$M_{qq}^{l/\langle}(m_{jj}) = M_{bb}^{l/\langle}(m_{jj}) \quad \text{in the absence of Z decays} \quad (5.3)$$

The distributions of $M_{qq}^{l/\langle}(m_{jj})$ and $M_{bb}^{l/\langle}(m_{jj})$ are shown in Fig. 5.7. The two ratios show good agreement with a $\chi^2/\text{NDF} = 17.2/17$ outside the signal region $60 \text{ GeV} < m_{jj} < 120 \text{ GeV}$. This allows the use of the ratio as a prediction of the kinematic behavior of the selection.

In other words, the ratio $M_{qq}^{l/\langle}$ is used to correct $M_{b\bar{b}}^{\langle}$ to the expected $M_{b\bar{b}}^l$ distribution in the absence of a contribution from Z decays, as shown in Fig. 5.8:

$$M_{b\bar{b}}^0(m_{jj}) = M_{qq}^{l/\langle}(m_{jj}) M_{b\bar{b}}^{\langle}(m_{jj}) \quad (5.4)$$

Thus $M_{b\bar{b}}^0(m_{jj})$ and $M_{b\bar{b}}^l$ should be the same if there was no $Z \rightarrow b\bar{b}$ contribution to $M_{b\bar{b}}^l$. It proves to be a good prediction for $M_{b\bar{b}}^l$ for a wide invariant mass range. The difference $M_{b\bar{b}}^l(m_{jj}) - M_{b\bar{b}}^0(m_{jj})$ is shown in Fig. 5.9.

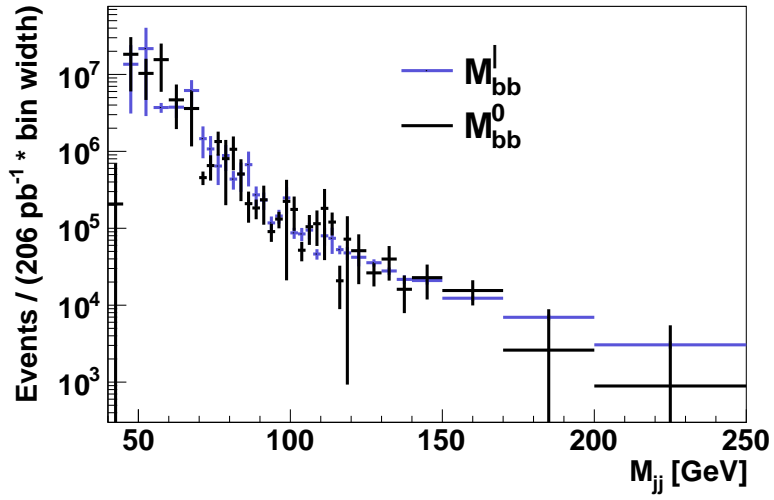


Figure 5.8: $M_{b\bar{b}}^0$ as derived using $M_{qq}^{l/\ell}$ and M_{bb}^{ℓ} , together with M_{bb}^l . The difference of these two corresponds to the signal distribution.

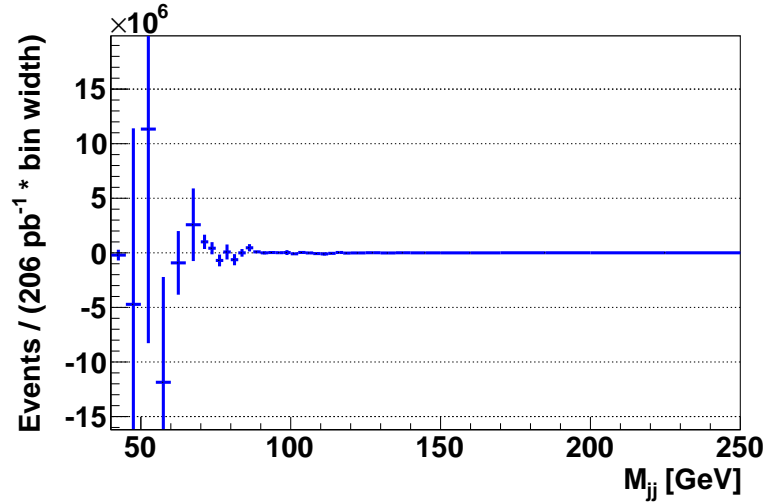


Figure 5.9: The signal $M_{b\bar{b}}^l(m_{jj}) - M_{b\bar{b}}^0(m_{jj})$.

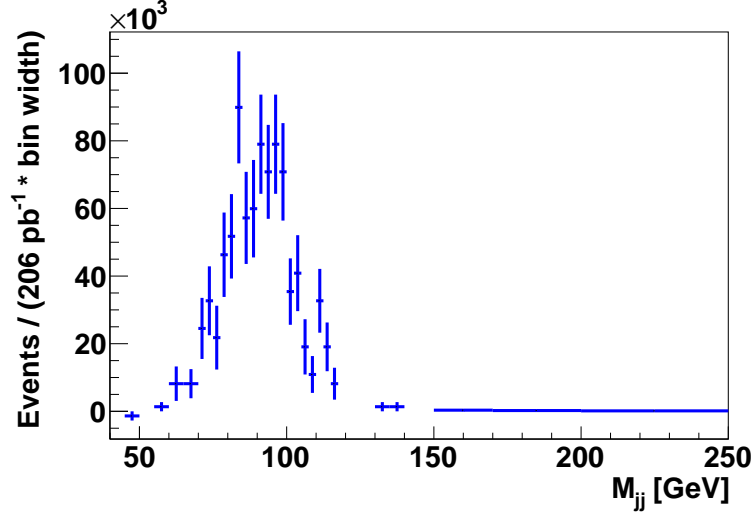


Figure 5.10: Monte Carlo prediction of the $Z \rightarrow b\bar{b}$ signal contribution to $M_{b\bar{b}}^l(m_{jj}) - M_{b\bar{b}}^0(m_{jj})$.

5.3.5 Signal Expectation

The expected signal is determined from a fully reconstructed Pythia Monte Carlo sample of $Z \rightarrow b\bar{b}$ simulated events. Its events undergo the same event selections (only events with two jets, each jet $E_T > 15$ GeV, each jet $|\eta| < 1.2$). The Monte Carlo sample is then split the way the b-jet sample is split, into a sample $M_{Z \rightarrow b\bar{b}}^l$ and $M_{Z \rightarrow b\bar{b}}^c$. The amount of signal events in $M_{b\bar{b}}^l(m_{jj}) - M_{b\bar{b}}^0(m_{jj})$ can then be predicted by $M_{Z \rightarrow b\bar{b}}^l - M_{Z \rightarrow b\bar{b}}^c$, it is shown in Fig. 5.10.

5.3.6 Signal Optimization

The Monte Carlo simulation predicts the majority of $Z \rightarrow b\bar{b}$ events in the invariant mass range of $80 \text{ GeV} < m_{jj} < 100 \text{ GeV}$. This analysis uses the invariant mass range $60 \text{ GeV} < m_{jj} < 120 \text{ GeV}$ for the signal for two reasons.

On one hand, the energy resolution of muon-associated b-jets has not been confirmed on data yet. By widening the signal invariant mass range beyond what Monte Carlo simulation suggests, possible deviations in the jet energy correction are taken into account.

On the other hand, the simulation predicts a significant reduction of the signal contribution outside the range $80 \text{ GeV} < m_{jj} < 100 \text{ GeV}$. By choosing a signal window that is larger than that, the signal search takes this steep gradient into account.

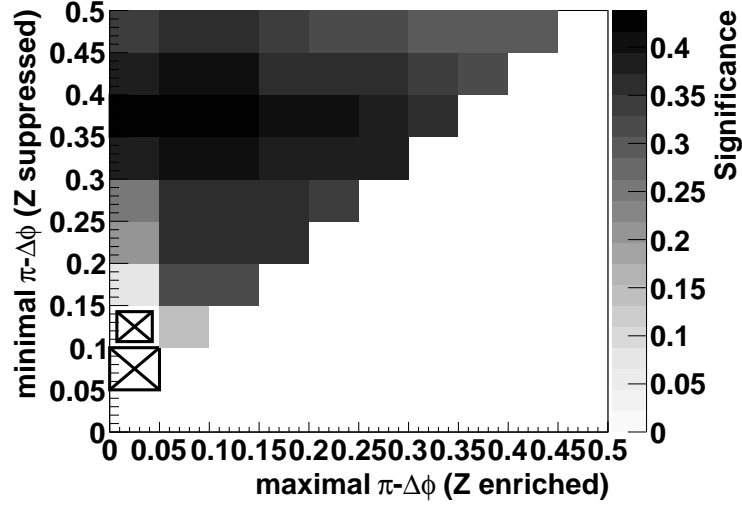


Figure 5.11: Significance (see text) as a function of $\Delta\phi$ limits for Z-enriched (x -axis) and Z-suppressed (y -axis) samples. Bins with impossible limits (diagonal and below) are shown as white; bins with negative significance are crossed out.

The limits for the opening angles of the Z-enriched and Z-suppressed samples still need to be chosen optimally. An optimal choice would not bias the signal region, but minimize the background uncertainty

$$\sigma_{\text{bg}}^2 = \sum_{m_{jj} < 60 \text{ GeV and } m_{jj} > 120 \text{ GeV}} \sigma^2 \left(M_{b\bar{b}}^{\text{I}}(m_{jj}) - M_{b\bar{b}}^0(m_{jj}) \right) \quad (5.5)$$

outside the signal region, i.e. for $m_{jj} < 60 \text{ GeV}$ and $m_{jj} > 120 \text{ GeV}$. On the other hand, the number of signal events $s(m_{jj})$ as predicted by Monte Carlo should be maximized:

$$s = \sum_{60 \text{ GeV} < m_{jj} < 120 \text{ GeV}} \left(s^{\text{I}}(m_{jj}) - s^{\text{I}}(m_{jj}) \right) \quad (5.6)$$

Combining this to allow for an optimal signal detection means that the following function (*significance*) is maximal for the ideal limits for the Z-enriched and Z-suppressed samples:

$$q = s / \sigma_{\text{bg}} \quad (5.7)$$

Fig. 5.11 shows the significance for several values of upper limit for the Z-enriched and lower limit for the Z-suppressed sample. The values used so far, $\Delta\phi > \pi - 0.15$ for

the Z-enriched and $\pi - 0.8 < \Delta\phi < \pi - 0.30$ for the suppressed sample, are thus optimal for signal detection.

The deviation of $M_{b\bar{b}}^l - M_{b\bar{b}}^0$ from 0 outside the Z signal region is used as a measure of the quality of the background prediction. This probes the dependence of the difference between the ratios of $M_{jj}|/\langle$ for light and b-jets (see Fig. 5.7) on the b-jet energy scale.

The regions $m_{b\bar{b}} < 60$ GeV and $m_{b\bar{b}} > 120$ GeV, as already used in Section 5.3.6, of the distribution of $M_{b\bar{b}}^l(m_{jj}) - M_{b\bar{b}}^0(m_{jj})$ will contain virtually no contribution of $Z \rightarrow b\bar{b}$. Only the invariant mass range above $m_{b\bar{b}} > 120$ GeV is used, which is above the Z resonance and at high enough energy to render all relevant quarks effectively massless, excluding possible flavor-dependent effects. The expected result of

$$\chi_{bg}^2 = \sum_{m_{jj}} \frac{\left(M_{b\bar{b}}^l(m_{jj}) - M_{b\bar{b}}^0(m_{jj})\right)^2}{\sigma^2 \left(M_{b\bar{b}}^l(m_{jj}) - M_{b\bar{b}}^0(m_{jj})\right)} \quad (5.8)$$

is NDF, the number of m_{jj} bins in the sum. The signal distribution discussed below and shown in Fig. 5.12 yields $\chi_{bg}^2/\text{NDF} = 13.2/9$ with NDF = 9 the number of bins above the signal region. This corresponds to a χ^2 probability of 33%, which justifies the assumption that the background of $M_{b\bar{b}}^l$ is well described by $M_{b\bar{b}}^0$.

5.3.7 Luminosity Measurement

The luminosity system measured that in the run range 161973 – 196584 a luminosity of $\mathcal{L}_{\text{delivered}} = 556.768 \text{ pb}^{-1}$ was delivered in 424643 LBNs (see Section 3.6 for the definition of LBNs). Out of that, 422708 LBNs are satisfying quality requirements allowing them to be used for the determination of the recorded luminosity. The recorded luminosity as available from the DAQ system, i.e. after the Level 3 trigger and after the exclusion of bad LBNs, leaves $\mathcal{L}_{\text{recorded}}^{L3} = 210 \text{ pb}^{-1}$. Out of that, $\mathcal{L}_{\text{recorded}}^{\text{reco}} = 206 \text{ pb}^{-1}$ was reconstructed. This is the luminosity that enters this analysis. As discussed in Section 3.6, an uncertainty of 6.1% is assigned to DØ's luminosity measurements.

5.3.8 Systematic Uncertainty

The main sources of systematic uncertainties are

1. the jet energy scale,

2. the b-tagging efficiency in the light jet sample, for which a parametrization has been derived in Section 4.3.3,
3. the track trigger tool component of the trigger configuration,
4. the Monte Carlo predictions of the Z event selection efficiencies (efficiency to pass the event selection, and efficiency to pass the criteria of the Z-enriched and Z-suppressed sample).

This analysis, especially by applying Equation 5.3, assumes a common energy scale for $M_{q\bar{q}}$ and $M_{b\bar{b}}$. A systematic uncertainty of 7% is assigned to the jet energy scale [1]. The uncertainty on the b-tagging efficiency has already been incorporated in the JLIP efficiency and taggability uncertainty. The (anti-)JLIP tag is only used on the light jet sample. The sample is split into two; only the ratio of these two samples enters the cross section measurement. As a consequence, possible correlations of uncertainties that span multiple bins are expected to cancel to first order.

Correction from Virtual Photons

As discussed in Section 2.2.5, the exchange of virtual photons contributes to the signal production. The virtual photon is estimated to change the $\gamma^*/Z \rightarrow b\bar{b}$ signal yield in an invariant mass window of ± 30 GeV around the Z resonance by +2% [56].

5.3.9 Signal Fit

The expected, simulated signal from Section 5.3.5 is compatible with the measured spectrum $M_{b\bar{b}}(m_{jj}) - M_{b\bar{b}}^0(m_{jj})$, see Fig. 5.12. Just as for the background region, also here a χ^2 is constructed to evaluate the significance of the distribution's deviation from zero in the signal region:

$$\chi^2 = \sum_{60 < m_{jj} < 120} \frac{\left(M_{b\bar{b}}^l(m_{jj}) - M_{b\bar{b}}^0(m_{jj})\right)^2}{\sigma^2 \left(M_{b\bar{b}}^l(m_{jj}) - M_{b\bar{b}}^0(m_{jj})\right)} \quad (5.9)$$

The number of bins used in this sum is NDF = 22. The data spectrum is compatible with a pure background distribution (i.e. without contributions from $Z \rightarrow b\bar{b}$) with a $\chi^2/\text{NDF} = 22.1/22$ (a 45% fit probability) in the signal region, i.e. for $60 \text{ GeV} < m_{jj} < 120 \text{ GeV}$. This analysis thus fails to find a significant signal. Due to the lack of a signal,

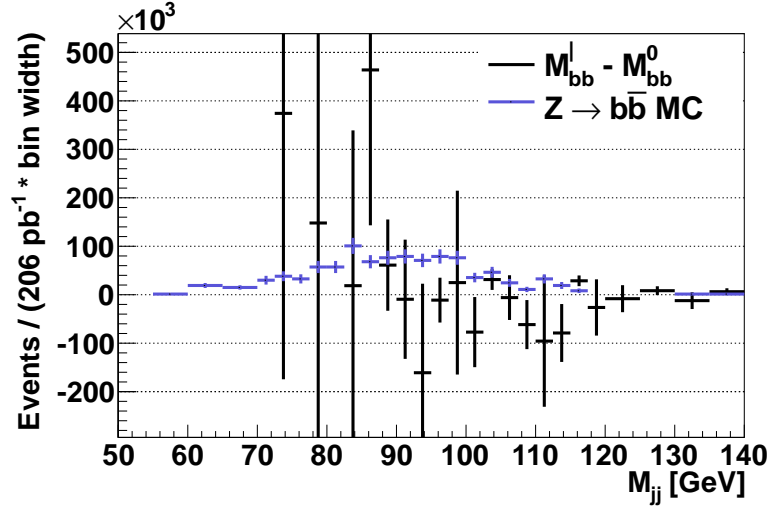


Figure 5.12: Difference between measured and expected invariant mass distribution $M_{b\bar{b}}^l - M_{b\bar{b}}^0$ and $Z \rightarrow b\bar{b}$ signal prediction from Monte Carlo. Note that several data points lie outside the range; see Fig. 5.8.

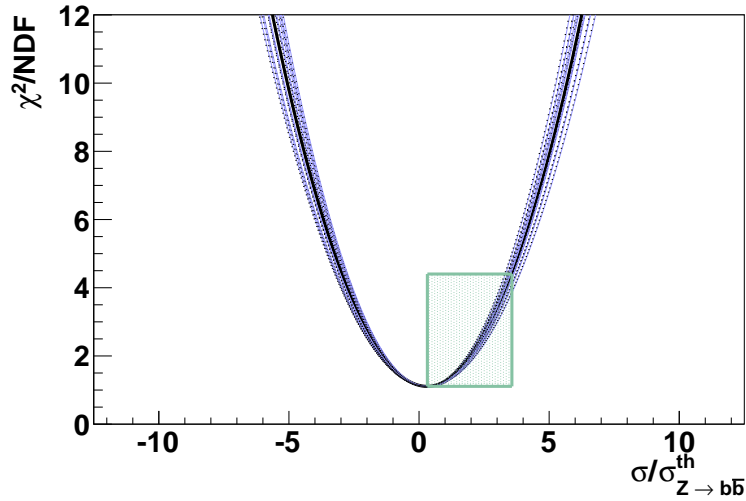


Figure 5.13: χ^2 of the measured signal distribution for scaled signal predictions and their uncertainty caused by the Monte Carlo signal parametrization.

this analysis cannot serve as an indicator of the quality of the b-jet energy scale correction used at DØ.

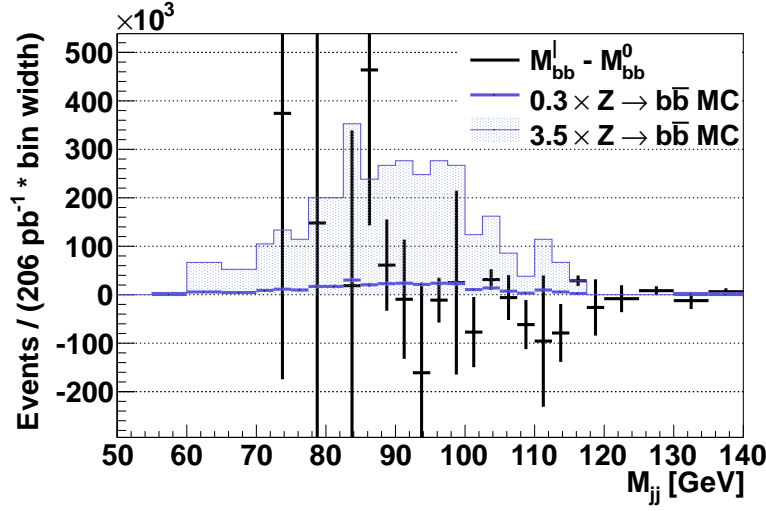


Figure 5.14: Difference between measured and expected invariant mass distribution $M_{b\bar{b}}^l - M_{b\bar{b}}^0$ and $Z \rightarrow b\bar{b}$ signal prediction from Monte Carlo, scaled to the most probable cross section. This shows only a part of the data points in the signal region; see Fig. 5.8.

5.4 Exclusion Limit

An exclusion limit allows to quantify the significance of the lack of a detected signal. It determines how compatible the measured distribution is with a pure background distribution, by subtracting an assumed signal from the measured distribution. Several hypothetical cross section values $\sigma/\sigma_{Z \rightarrow b\bar{b}}^{\text{th}}$ are probed, by scaling the signal distributions predicted from Monte Carlo as shown in Fig. 4.27. The prediction is based on separate parametrizations of the two Monte Carlo signal contributions to $M_{b\bar{b}}^l$ and $M_{b\bar{b}}^c$. Their difference is then used as a prediction of the expected signal contribution, $M_{Z \rightarrow b\bar{b}\text{MC}}$. The χ^2 of a scaled cross section is thus

$$\chi^2(\sigma/\sigma_{Z \rightarrow b\bar{b}}^{\text{th}}) = \sum_{60 < m_{jj} < 120} \frac{\left(M_{b\bar{b}}^l(m_{jj}) - \sigma/\sigma_{Z \rightarrow b\bar{b}}^{\text{th}} M_{Z \rightarrow b\bar{b}\text{MC}}(m_{jj}) - M_{b\bar{b}}^0(m_{jj}) \right)^2}{\sigma^2 \left(M_{b\bar{b}}^l(m_{jj}) - M_{b\bar{b}}^0(m_{jj}) \right)} \quad (5.10)$$

The distribution of the χ^2 values for the different probed cross sections is shown in Fig. 5.13, including the systematic uncertainties stemming from separately varying each parameter of the Monte Carlo signal parametrization by its uncertainty. The most

probable value is at $0.3 \sigma / \sigma_{Z \rightarrow b\bar{b}}^{th}$; the appropriately scaled Monte Carlo prediction is shown in Fig. 5.14 together with the relevant data invariant mass region.

The exclusion limit is determined as the cross section at which the χ^2 value is 1.96^2 times higher than the χ^2 at $\sigma / \sigma_{Z \rightarrow b\bar{b}}^{th} = 0.3$. This allows an exclusion of a process $Z \rightarrow b\bar{b}$ with a cross section $3.5 \sigma / \sigma_{Z \rightarrow b\bar{b}}^{th}$ at 95% Confidence Level.

As explained in Section 4.2.1, the analysis was also carried out using a different CJT trigger parametrization. It results in a different most likely cross section of $0.5 \sigma / \sigma_{Z \rightarrow b\bar{b}}^{th}$. This can be interpreted as a systematic uncertainty on the most likely cross section, which is then $\sigma / \sigma_{Z \rightarrow b\bar{b}}^{th} = 0.3 \pm 0.2$. The original CJT parametrization (that provides a better overall description of the efficiency distribution) yields the more conservative exclusion limit.

Chapter 6

Comparison to other Measurements and Theory

6.1 Other Measurements

The world average of the branching ratio $\text{BR}(Z \rightarrow b\bar{b}) = (15.12 \pm 0.05) \%$ has been determined by [26]. This average uses for instance the measurements by the SLD collaboration [79] of the relative branching ratio $R_b = \text{BR}(Z \rightarrow b\bar{b})/\text{BR}(Z \rightarrow \text{hadrons}) = 0.21594 \pm 0.00094 \text{ (stat.)} \pm 0.00075 \text{ (syst.)}$, using e^+e^- collisions at SLAC, and the LEP experiments' measurements of the branching ratio $\text{BR}(Z \rightarrow \text{hadrons}) = (69.91 \pm 0.06) \%$.

The most precise measurements of the Z decay width to leptons are available from LEP experiments [6, 10, 11, 23], where the Z is produced from e^+e^- collisions. They allow for a combined measurement [26] of the branching ratios $\text{BR}(Z \rightarrow \tau^+\tau^-) = (3.370 \pm 0.008) \%$ and $\text{BR}(Z \rightarrow \mu^+\mu^-) = (3.366 \pm 0.007) \%$.

The cross section times branching ratio for the process $Z \rightarrow b\bar{b}$ at a collision energy of $\sqrt{s} = 1.96 \text{ TeV}$ has been determined by CDF [51] as $\sigma_Z \times \text{BR}(Z \rightarrow b\bar{b}) = 1578_{-410}^{+636} \text{ pb}$.

Measurements for other Z decay channels exist, too. At DØ, the cross section times branching ratio for the Z decaying to $\tau^+\tau^-$ was measured [49] as $\sigma(p\bar{p} \rightarrow Z/\gamma \rightarrow \tau^+\tau^-) = (329.2 \pm 2.3 \text{ (stat.)} \pm 7.8 \text{ (syst.)} \pm 21.4 \text{ (lumi.)}) \text{ pb}$. Given the branching ratios $\text{BR}(Z \rightarrow \tau^+\tau^-)$ and $\text{BR}(Z \rightarrow b\bar{b})$, this predicts a cross section times branching ratio $\sigma(p\bar{p} \rightarrow Z/\gamma \rightarrow b\bar{b}) = (1.48 \pm 0.10) \text{ nb}$. Another measurement from DØ uses the decay to a muon pair [45]; its cross section times branching ratio has been measured as $\sigma(p\bar{p} \rightarrow Z \rightarrow \mu^+\mu^-) = 291.3 \pm 3.0 \text{ (stat.)} \pm 6.9 \text{ (syst.)} \pm 18.9 \text{ (lumi.)} \text{ pb}$. Given the

branching ratio $\text{BR}(Z \rightarrow \mu^+\mu^-)$, this predicts a cross section times branching ratio $\sigma(\text{p}\bar{\text{p}} \rightarrow Z/\gamma \rightarrow \text{b}\bar{\text{b}}) = (1.31 \pm 0.09) \text{ nb}$.

The upper limit derived in this analysis is compatible with above predictions.

6.2 Prediction from Theory

The decay widths of the Z are theoretically well understood; the Standard Model predicts a relative decay width of $R_{\text{b}}^{\text{theory}} = \text{BR}(Z \rightarrow \text{b}\bar{\text{b}})/\text{BR}(Z \rightarrow \text{hadrons}) = 0.2158 \pm 0.0001$ [24] which agrees perfectly with measurements.

6.3 Conclusion

The cross section times branching ratio $\sigma(\text{p}\bar{\text{p}} \rightarrow Z \rightarrow \text{b}\bar{\text{b}})$ has been measured at $\sqrt{s} = 1.96 \text{ TeV}$ using $\mathcal{L}_{\text{recorded}}^{\text{reco}} = (206 \pm 13) \text{ pb}^{-1}$ of reconstructed data from the DØ experiment. The measurement fails to find a significant signal. The most probable cross section and the exclusion limit are found to be consistent with theoretical predictions and previous measurements, for instance at CDF [51]. The lack of significance of this measurement is mainly due to the statistical uncertainty.

More data was taken during DØ's Run IIb, but with a different trigger configuration; the trigger used in this analysis did not exist anymore in Run IIb. This analysis derives event weights from the trigger and event selection efficiencies, and samples most of their parametrizations from data. With trigger and thus event selection changing for Run IIb data, a significant part of this analysis would have had to be redone, which was out of reach for this analysis.

The procedure used in this analysis makes minimal use of Monte Carlo predictions; it has been shown to yield results consistent with expectations, avoiding many biases that can be introduced by other procedures [60]. A sample with larger statistics should allow for additional cross checks, e.g. to quantify the few assumptions in this analysis, especially concerning the similarity of the ratios of the Z-enhanced and -suppressed samples for light and b-jet samples, as presented in Section 5.3.4.

The significance of this analysis rises with the invariant mass. The invariant mass resolution in DØ is sufficient to distinguish peaks at 91 GeV and 125 GeV. Using the

procedure of this analysis also for a Higgs measurement might thus be a viable option, despite the significantly lower production cross section of the Higgs boson.

Bibliography

- [1] V. M. Abazov et al. Measurement of the $t\bar{t}$ production cross section in $p\bar{p}$ collisions at $\sqrt{s} = 1.96$ TeV using kinematic characteristics of lepton + jets events. *Phys. Lett. B*, 626(1-4):45–54, 2005.
- [2] V. M. Abazov et al. The muon system of the Run II DØ detector. *Nucl. Instrum. Meth. A*, 552:372–398, 2005.
- [3] V. M. Abazov et al. Measurement of the Inclusive Jet Cross Section in $p\bar{p}$ Collisions at $\sqrt{s} = 1.96$ TeV. *Phys. Rev. Lett.*, 101, 062001, 2008.
- [4] V. M. Abazov et al. b-Jet identification in the DØ experiment. *Nucl. Instrum. Meth. A*, 620:490–517, 2010.
- [5] V. M. Abazov et al. Measurement of color flow in $t\bar{t}$ events from $p\bar{p}$ collisions at $\sqrt{s} = 1.96$ TeV. *Phys. Rev.*, D83:092002, 2011.
- [6] G. Abbiendi et al. Precise determination of the Z resonance parameters at LEP: ‘Zedometry’. *Eur. Phys. J.*, C19:587–651, 2001.
- [7] G. Abbiendi et al. Charged particle multiplicities in heavy and light quark initiated events above the Z0 peak. *Phys. Lett.*, B550:33–46, 2002.
- [8] A. Abdesselam. Comparison of H-Matrices for electron identification in DØ Run II. DØ Note 3745, 2000.
- [9] M. Abolins, D. Edmunds, S. Gross, and P. Laurens. DØ Run II Level 1 Trigger Framework Technical Design Report. Technical report, 1998.
- [10] P. Abreu et al. Cross-sections and leptonic forward-backward asymmetries from the Z0 running of LEP. *Eur. Phys. J.*, C16:371–405, 2000.
- [11] M. Acciarri et al. Measurements of cross sections and forward-backward asymmetries at the Z resonance and determination of electroweak parameters. *Eur. Phys. J.*, C16:1–40, 2000.
- [12] S. N. Ahmed, S. de Jong, R. Lipton, B. Wijngaarden, S. Duensing, and A. Naumann. DØ SMT Radiation Monitoring System. DØ Note 4022, 2002.
- [13] S. N. Ahmed, R. Lipton, B. Wijngaarden, S. Duensing, A. Naumann, and S. de Jong. DØ SMT Radiation Protection System. DØ Note 3915, 2001.
- [14] G. Alexeev et al. Technical Design Report for the DØ Forward Muon Tracking

Detector Based on Mini-drift Tubes. DØ Note 3366, 1997.

- [15] G. Altarelli, R. Kleiss, and C. Verzegnassi. Z Physics at LEP 1. CERN Yellow Book 89-08, 1989.
- [16] B. Andersson. *The Lund Model*. Cambridge University Press, 1998.
- [17] ATLAS Collaboration. Observation of a new particle in the search for the Standard Model Higgs boson with the ATLAS detector at the LHC. *Phys. Lett. B*, 716:1–29, 2012.
- [18] L. Babukhadia et al. Results of the tevatron higgs sensitivity study. 2003. FERMILAB-PUB-03-320-E.
- [19] P. Balm. Central Track Matching of Muon Tracks at Level 3. DØ Note 3934, 2002.
- [20] P. Balm. Measurement of the B_d^0 lifetime in the decay mode $B_d^0 \rightarrow J/\psi (\mu^+ \mu^-) K_S^0 (\pi^+ \pi^-)$. DØ Note 4319, 2004.
- [21] D. Bandurin, G. Bernardi, C. Gerber, T. Junk, A. Juste, A. Kotwal, J. Lewis, C. Mesropian, H. Schellman, J. Sekaric, D. Toback, R. Van Kooten, C. Vellidis, and L. Zivkovic. Review of physics results from the tevatron. *Intern. J. of Mod. Phys. A*, 30(06), 2015.
- [22] J. L. Bantley, A. Brandt, R. Partridge, J. Perkins, and D. Puseljic. Improvement to the Luminosity Monitor Constant. 1996. FERMILAB-TM-1930.
- [23] R. Barate et al. A measurement of the b-quark mass from hadronic Z decays. *Eur. Phys. J.*, C18:1–13, 2000.
- [24] D. Bardin, M. Grunewald, and G. Passarino. Precision calculation project report. arxiv hep-ph/9902452, 1999.
- [25] R. Barlow and C. Beeston. Fitting using finite Monte Carlo samples. *Comput. Phys. Commun.*, 77:219–228, 1993.
- [26] J. Beringer et al. Review of Particle Physics. *Phys. Rev.*, D86:1+, 2012.
- [27] G. Bernardi, E. Busato, and J.-R. Vlimant. Improvements from the T42 Algorithm on Calorimeter Objects Reconstruction. DØ Note 4335, 2004.
- [28] G. C. Blazey, J. R. Dittmann, S. D. Ellis, V. D. Elvira, K. Frame, et al. Run II jet Physics: Proceedings of the Run II QCD and Weak Boson Physics Workshop, 2000, <http://arxiv.org/abs/hep-ex/0005012>.
- [29] D. Bloch, B. Clément, D. Gelé, S. Greder, and I. Ripp-Baudot. Performance of the Jet Lifetime Probability method for btagging in D0 data. DØ Note 4158, 2003.
- [30] R. Brun and F. Rademakers. ROOT - An Object Oriented Data Analysis Framework. Proceedings AIHENP’96 Workshop, Lausanne, Sep. 1996. *Nucl. Instrum. Meth. A*, A 389:81–86, 1997.

- [31] E. Busato and B. Andrieu. Jet Algorithms in D0 RunII Software: Description and User's Guide. DØ Note 4457, 2004.
- [32] J. Cammin. b Response in p17. Internal presentation for the jet energy scale group, 2008.
- [33] S. Caron. Fast b-identification algorithms for the L2 Silicon Track Trigger. DØ Note 4800, 2005.
- [34] B. C. K. Casey et al. The DØ Run IIb Luminosity Measurement. DØ Note 6317, 2012.
- [35] CDF Collaboration. First Measurements of Inclusive W and Z Cross Sections from Run II of the Tevatron Collider. *Phys. Rev. Lett.*, 94:091803, 2005.
- [36] CDF Collaboration. Search for $wz+zz$ production with missing transverse energy+jets with b enhancement at $\sqrt{s}=1.96$ TeV. *Phys. Rev. D*, 85:012002, 2012.
- [37] CDF Collaboration and DØ Collaboration. Higgs boson studies at the tevatron. *Phys. Rev. D*, 88:052014, 2013.
- [38] C. Clément et al. MuonID Certification for p14. DØ Note 4350, 2004.
- [39] CMS Collaboration. Observation of a new boson at a mass of 125 GeV with the CMS experiment at the LHC. *Phys. Lett. B*, 716:30–61, 2012.
- [40] S. de Jong, C. Galea, and M. Anastasoie. Radiation dose history in the SMT. DØ Note 4653, 2004.
- [41] F. Déliot. The Fit Algorithm in muo_trackreco. <http://www-d0.fnal.gov/~deliot/fitalg.ps>, 2000.
- [42] D. Denisov, G. Gutierrez, A. Ito, V. Turtikov, and D. Wood. Studies of the PDT A-layer efficiency using RAW data. DØ Note 4472, 2004.
- [43] DØ Collaboration. Rapidity gaps between jets in $p\bar{p}$ collisions at $\sqrt{s} = 1.8$ TeV. *Phys. Rev. Lett.*, 72:2332–2336, 1994.
- [44] DØ Collaboration. Measurement of the inclusive differential cross section for Z bosons as a function of transverse momentum in $p\bar{p}$ collisions at $\sqrt{s} = 1.8$ TeV. *Phys. Rev. D*, 61:032004, 2000.
- [45] DØ Collaboration. Measurement of the Cross section for Inclusive Z Production in Di-muon Final States at $\sqrt{s} = 1.96$ TeV. DØ Note 4573, 2004.
- [46] DØ Collaboration. The DØ silicon micro-strip tracker. *Nucl. Instrum. Meth. A*, 560:14–17, 2006. FERMILAB-CONF-06-448-E.
- [47] DØ Collaboration. The upgraded DØ detector. *Nucl. Instrum. Meth. A*, 565:463–537, 2006. FERMILAB-PUB-05-341-E.

- [48] DØ Collaboration. The DØ experiment's integrated luminosity for Tevatron Run IIa. 2007. FERMILAB-TM-2365.
- [49] DØ Collaboration. Measurement of $\sigma(\text{p}\bar{\text{p}} \rightarrow \text{Z} + \text{X}) \text{Br}(\text{Z} \rightarrow \tau^+\tau^-)$ at $\sqrt{s} = 1.96 \text{ TeV}$. *Phys. Lett. B*, 670:292–299, 2009.
- [50] DØ Collaboration. The DØ Silicon Microstrip Tracker. *Nucl. Instrum. Meth. A*, 634:8–46, 2011.
- [51] J. Donini, T. Dorigo, K. Hatakeyama, S. Kwang, C. Neu, M. Shochet, T. Tomura, M. Tosi, and D. Whiteson. Energy Calibration of b-Quark Jets with $\text{Z} \rightarrow \text{b}\bar{\text{b}}$ Decays at the Tevatron Collider. *Nucl. Instrum. Meth. A*, 596:354–367, 2008.
- [52] T. Dorigo. Observation of Z decays to b quark pairs at the Tevatron collider. In *High-energy physics. Proceedings, 29th International Conference, ICHEP'98, Vancouver, Canada, July 23-29, 1998. Vol. 1, 2*, http://lss.fnal.gov/cgi-bin/find_paper.pl?conf-98-197, 1998.
- [53] T. Edwards, S. Yacoob, T. Andeen, J. Park, B. Casey, M. Begel, R. Partridge, H. Schellman, and A. Sznajder. The Updated DØ Luminosity Determination — Short Summary. DØ Note 4328, 2004.
- [54] R. Field. Jet Physics In Run 2 At CDF. CDF/PUB/JET/PUBLIC/7728, 2005.
- [55] Y. Fisyak and J. Womersley. DØGSTAR, DØ GEANT Simulation of the Total Apparatus Response. DØ Note 3191, 1997.
- [56] C. Galea. Measurement of $\sigma(\text{p}\bar{\text{p}} \rightarrow \text{Z}) \text{Br}(\text{Z} \rightarrow \tau^+\tau^-)$ and search for Higgs boson decaying to $\tau^+\tau^-$ at $\sqrt{s} = 1.96 \text{ TeV}$. PhD thesis, Radboud University Nijmegen, The Netherlands, 2008.
- [57] J. Gallicchio and M. D. Schwartz. Seeing in color: Jet superstructure. *Phys. Rev. Lett.*, 105:022001, 2010.
- [58] T. Golling. Measurement of the $t\bar{t}$ Production Cross-Section at $\sqrt{s} = 1.96 \text{ TeV}$ in the Muon+Jets Final State using a Topological Method. DØ Note 4667, 2005.
- [59] M. Goosens et al. GEANT, detector description and simulation tool. GEANT User's Guide, CERN, 2001.
- [60] A. Haas, A. Jenkins, P. Jonsson, and G. Davies. Evidence for $\text{Z} \rightarrow \text{b}\bar{\text{b}}$ Decays at DØ. DØ Note 5204, 2006.
- [61] F. Halzen and A. D. Martin. Quarks and Leptons: An Introductory Course in Modern Particle Physics. Wiley, New York, 1984.
- [62] R. Hamberg, W. L. van Neerven, and T. Matsuura. A complete calculation of the order α_s^2 correction to the Drell-Yan K-factor. *Nucl. Phys. B*, 359:343–405, 1991.
- [63] J. Hegeman. Jet energy scale calibration in the DØ experiment. *Journal of Physics: Conference Series*, 160(1), 2009.

- [64] G. Hinshaw et al. Nine-Year Wilkinson Microwave Anisotropy Probe (WMAP) Observations: Cosmological Parameter Results. *Astrophys. J. Suppl.*, 208:19, 2013.
- [65] F. James. MINUIT. CERN Program Library Long Writeup D506, <http://wwwasdoc.web.cern.ch/wwwasdoc/minuit>, 2000.
- [66] E. Kajfasz. b-production at the Tevatron. <http://arxiv.org/abs/hep-ex/0309033>, 2003.
- [67] F. Koetsveld. On the Angular Correlations of b-jets in $p\bar{p}$ collisions at $\sqrt{s} = 1.96$ TeV. Master’s thesis, Radboud University Nijmegen, The Netherlands, 2006.
- [68] J. Kotcher. Design, Performance, and Upgrade of the D0 Calorimeter. DØ Note 2417, 1995.
- [69] L. Lueking, L. Loebel-Carpenter, W. Merritt, C. Moore, R. Pordes, I. Terekhov, S. Veseli, M. Vranicar, S. White, and V. White. The DØ Experiment Data Grid – SAM. In *GRID*, volume 2242 of *Lecture Notes in Computer Science*, pages 177–184, <http://dblp.uni-trier.de/db/conf/grid/grid2001.html#LuekingLMMPTVVW01>, 2001. Springer.
- [70] A. Maciel, S. Uzunyan, C. Leonidopoulos, and J. Kowalkowski. The L2-Muon Trigger Methods and Algorithms. DØ Note 4756, 2005.
- [71] A. Naumann and F. Filthaut. Combining Prescaled Triggers. DØ Note 4844, 2005.
- [72] T. Nunnemann. NNLO Cross-Sections for Drell-Yan, Z and W Production using Modern Parton Distribution Functions. DØ Note 4476, 2004.
- [73] T. Nunnemann. Vector Bosons in New Phenomena Searches. PhD thesis, Ludwig-Maximilians-Universität München, Germany, 2007.
- [74] OPAL Collaboration. Studies of Charged Particle Multiplicity in b Quark Events. *Z. Phys.*, C61:209–222, 1994.
- [75] V. Papadimitriou. Luminosity determination at the Tevatron. In *LHC Lumi Days Geneva, Switzerland, January 13-14, 2011*, 2011.
- [76] R. J. Pasquinelli. Implementation of stochastic cooling hardware at Fermilab’s Tevatron collider. *J. Inst.*, 6 T08002, 2011.
- [77] T. Sjostrand, S. Mrenna, and P. Skands. Pythia 6.4 physics and manual. *JHEP*, 05:026, 2006.
- [78] T. Sjostrand, S. Mrenna, and P. Skands. A Brief Introduction to PYTHIA 8.1. *Comput. Phys. Commun.*, 178:852–867, 2008.
- [79] SLD Collaboration. Measurement of the branching ratios of the Z into heavy quarks. Technical report, <http://arxiv.org/abs/hep-ex/0503005>, 2005.
- [80] D. Smirnov. Status of the DØ fiber tracker and preshower detectors. *Nucl. Instrum.*

Meth. A, 598(1):94–97, 2009.

- [81] G. Stermann, J. Smith, J. C. Collins, J. Whitmore, R. Brock, J. Huston, J. Pumplin, W.-K. Tung, H. Weerts, C.-P. Yuan, S. Kuhlmann, S. Mishra, J. G. Morfin, F. Olness, J. Owens, J. Qiu, and D. E. Soper. Handbook of perturbative QCD. *Rev. Mod. Phys.*, 67:157–248, 1995.
- [82] UA1 Collaboration. Experimental observation of lepton pairs of invariant mass around 95 GeV/c² at the CERN SPS collider. *Phys. Lett. B*, 126:398–410, 1983.
- [83] J.-R. Vlimant, U. Bassler, G. Bernardi, and S. Trincaz-Duvoid. Technical description of the T42 algorithm for the calorimeter noise suppression. DØ Note 4146, 2003.
- [84] S. Weinberg. A Model of Leptons. *Phys. Rev. Lett.*, 19:1264–1266, 1967.
- [85] D. Whiteson. Global Track Finding at Level 3. DØ Note 3808, 2001.
- [86] B. Wijngaarden. Angular Correlations in Beauty Production at the Tevatron at $\sqrt{s} = 1.96$ TeV. PhD thesis, Radboud University Nijmegen, The Netherlands, 2005.

Summary

The Z boson is one of the particles exchanged in electroweak interactions. Its mass, decay width and branching ratios have been well studied, mostly at lepton-colliders. The Higgs boson is a more recently discovered cornerstone of the Standard Model and is far less well studied.

The Higgs and Z bosons share several similar properties: their masses are of the same magnitude $\mathcal{O}(100)$ GeV; they are both neutral in electric and color charge; they have the same set of possible decay products. However, the branching ratios into these decay products are vastly different for the Z and the H. Particularly interesting decays are into the $b\bar{b}$ pairs with branching ratios $\text{BR}(H \rightarrow b\bar{b}) = 58\%$ and $\text{BR}(Z \rightarrow b\bar{b}) = 15\%$. This predicted dominant decay mode of the Higgs boson into b-quarks has not yet been established beyond any doubt. However, it is one of the more sensitive probes of physics beyond the Standard Model. At hadron colliders, the much more abundantly produced and well studied Z boson can serve to calibrate the search for and measurement of $\text{BR}(H \rightarrow b\bar{b})$.

The DØ detector observed $p\bar{p}$ collisions at the Tevatron collider at Fermilab near Chicago in the USA from 1992 until 2011. From 2001 until 2011, the Tevatron provided collisions at 1.96 TeV center-of-mass energy. One of Tevatron's most promising Higgs search channels is the associated production of a Higgs with a weak vector boson followed by a leptonic decay of the vector boson and the decay of the Higgs into a $b\bar{b}$ pair. Observing the $Z \rightarrow b\bar{b}$ process is thus an important benchmark for Higgs searches. It is also one of the few measurements allowing to verify the b-jet energy scale, which is a prerequisite for accurately measuring the Higgs mass. A novel method to select $Z \rightarrow b\bar{b}$ events at hadron colliders is presented here and tested on a data set of the DØ experiment.

A sample of properly reconstructed DØ events corresponding to an integrated luminosity of $\mathcal{L}_{\text{recorded}}^{\text{reco}} = 206 \text{ pb}^{-1}$ was studied to extract a $Z \rightarrow b\bar{b}$ signal. The b-jets stemming from a Z decay were found to be almost indistinguishable for DØ's detector from b-jets of inclusive QCD background processes. Instead of separating the source of b-jets, a prediction from data for the invariant mass distribution of inclusive b-di-jet events was derived. Given that, the difference between the actual invariant mass distribution and the predicted background invariant mass distribution would be due to the additional b-di-jet events caused by the decay of a Z. A signal should then be visible as a peak around 91.19 GeV, the rest mass of the Z.

Even without Z signal contribution, the invariant mass spectrum exhibits a peak caused by event selection and trigger efficiencies rising with the invariant mass, and the steeply falling invariant mass spectrum. Overlaid with this peak is the relatively small excess caused by Z signal events. The analysis compares the invariant mass spectrum of several samples to extract the excess from signal events.

The shape of the invariant mass spectrum is mostly driven by QCD. Already at invariant masses around 60 GeV, where back-to-back jets have an average energy of 30 GeV, the different quark masses do not play a significant role anymore; their effect on the invariant mass spectrum is negligible. This motivates a possible source for a prediction of the inclusive b invariant mass spectrum: one could assume that the light di-jet invariant mass spectrum is very similar to the b-di-jet spectrum. However, due to differences in the mix of production processes, the angular distribution of di-jets differs for light and b-jets, resulting in shifts in the invariant mass spectrum.

Instead, the analysis splits both the light and the b-jet samples into two sub-samples: jet pairs that are separated in azimuth by more than $\Delta\phi > \pi - 0.15$ are in the Z-enhanced sample (because Z decays will mostly produce jet pairs back-to-back); those jet pairs with $\Delta\phi < \pi - 0.30$ belong to the second, Z-suppressed sample. The ratio of the Z-enhanced to Z-suppressed sample outside of the Z-signal region is found to be identical (within statistical uncertainties) for light and b-jets. The light jet samples' relative content of events stemming from Z decays is much lower than for b-jets, because collisions are much more likely to produce inclusive light jet pairs than inclusive b-jet pairs. The ratios of Z-enhanced and Z-suppressed invariant mass spectra can thus be used to construct a prediction of the b-di-jet invariant mass spectrum without jets from Z decays, even in the Z-signal range.

Inefficiencies in the data taking process and selection were corrected by assigning a weight that is the inverse of the efficiency for such an event to make it into the analysis sample. This approach can be applied to use the data sample itself to predict the phase space distribution of all events, which is needed to calculate the overall signal efficiency.

Due to low statistics of the analysis sample, the enhancement of events around the signal region was found to be consistent with statistical fluctuations of the background. It excludes the process $Z \rightarrow b\bar{b}$ with a cross section larger than 3.5 times the theoretical Standard Model cross section times branching ratio at 95% Confidence Level.

The analysis method can be used for a Higgs search employing only a minimal amount of Monte Carlo simulations — only the fraction of Higgs events decaying to two jets with a given minimal opening angle needs to be simulated. With the large amount of suitably triggered data that has been collected at DØ, it should be possible to find a clear Z signal at DØ with an analysis similar to this one.

The same arguments hold for Z measurements at the LHC experiments. Given enough data with appropriate trigger and reconstruction thresholds, the uncertainties on the weights and the Poisson uncertainties of the background will be reduced. This could make the method used in this analysis a possible candidate for Higgs measurements,

especially if the Higgs mass is not in the turn-on region of the invariant mass spectrum anymore, which increases the weights' precision and reduces the background uncertainty.

Samenvatting

Het Z-boson is een van de deeltjes die uitgewisseld worden in elektrozwakke wisselwerkingen. Zijn massa, vervalsbreedte en vertakkingsverhoudingen zijn goed bestudeerd, voornamelijk in elektron-positron-verstrooiingsexperimenten. Het Higgs-boson is een veel recenter ontdekte steunpilaar van het Standaard Model en is veel minder goed bestudeerd.

De Higgs en Z-bosonen delen verscheidene vergelijkbare eigenschappen: hun massa's zijn van dezelfde grootte $\mathcal{O}(100)$ GeV; ze zijn beide neutraal in elektrische- en kleur-lading; ze hebben dezelfde verzameling mogelijke vervalsproducten. Echter, de vertakkingsverhoudingen voor deze vervalsproducten zijn enorm verschillend. Bijzonder interessante vervallen zijn die naar $b\bar{b}$ -paren, met vertakkingsverhoudingen $\text{BR}(H \rightarrow b\bar{b}) = 58\%$ en $\text{BR}(Z \rightarrow b\bar{b}) = 15\%$. Deze voorspelde dominante vervalswijze van het Higgs-boson naar b-quarks is nog niet boven elke twijfel aangetoond. Echter, het is een van de gevoeligere onderzoeksmogelijkheden voor de natuurkunde voorbij het Standaardmodel. Bij proton-(anti-)proton-verstrooiingsexperimenten kan het veel overvloediger geproduceerde en goed bestudeerde Z-boson dienen om de zoektocht naar en meting van $\text{BR}(H \rightarrow b\bar{b})$ te kalibreren.

De DØ detector heeft van 1992 tot 2011 $p\bar{p}$ -botsingen bestudeerd bij de Tevatron-botser op het Fermilab, in de buurt van Chicago in de VS. Van 2001 tot 2011 leverde het Tevatron botsingen met een zwaartepuntsenergie van 1,96 TeV. Een van de meest veelbelovende Higgs zoek-kanalen bij het Tevatron is de productie van een Higgs in samenhang met een zwak vector-boson, gevolgd door een leptonisch verval van het vector-boson en het verval van de Higgs naar een $b\bar{b}$ paar. Het waarnemen van het $Z \rightarrow b\bar{b}$ proces is aldus een belangrijk referentiepunt voor Higgs-zoektochten. Het is ook een van de weinige metingen die het mogelijk maakt de b-jet energieschaal, die een eerste vereiste is voor het precies meten van de Higgs-massa in dit vervalkanaal, te verifiëren. Hier wordt een nieuwe methode om $Z \rightarrow b\bar{b}$ gebeurtenissen bij hadron-botsers te selecteren gepresenteerd, en de methode wordt getest op een data-verzameling van het DØ experiment.

Een verzameling van goed gereconstrueerde DØ gebeurtenissen, overeenkomend met een geïntegreerde luminositeit van 206 pb^{-1} , is bestudeerd om een $Z \rightarrow b\bar{b}$ signaal te extraheren. De b-jets voortkomend uit een Z verval bleken voor de DØ-detector bijna ononderscheidbaar te zijn van b-jets uit inclusieve QCD achtergrond processen. In plaats van het onderscheiden van de bron van b-jets, is een voorspelling voor de invariante-massaverdeling van inclusieve di-b-jet gebeurtenissen uit de data afgeleid. Met dat gegeven zou het verschil tussen de feitelijke invariante-massaverdeling en de

voorspelde invariante-massaverdeling van de achtergrond toe te schrijven moeten zijn aan de additionele di-b-jet gebeurtenissen veroorzaakt door het verval van een Z. Een signaal zou dan zichtbaar moeten zijn als een piek in de buurt van 91,19 GeV, de rustmassa van de Z.

Zelfs zonder een Z signaalbijdrage vertoont het invariante-massaspectrum een piek, veroorzaakt door het toenemen met de invariante massa van de doelmatigheid van de selectie van gebeurtenissen en de trigger, en door het sterk afnemende invariante-massaspectrum. Het relatief kleine overschot veroorzaakt door Z-signaalgebeurtenissen ligt boven op deze piek. De analyse vergelijkt het invariante-massaspectrum van verscheidene gebeurtenis-verzamelingen om het overschot van signaal gebeurtenissen te extraheren.

De vorm van het invariante-massaspectrum wordt grotendeels bepaald door QCD. Al bij een invariante massa van rond 60 GeV, waar tegenover elkaar liggende jets een gemiddelde energie van 30 GeV hebben, spelen de verschillende quarkmassa's al geen rol van belang meer; hun effect op het invariante-massaspectrum is verwaarloosbaar. Dit motiveert een mogelijke bron voor een voorspelling van het inclusieve b invariante-massaspectrum: men zou aan kunnen nemen dat het lichte di-jet invariante-massaspectrum zeer vergelijkbaar is met het di-b-jet spectrum. Echter, ten gevolge van verschillen in de menging van productie processen, verschillen de hoek-verdelingen van di-jets voor lichte- en b-jets, resulterend in verschuivingen in het invariante-massaspectrum.

In plaats van directe achtergrond voorspelling gebaseerd op lichte quarks splitst de analyse zowel de lichte- als de b-jet verzamelingen in twee sub-verzamelingen: jet-paren die in azimut meer dan $\Delta\phi > \pi - 0,15$ van elkaar af liggen zijn in de Z-verrijkte verzameling (omdat Z vervallen met name tegenover elkaar liggende jets produceren); de jet-paren met $\Delta\phi < \pi - 0,30$ horen bij de tweede Z-onderdrukte verzameling. De verhouding van de Z-vermeerderde en Z-onderdrukte verzamelingen buiten het Z-signaal gebied blijkt identiek te zijn (binnen de statistische onzekerheden) voor lichte- en b-jets. De relatieve bijdrage van gebeurtenissen voortkomend uit Z vervallen aan de lichte-jet verzameling is veel kleiner dan voor b-jets, omdat botsingen veel waarschijnlijker inclusieve lichte-jet-paren dan inclusieve b-jet-paren produceren. De verhouding van de Z-vermeerderde en Z-onderdrukte invariante-massaspectra kan aldus worden gebruikt om een voorspelling te construeren voor het di-b-jet invariante-massaspectrum zonder jets uit Z vervallen, zelfs in het Z-signaal gebied.

Inefficiënties bij het vergaren en selecteren van de data zijn gecorrigeerd door een gewicht toe te kennen dat het omgekeerde is van de efficiëntie voor een dergelijke gebeurtenis om in de analyse gebeurtenis-verzameling terecht te komen. Deze aanpak kan worden toegepast om de data-verzameling zelf te gebruiken om de fase-ruimte verdeling te voorspellen voor alle gebeurtenissen, hetgeen nodig is om de globale signaal-efficiëntie te berekenen.

Ten gevolge van de lage aantallen gemeten gebeurtenissen blijkt de vermeerdering van gebeurtenissen rond het signaal gebied consistent te zijn met statistische fluctuaties van de achtergrond. Het sluit het proces $Z \rightarrow b\bar{b}$ met een werkzame doorsnede groter dan 3,5

keer de theoretische Standaardmodel werkzame doorsnede keer de vertakkingsverhouding uit op een 95% betrouwbaarheidsniveau.

De analysemethode kan worden gebruikt voor een Higgs-zoektocht gebruik makend van een minimale hoeveelheid Monte Carlo simulaties — alleen het aandeel van Higgs-gebeurtenissen die naar twee jets vervallen met een gegeven minimale ruimtehoek moet worden gesimuleerd. Met de grote hoeveelheid data in de volledige door DØ vergaarde dataset, zou het mogelijk moeten zijn een helder Z signaal te vinden bij DØ, met een analyse vergelijkbaar met die hier gepresenteerd.

Dezelfde argumenten gelden voor Z metingen bij de LHC experimenten. Gegeven voldoende data met geschikte trigger- en reconstructiedrempels, zullen de onzekerheden op de gewichten en de statistische onzekerheden op de achtergrond afnemen. Dit zou de methode gebruikt in deze analyse een mogelijke kandidaat voor Higgs-metingen kunnen maken, in het bijzonder als de Higgs massa niet meer in het aanschakel-gebied van het invariante-massaspectrum ligt, hetgeen de nauwkeurigheid van de gewichten doet toenemen en de achtergrond-onzekerheid doet afnemen.

Curriculum Vitae

Nikolaus Axel Naumann was born on May 9, 1974, in Kassel, Germany. Starting 1993 he studied physics and mathematics at the Westfälische Wilhelms-Universität, of Münster, Germany, where he received a physics Diploma in 2000. He started a position with the *Stichting voor Fundamenteel Onderzoek der Materie*, working under the supervision of Prof. Sijbrand de Jong at the Radboud University of Nijmegen, from 2000 to 2004. For about two years during this period he was detached to the US, working at the DØ experiment at the Fermi National Accelerator Laboratory.

From 2004 to 2005, he was working as a Guest Scientist at the Fermi National Accelerator Laboratory, USA. Since 2005 he is employed at the European Organization for Particle Physics, CERN.

Acknowledgments

No thesis can be written without advisors. Yet I have benefited from having Sijbrand de Jong as advisor and Frank Filthaut as co-advisor like virtually no other student. Their perseverance and endurance, as well as their ability to motivate and follow up over years was paramount to the creation of this thesis. Both of you taught me how to apply the knowledge I had collected from books and lectures to an analysis. Dear Sijbrand, dear Frank: thank you for 17 years of guidance, support and help! This thesis would not have happened without you.

The analysis in this thesis is another brick in a series of NIKHEF / DØ analyses; I have benefited notably from the experience and help from Paul Balm, Onne Peters, Bram Wijngaarden, Silke Duensing, and especially Cristina Galea. And thank you all (and Anne-Mieke van den Bergen) for making the time in the US an unforgettable one!

In the US, several people have provided help, input and guidance for this analysis, as well as an improvement of quality of life. Most notably I would like to thank Andy Haas, Daniel Whiteson and Michael Kirby.

Thank you, Michiel Sanders, for providing the Dutch translation of the summary!

I appreciate that DØ allowed me to finish this analysis, and helped me with my questions, for instance on jet identification in the low- E_T regime and b-identification. The DØ Higgs group helped with setting up this analysis.

Even though they have caused an interference with the timely termination of my thesis, I really appreciate the trust of the ROOT project leads and members, allowing me to work on my thesis over the years. I am especially grateful to Rene Brun, Fons Rademakers and Philippe Canal for their support and encouragement. And a special thanks to Bertrand Bellenot for providing me with the magic code for Fig. 3.2.

Finally I would like to thank my family for enduring uncounted weekends of “I have to work on my thesis” instead of enjoying family life. That time is now over. Thank you, Julia!